DESIGN, SIMULATION AND ANALYSIS OF A MOLECULAR NANO-SENSOR OPERATING AT TERAHERTZ FREQUENCIES FOR ENERGETIC MATERIALS

A Thesis

by

SUKESH SHENOY

Submitted to the Office of Graduate Studies of
Texas A&M University
in partial fulfillment of the requirements for the degree of

MASTER OF SCIENCE

May 2007

Major Subject: Mechanical Engineering

DESIGN, SIMULATION AND ANALYSIS OF A MOLECULAR NANO-SENSOR OPERATING AT TERAHERTZ FREQUENCIES FOR ENERGETIC MATERIALS

A Thesis

by

SUKESH SHENOY

Submitted to the Office of Graduate Studies of
Texas A&M University
in partial fulfillment of the requirements for the degree of

MASTER OF SCIENCE

Approved by:

Co-Chairs of Committee,	Jorge Seminario
	Debjyoti Banerjee
Committee Member,	Steve Suh
Head of Department,	Dennis L. O'Neal

May 2007

Major Subject: Mechanical Engineering

ABSTRACT

Design, Simulation and Analysis of a Molecular Nano-Sensor Operating at Terahertz Frequencies for Energetic Materials. (May 2007)

Sukesh Shenoy, B.E., Manipal Institute of Technology

Co-Chairs of Advisory Committee: Dr. Jorge Seminario
Dr. Debjyoti Banerjee

Nano-sensors, as an application of nanotechnology, are extremely important for environmental, medical and security applications. Terahertz science is an exciting new field that is set to impact the field of sensing to a large extent. I proposed to combine the fields of nanotechnology and terahertz science and develop a molecular nano-sensor that operates at terahertz frequencies. I focused our sensing on energetic materials, particularly nitromethane, and conducted an extensive analysis on its frequency spectrum. The study also focused on designing the nano-sensor and determining its terahertz operation characteristics. I subjected it to various conditions through the use of molecular dynamics simulations. Finally we analyzed the simulation results and provided a proof of the concept that we had a working molecular nano-sensor that operates at terahertz frequencies and senses energetic materials.

The results from the frequency analysis of nitromethane showed that the frequency characteristics determined from our simulations were in close agreement with the ones determined experimentally. In addition to this we also successfully demonstrated the use of a Lennard Jones potential to model the CN bond scission of nitromethane. Finally, the

results from the interactions between the nano-sensor and nitromethane showed that the presence of nitromethane causes sufficient change in the terahertz frequency characteristics of the nano-sensor providing a means to detect nitromethane.

DEDICATION

To my parents

ACKNOWLEDGMENTS

I would like to thank my advisor Dr. Seminario for his continuous guidance and support. I would also like to thank my committee members, Dr. Banerjee and Dr. Suh for their encouragement and support.

I am also grateful to the members of my research group, my friends and colleagues who have helped me solve problems pertaining to my research and have made my stay at Texas A&M University a memorable experience.

Finally, I would like to thank my parents and my aunt for their patience, support and encouragement.

TABLE OF CONTENTS

Page

Page

LIST OF FIGURES

FIGURE Page

LIST OF TABLES

1. INTRODUCTION

Nanotechnology and nanoscale materials are a new and are an exciting field of research. The unusual optical, electrical and mechanical properties coupled with inherently small sizes of nanoparticles provide an ability to make applications and devices that were unavailable. One of the applications is that of sensors for chemical and biological species. These sensors can be used for environmental, medical and security applications.

1.1 Sensor features

For any sensor to be effective it has to incorporate certain design and operational features [1].

i) Rapid Response - Sensor should provide the results as quickly as possible.

ii) Reagentless - The sensor does not require additional reagents to process the sensor information.

iii) Regenerable - The sensor can be repeatedly used and the idle time between the sensing activities is less.

iv) Sensitivity - The sensor should be sensitive enough to detect small quantities of the analyte.

v) Selectivity - Various types of analytes should be detectable.

vi) Low Power Consumption - This would be a vital consideration for point of contact and field sensors where power availability is limited.

This thesis follows the style of the *IEEE Transactions on Nanotechnology Journal*.

vii) Sensing environment safety - Nanomaterials have certain properties that may cause them to harmfully interact with the sensing environment which can be biological systems. Nanosensors should be engineered so that they do not have any harmful effect on the sensing environment.

1.2 Issues

There are certain health and safety related issues [2] considering nanosensors. These nanosensors have properties similar to the biological systems that form the working platform for the nanosensor. Thus nanosensors might harmfully interact with the systems at a cellular, sub-cellular and protein levels.

There are legal issues [3] involved with nanosensors that are used in chemical and biological detection. One of the important requirements of the sensors is that it should be discrete and should only detect and inform the presence of the substance it is searching.

For any sensor to be effective it has to provide the results as fast as possible. In the case of chemical sensors speed hasn't been an issue however this has not been the case for biological sensors. For identifying viral and bacterial species most biosensors use polymerase chain reaction [4] that usually takes a long time to produce results. Polymerase chain reaction is a process in which DNA fragments can be replicated rapidly. This may be effective for detect-to-treat sensors but a faster and an equally accurate approach is required for detect-to-protect sensors.

1.3 Types of sensor agents

Sensor agents for chemical and biological sensors in a broad form encompass the substances (analytes) that a sensor is supposed to sense. It can be divided into biological agents and chemical agents.

Biological agents are much more harmful (1-1000 times) than chemical agents [4]. Table – 1 shows a list of biological agents provided by the Centers for Disease Control . (CDC) [5].

Table 1. Biological agents categorized according to the degree of harm the biological agents can cause among humans. Category A being the most harmful and the category C being the least harmful.

Category A	Category B	Category C
Anthrax Botulism Plague Small Pox Tularemia Viral hemorraghic fevers	Brucellosis Epsilon toxin of Clostridium perfringens Food safety threats (Salmonella, E. coli) Glanders Melioidosis Psittacosis Q fever Ricin toxin Staphylococcal enterotoxin B Typhus fever Viral encephalitis Water safety threats (Vibrio cholerae, Cryptosporidium parvum)	Emerging infectious virus such as Nipah virus and hanta virus

Biosensors are used to sense biological agents and they usually have two tasks – sample the environment and look for the existence of a pathogen and identifying the pathogen.

Chemical agents as categorized by the CDC are shown below [6].

Biotoxins - Abrin, Nicotine

Blister Agents - Mustard gas, Luisite

Blood Agents – Arsine, Cyanide

Caustic (Acids) – Methyl bromide, Ammonia

Choking/Lung/Pulmonary Agents – Hydroflouric Acid

Incapacitating Agents – Fentanyls and other opioids.

Long-Acting Anticoagulants - Super Warfarin

Metals – Arsenic, Thallium

Nerve Agents – Sarin, Soman

Organic Solvents - Benzene

Riot Control Agents – Bromobenylcyanide, choloracetophenone

Toxic Alcohols – Ehylene glycol

Vomiting agents – Adamsite

In addition to the above agents one can consider explosives such as TNT, RDX to be chemical agents.

Chemical sensors that sense chemical agents use optical, mechanical, electrical and electrochemical methods to sample and identify the agents.

1.4 Materials used for sensors

Various materials have been tried for the development of sensors. Of all the materials gold has been a metal that has been researched a lot for its unusual properties at the nano level. Nanoparticle probes consisting of two gold particles with covalently bound oligonucleotides [7] have been used in a scanometric approach to sensing. When they encounter target strands, these probes undergo polymerization forming network structures and this process causes a color change from red to blue thus providing a means for detection. The network structures show sharp melting profiles and thus allow differentiating between a complementary strand and a single base mismatch. This ensures that it has high selectivity. Sensitivity is increased by causing silver reduction promoted by the nanoparticle probes. Gray scale values obtained from a flat bed scanner are plotted against target concentration. The lowest target concentration that can be detected is 50 fm. Another way to detect has been to use to an array consisting of microelectrodes prepared from a silicon wafer with capture strands of oligonucleotides filled in the gaps between the microelectrodes [8]. The array is then exposed to a solution of target oligonucleotide and Au-nanoparticle probe solution. The target oligonucleotide attaches to the capture strand at one end and the Au-nanoparticle on the other. Then a solution of AgNO3 and hydroquinone is used to cause a deposition of silver in the gaps thus resulting is a measurable electric signal. Gold nanoclusters have been used for the development of adsistors [9]. These adsistors consist of Gold nanoclusters coated over a pair of electrodes. When this sensor is exposed to an analyte vapor, the vapor is adsorbed by the gold nanoclusters and as a result the distance

between the gold molecules in the nanoclusters changes and hence the resistance which can be measured. Gold clusters have been used for the development of nanocells [10].

Carbon nanotubes with their electrical and mechanical properties are ideal candidates for the development of nanosensors. Sorption based sensors are garnering a lot of interest because of their low power consumption and reduced size. Single wall carbon nanotubes (SWNT) [11] that act as chemocapacitors have been used to develop sorption based sensors. These capacitors are a combination of transducer elements and a chemosensitive layer. The capacitor is based on the principle that the capacitance of a single walled carbon nanotube changes depending on the molecular absorbates. The SWNT capacitor consists of a network of SWNT with palladium electrodes that can be used to measure the capacitance of the SWNT capacitor. One plate of the capacitor is formed by this network and the other is formed by the substrate. The SWNT can be made to sense a particular analyte by coating it with a thin wall of chemosensitive material. When a bias is applied between the plates then the fringe electric field on the surface of the SWNT plate causes the molecular absorbates (analyte) to polarize causing an increase in capacitance. Carbon nanotube has also been used as a single molecule torsional pendulum [12] that can be used to sense nano-scale forces.

Research is going on to use a transistor based approach to nanosensors. MOSFET that can be considered to be at the heart of electronic industry has been used to develop sensors such as MOSFET embedded microcantilevers [13].

Organic thin film transistors that are being considered to be the next generation transistors with speeds rivaling traditional transistors and yet are cheap offer exciting opportunities for sensor applications.

Other materials that are being considered are Piezoelectric coiled nanosprings made from zinc oxide [14] and silver nanoswitches [15] made from silver sulphide that is very small in size and consumes very less power.

1.5. Methods for sensing

1.5.1 Optical absorbance

Every substance absorbs light and the intensity and spectrum of absorption is determined by the size, shape and composition of the substance. Metal nanoparticles that have large coefficients are ideal candidates to be used for optical absorbance of sensing. Metal Nanoparticles bind to the surface of the analyte and using transmission-mode optical microscopy, electron microscopy or force microscopy one can measure the density of the bound nanoparticles and thus in turn determine the concentration of the analyte.

One of the methods that has been researched consists of using nanoparticle probes consisting of two gold particles with covalently bound oligonucleotides [7]. When they encounter target strands, these probes undergo polymerization forming network structures and this process causes a color change from red to blue thus providing a means for detection.

1.5.2 Optical scattering

Scattering of light is the process in which light changes direction after it penetrates a transparent object. The amount of scattering depends on the properties of the transparent material and is brought about by surface plasmon resonance. Similar to optical absorbance if transparent nanoparticles attach themselves to the analyte, one can determine the concentration of the nanoparticles and hence the analyte using optical scattering [16].

1.5.3 Raman scattering

When light is incident on polarizable molecules the incident photon can excite vibrational modes of the molecules, yielding scattering photons which are diminished in energy by the amount of the vibration transition energies. Scattering of photons once again depends on the properties of the molecule and the spectrum observed is unique to the molecule. One application of Raman scattering is Raman spectroscopy. Raman spectroscopy offers advantages like samples are not destroyed, pretreatment of samples is not necessary and interference of water is weak. However, one has not been able to use them on biological molecules which exhibit fluorescence. Fluorescence is a process in which a molecule absorbs a high energy photon and emits a low energy photon with a longer wavelength while the energy absorbed results in molecular vibrations or heat. To overcome these problems Raman microspectroscopy has been used where fluorescence effect has been reduced. Another way is to use molecular chemical imaging using both Raman and fluorescence optical spectroscopy [17].

1.5.4 Electrical detection

The previous methods of detection were optical methods. We can use electrical methods of detection too. The principle used is that the analyte to be sensed changes the electrical characteristics in a circuit that can be measured.

Transducers can be in the form of chemoresistors [9] that measure a change in current caused by change in resistance caused by analyte interaction, or chemocapacitors [11] that measure a change in dielectric constant.

1.5.5 Electromechanical detection

A combination of electrical and mechanical components can be used for sensing applications. The principle used is that interaction with the analyte causes a mechanical displacement that can be transformed into an electrical signal. Some of the applications that have been developed are i) MOSFET embedded microcantilevers [13] where the deflection of these cantilevers results in a change in the drain current in the MOSFET which can be measured. The cantilevers are deflected due to the binding of biotin molecules to target probes immobilized on the cantilevers. We see that as the more and more biotin molecules bind on the microcantilevers, there is more bending and hence the drain current decreases. The bending is caused due to an increase in compressive stress resulting from repulsive electrostatic or steric intermolecular reactions, or by changes in hydrophobicity of the surface. The system can detect deflections in the range of 5nm-10nm. ii) Single molecule torsional pendulum [12] that consists of a single wall carbon nanotube with a weight attached to it. The carbon nanotube has a low torsion constant

thus it can determine forces applied to it depending on the torque and measuring the resulting deflection. Thus this mechanism can be used to sense nano-scale forces.

iii) Piezoelectric coiled nanosprings [14] which can stretch or compress depending on the electric field applied in lengths of nanometer scale.

1.5.6 Terahertz sensing

Terahertz radiation lies in between the microwave and the infrared region in the electromagnetic spectrum. The wavelength lies in between the 30 micrometer and 1 mm region. Terahertz radiation can penetrate into organic materials and doesn't cause damage like X-rays thus leading to better applications in sensing. One of the preliminary research efforts was to examine the terahertz frequency absorption characteristics of DNA [18].

This led to further research in DNA and other biological molecules and it was established that the Terahertz frequency absorption characteristics were dependent on the species specific resonant characteristics at the molecular level. Thus providing groundwork to develop sensors that would identify different biological agents based on their terahertz absorption characteristics. Teraview has developed a method for detecting cancerous cells using terahertz radiation [19]. Since terahertz radiation can penetrate clothes, another application that has been envisaged is a non intrusive detection of explosives on passengers at the airport.

Various terahertz operating devices are being researched that can be used as sensors. Simulations performed on gold clusters interconnected with 2, 5-dinitro-1, 4-

diethynylphenylthiolate-benzene molecular devices [20] arranged in a square conformation have shown that it is possible to develop a device operating at terahertz frequencies [21]. Based on this elemental device a nanocell [10] has been developed. It is a device that uses molecular electrostatic potentials for storing data and molecular vibrational states for transmitting data. The programmability feature of the nanocell makes it attractive to sensing applications.

1.6 Terahertz sensing

There are two issues to be considered for terahertz sensing. The first is the limited availability of spectral signatures of a biological molecule in its natural state and the second the limited variation in the spectral signatures (absorption frequency variations) [22].

One idea is to perform controlled perturbations of the biological molecule so that we can achieve more phonon mode information. Terahertz signatures are affected by the molecular bonding in the biological molecules and a change in the conformational state of the molecule will result in a change in the terahertz signature. This may result in enhanced information of the terahertz signature for a particular biological molecule. One of the ways that the molecular conformation can be changed is by providing an external stimulus which can be in the form of an optical or terahertz radiation. Experiments on bovine pancreatic ribonuclease [23], a globular protein, has shown that by providing an external stimulus (thermal) the molecular conformation changes which in turn affects the terahertz spectral characteristics of the protein. Therefore the need is to develop an

integrated architecture involving electrical, terahertz and optical interactions also called ETO and provides a novel approach for multistate spectral sensing (MS).

When one measured the dynamical phonon mode information using macroscopic measurement techniques, it was seen that the terahertz signatures were weak and broad resonant features. Also the absorption frequency spectra for different biological molecules measured showed a limited variation, making it difficult to differentiate one biological molecule from another. Until recently it was believed that lower concentration of the biological molecule would result in weaker signatures, however experiments conducted on bacillus subtilis [24] have shown that as the concentration gets lower the signature gets stronger and also sharp resonant features are observed. The terahertz radiation excites the transverse optical phonon in the wall of the bacillus subtilis. This can be depicted as a simple mass spring mechanism. The coupling of the terahertz radiation and the bacillus subtilis take place because of the fact that the wall of the bacillus subtilis shows polar characteristics.

The need to understand and use the effect of terahertz radiation on biological molecules at the molecular level and the desire to obtain strong and sharp terahertz signatures by using minute concentrations of the biological molecule entails that we use a nanoscale approach to terahertz sensing.

1.6.1 Biomolecular architectural concept

As seen from the previous observations we need to develop an architecture using the electrical, optical and terahertz characteristics of biomolecules. The idea is to incorporate

biomolecules in circuits that help to utilize the conformation dependent frequency absorption characteristics of biomolecules. Specific molecules such as DNA and RNA can be used to provide integrated molecular-level sensing and data processing. Almost all DNA and RNA molecules can be elevated to excited states using external stimuli thus forming a basis for an ETO based biomolecular architecture.

Fig. 1 shows the conceptual design of ETO based architecture. The principal element in the architecture is the biomolecule that acts as a tunable filter i.e. the terahertz absorption peak f1 depends on the excitation frequency f2. It consists of two sources – one a terahertz source at frequency f1 and the other source might be a terahertz or optical source at frequency f2. A detector is employed that is used to detect the terahertz radiation at frequency f1. A D.C driver circuit is employed to provide power to the various components of the circuit. The biomolecule helps to provide feedback and clocking/register function. The advantage of this circuit is that the components are operating at different frequencies thus providing operation isolation between different architectural components.

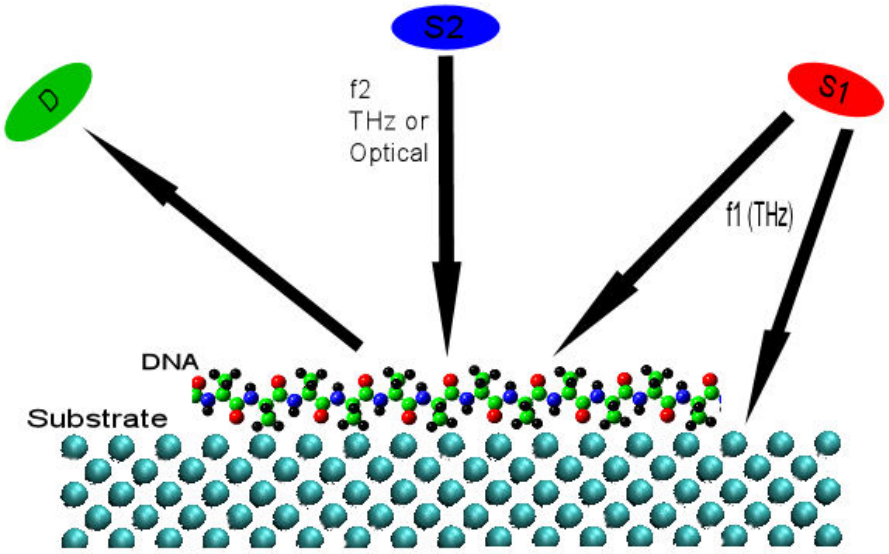

Fig. 1 ETO architecture concept (adapted from Ref [22]). S2 source is used to induce alternative geometric conformations of the DNA. D is a detector that detects the terahertz radiation emitted from S1 source at f1 frequency. Enhancement of signals achieved using Surface Enhanced Raman Scattering. Multiple terahertz signatures of the biomolecule achieved by detemining the terahertz absorption characteristics at alternative geometric conformations.

Since the entire premise of the above concept is based on the fact that the spectral absorption characteristics are dependent on the external stimuli, the architecture can be easily envisaged as a nano-bio sensor. The biomolecule that needs to be sensed can be incorporated into the architecture and its spectral characteristics can be analyzed thus providing us a novel way to sense its presence.

The success of the multistate spectral sensing depends on the identification of molecules that can be excited into various metastable states with different geometrical configurations through controlled external excitation signals.

Experiments conducted on cis-trans isomers of butene and large biomolecules have led to the conclusion that these molecules can undergo photoisomerisation and thus can be incorporated into the ETO architecture concept.

The ETO based architecture can be used to develop a nano-bio sensor. The architecture can be experimentally and computationally validated by using a certain biomolecule that is suitable for multistate spectral sensing. Since the architecture is a concept one needs to identify and analyze the various elements of the circuit.

1.6.2 Terahertz source

Terahertz sources in our ETO architectural concept can be identified as one of the important elements due to its cost, availability and functional requirements. There is a dearth of efficient and reliable terahertz sources and this area is seeing a lot of research to address these issues. This research has led to the identification of various broad band and narrow band terahertz sources. Table-2 shows a comparative study of various prospective terahertz sources that can be used in the ETO architecture. The various terahertz sources are analyzed using different factors such as power output, usable frequency range, cost of the source and the related disadvantages. Since terahertz science is in its infancy stage most of these sources are yet to be commercially developed. Though one can build these sources in the laboratory it is a cumbersome task and is also time consuming. The table also indicates whether turnkey systems are commercially available in the market. The primary factor that governs the selection of the terahertz source for experimental validation is its cost. As of this moment the cost of terahertz

sources are relatively high and there is continuous research going on the develop materials and technology to bring down the cost without effecting the functional and operational characteristics of the terahertz sources. Based on the cost we see from the table that one can build a terahertz source using a combination of frequency multipliers, oscillators and amplifiers. These components are readily available in the market and offer features (frequency and power output) that are critical functional requirements to consider them as terahertz sources in the ETO architecture.

Table 2. Comparative study of various terahertz sources.

	Optically pumped terahertz lasers	Quantum cascade lasers	Time Domain Spectros-copy	Backward wave oscillators	Frequency multipliers oscillators +amps	Photoconductive emitters
Average Power	~100 mW[19]	~50 mW [25]	~500 mW [26]	~ 10 mW [19]	0.1-1 mW [27]	nW to µW [25]
Usable range	0.3-10 THz [19]	2.1-4.8 THz [28]	0.1-2 THz [19]	0.03-1.2 THz [28]	0.1-1THz [27]	0.2-2THz [25]
Contin-uous Wave / pulsed	CW or pulsed [19]	CW (at 97K) or pulsed (at 137K) [25]	Pulsed [19]	Pulsed or CW [29]	CW [27]	CW [19]
Turnkey systems availab-le	Yes [19]	No [30]	Yes [19]	Yes [19]	Yes [27]	Yes (laser source + photoconductive antenna) [30]
Cost (in $)	N/A	N/A	N/A	24000 [30]	N/A but cost less than photomixers [27]	48000 [30]
Major disadv-antages	May have higher cost	Commercia-lly unavailable and operates at low temperatures	Pulsed output	Complex, require high power and are not portable [27]	Tunability is 10 -15% of the center frequency [19]	Cost and operates at low temperature

1.7 Biological molecules

Biological molecules form the living cells. They are made from a combination of monomers to form polymers. One type of the biological molecules that occur in living organisms is organic molecules. The four different organic molecules are as follows.

1.7.1 Proteins

They are made from a set of building blocks called as amino acids. Essential amino acids are those that the body cannot produce and they need to be included in the diet whereas non essential amino acids can be produced by the body.

Proteins are polymers of amino acids. Amino acids exist in 20 different forms naturally and different amino acids combine to give different proteins. The structure of an amino acid is as shown in Fig. 2(a). It consists of a hydrogen atom, an amino group NH_2, a carboxyl group (COOH) and a side chain R which is the differing part of different amino acids.

Two amino acids combine to form a dipeptide and a lot of amino acids combine to form a polypeptide as shown in Fig. 2(b) through condensation. The number of amino acids and the order in which they are linked to form the polypeptide is called the primary structure. The primary structure governs the function of the protein a slight change in the order of the amino acids may cause the protein to function differently or may render it useless. The proteins may then twist to form the secondary structure. The twisting may be in the form of an alpha helix or a beta pleated sheet.

The tertiary structure gives the protein its three dimensional shape. This shape is formed by amino acids which are in close proximity. Hydrogen and disulphide bonds help to form the tertiary structure. Globular proteins may also be formed. Some examples of globular proteins are haemoglobin, enzymes and antibodies.

Quaternary structures are formed when two or more tertiary structures bond together. Proteins are susceptible to external stimuli such as heat and pH thus causing it to change its tertiary structure. This is called denaturization. In the case of globular proteins denaturization causes it to change its shape from a ball to some other shape thus causing a change in its properties.

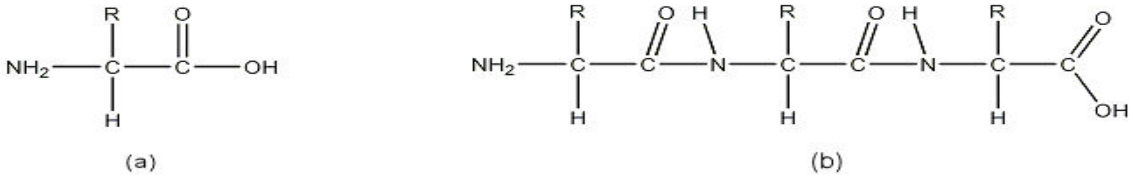

Fig. 2 Proteins. (a) Amino acid consisting of one hydrogen atom, amino group (NH2), carboxyl group (COOH) and R (different for different amino acids) (b) Polypeptide formed from the combination of many amino acids through condensation

1.7.2 Carbohydrates

They are biological molecules that are made of carbon, hydrogen and oxygen. They include sugars, glycogen, cellulose and starches Carbohydrates may be in the form of monosaccharides, disaccharides or polysaccharides.

Monosaccharides consist of single sugar unit such as glucose. They are sweet to taste and are small, polar molecules. The structure of a monosaccharide such as glucose is shown in Fig. 3

There are two different forms of glucose – alpha glucose and beta-glucose. The structure of alpha glucose is as shown Fig. 3 whereas the structure for beta-glucose is obtained by interchanging the position of H and OH of the rightmost carbon atom.

Disaccharides are formed by the reaction of two monosaccharides through condensation. For instance, a maltose molecule and water is formed by a combination of two glucose molecules.

Polysaccharides (like starch) are formed by the combination of a number of sugar molecules. They are large molecules and do no interfere in the cellular functions.

Cellulose which is another important polysaccharide is formed by the combination of lots of beta glucose molecules through condensation. Here the beta glucose molecules have to flip over to form the hydrogen bonding.

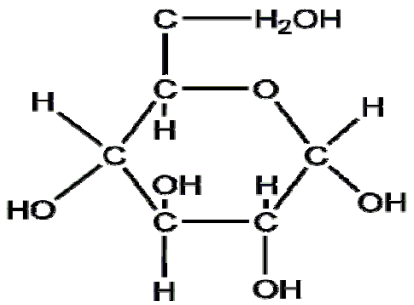

Fig. 3 Glucose. A form of carbohydrate and represents a single sugar unit (monosaccharide).

1.7.3 Lipids

Fats, oils, steroids (cholesterol) are lipids. They are two groups – triglycerides and phospholipids.

Triglycerides are formed by the combination of a glycerol molecule (Fig. 4(a)) and three fatty acid molecules through condensation. Fatty acids, as shown in Fig. 4(b), usually have a carboxyl group and the R represents a long hydrocarbon range.

Phospholipids are structurally similar to triglycerides. They are formed from a combination of 2 fatty acids, glycerol and a phosphate group.

Fig. 4(c) shows the structure of a phospholipid biological molecule with the fatty acid end being hydrophobic and the phosphate end being hydrophilic. This property is important for plasma membranes.

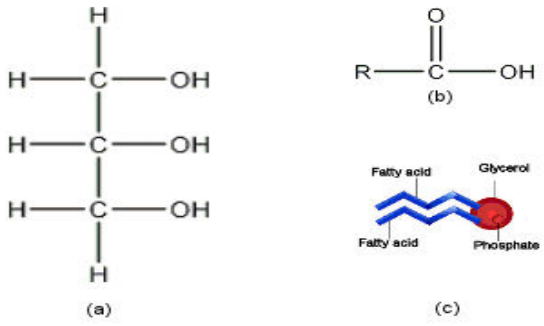

Fig. 4 Lipids. (a) Glycerol (b) Fatty acids consisting of a carboxyl group (COOH) and a long hydrocarbon chain R. (c) Phospholipids are formed from a combination of 2 fatty acids, glycerol and a phosphate group.

1.7.4 Nucleotides

Nucleotides are the building blocks for DNA. Each nucleotide is made of three molecular groups – a deoxyribose sugar (a pentose sugar) containing 5 carbon atoms, a phosphate group and a base that can be adenine, guanine, thymine or cytosine. Adenine and guanine are purines and are larger than thymine or cytosine, which are pyrimidines.

A number of nucleotides can be joined together through the process of condensation to make a polynucleotide. A DNA is formed by the combination of two polynucleotides. The structure is in the form of a ladder with the bases forming the rungs. Adenine always pairs with thymine and guanine always pairs with cytosine. The bases are held by hydrogen bonds. The helical shape of the DNA is shown in Fig. 5.

Like DNA there are 4 different nucleotides for RNA. It consists of three molecular groups – a ribose sugar (pentose), a phosphate group and a base that can be adenine, guanine, uracil or cytosine. These 4 different nucleotides form a polynucleotide as in the case of DNA. However, RNA is formed by a single strand of polypeptide unlike the DNA which has two polypeptides.

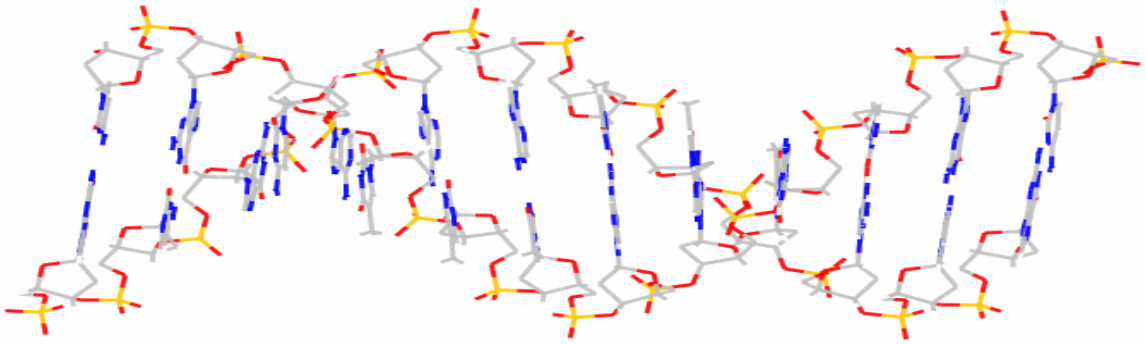

Fig. 5 Helical shape of the DNA.

1.7.5 Examples of biological molecules

a) Bacillus anthracis (1)

It is a gram positive, rod shaped, spore forming bacterium. The bacterium forms a poly-d-glutamic acid wall around it once it enters the host cell. This wall impedes the host immune system. D-glutamic acid has the structure as shown in the Fig. 6(a) below. It has the chemical formula $C_5H_9O_4$.

D-glutamic acid is an enantiomer (a mirror image) of L-glutamic acid.

b) Alanine and Glycine

These are the simplest of the amino acids and have the structure as shown in Fig. 6(b) and Fig. 6(c). Alanine has the chemical formula $C_3H_7NO_2$ and glycine has the chemical formula $C_2H_5NO_2$.

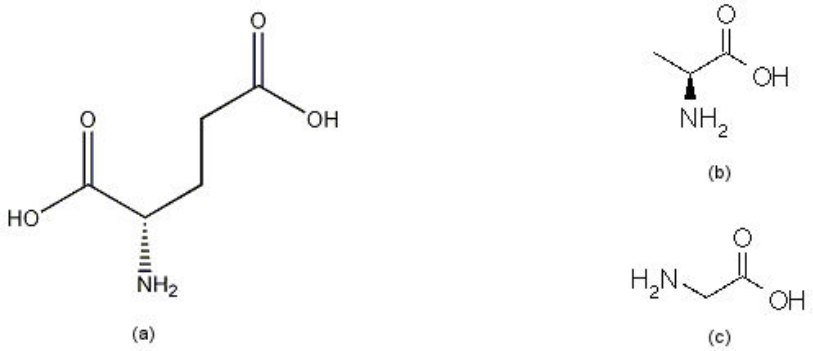

Fig. 6 Examples of biomolecules. (a) Poly-d-glutamic acid, a wall formed around bacillus antracis bacteria to protect itself against the host immune system. (b) Alanine, an amino acid (c) Glycine, an amino acid.

2. BASIC THEORY

2.1 Introduction to theoretical chemistry methods

Theoretical chemistry uses theoretical basis to explain chemical phenomena. In recent times quantum mechanics has gained a lot of prominence and acceptance in explaining such phenomena. To use the theoretical chemistry in an applied setting various methods are available, with a certain degree of approximation, such as ab initio methods like Hartree Fock method, Density Function Theory, etc:-, semi empirical methods, molecular mechanics and molecular dynamics. The degree of system complexity that can be handled increases as one moves from the ab initio methods to molecular mechanics and molecular dynamics.

2.1.1 Ab initio methods

Ab initio methods as the name suggests are methods that can be used to analyze a system using first principles. These methods however can handle only simple systems usually consisting of a couple of hundred atoms. Some of the ab initio methods are explained below.

2.1.1.1 Hartree Fock method

Hartree Fock method is one of the basic ab initio methods available to find the orbitals of a many electron system. It finds the orbitals by minimizing the energy of the system.

For a doubly occupied (closed shell) multi-electron system the determinantal wavefunction is given by

$$\varepsilon(1,2,.....,2N) = |\phi_1\overline{\phi_1}\phi_2\overline{\phi_2}.....\phi_N\overline{\phi_N}| \quad (1)$$

ϕ_1 is a spatial orbital with a α spin orbital and $\overline{\phi_1}$ is a spatial orbital with a β spin orbital and so on.

The total energy of closed shell N spatial orbitals is given by

$$E = 2\sum_{i=1}^{N} \in_i^{(0)} + \sum_{i,j}^{N} (2J_{ij} - K_{ij}) \quad (2)$$

The first summation term is the energy the atom would have in the absence of electron repulsion and the second summation term is the energy due to the electron repulsion. If the determinantal wavefunction is known then it is possible to find the total energy using (2).

The Hartree Fock method uses the Hartree Fock equation (matrix equation) as a basis for calculating the molecular orbitals. It is given by

$$\hat{F}\phi_i = \in_i \phi_i \quad (3)$$

where,

$\hat{F}$ is known as the Hartree Fock operator.

ϕ_i is a set of orbitals.

$\{\in_i\}$ is called the Hartree Fock Eigenvalues and orbitals ϕ_i are the corresponding eigenvectors.

Self consistent field method is one of the basic methods that is used to solve the Hartree Fock Equation. The idea is to begin with an initial set of orbitals and calculate the Hartree Fock operator for the particular set. Using the Hartree Fock equation a new set of orbitals (field) is calculated and the calculation is repeated. After a certain number of steps it is seen that the previous set of orbitals or field is approximately equal to the new set of orbitals or field obtained and consequently one can say that a self consistent field has been reached. This set of orbitals can now be used to calculate the wavefunction and the total energy of the many electron system.

Generally not all atoms and molecules can be described in terms of doubly occupied orbitals i.e. closed shell systems. To analyze open shell systems variations of the closed shell Hartree Fock equation is used. Two methods are available - restricted Open-shell Hartree Fock (ROHF) method and the unrestricted Hartree Fock (UHF) method.

In the ROHF method, doubly occupied orbitals are used as far as possible and singly occupied orbitals are used for unpaired electrons whereas in the case of UHF method each electron is assigned to a different orbital.

One of the drawbacks of the Hartree Fock method is that it assumes the electrons to be acting independent of one and another. Thus the effects of electron correlation are generally neglected. This may give rise to a energy value that deviates from the one determined by exact solution of the Schroedinger equation.

2.1.1.2 Moller Plesset method

As mentioned before one of the drawbacks of Hartree Fock method is that it neglects electron correlation. To overcome this drawback Moller and Plesset suggested a method that implements perturbation theory to incorporate electron correlation [31]. Perturbation theory helps to describe a complex system in terms of a simple one. We begin with an unperturbed Hamiltonian and go on adding additional Hamiltonians representing weak perturbations till the complex system is mathematically represented.

The unperturbed Hamiltonian operator is now combined with a small perturbation $\hat{V}$ and expressed as

$$\hat{H} = \hat{H}_0 + \lambda \hat{V} \tag{4}$$

Where λ is a parameter

The wavefunction ψ and energy E for weak perturbations can be expressed in terms of a power series as

$$\psi = \lim_{n\to\infty} \sum_{i}^{n} \lambda^i \psi^{(i)} \tag{5}$$

$$E = \lim_{n\to\infty} \sum_{i}^{n} \lambda^i E^{(i)} \tag{6}$$

Substituting the (5) and (6) in the schroedinger equation, $\hat{H}\psi = E\psi$, we get

$$(\hat{H}_0 + \lambda \hat{V})(\sum_{i}^{n} \lambda^i \psi^{(i)}) = (\sum_{i}^{n} \lambda^i E^{(i)})(\sum_{i}^{n} \lambda^i \psi^{(i)}) \tag{7}$$

The zero order solution corresponds to the Hartree Fock solution. The first order correction for energy is zero and the second order corrections is obtained from

$$E_0^{(2)} = \sum_{a>b;r>s} \frac{|< ab \,||\, rs >|^2}{E_0^{(0)} - (E_0^{(0)} + \varepsilon_r - \varepsilon_a + \varepsilon_s - \varepsilon_b)}$$

Where $E_0^{(0)}$ is the zeroth order correction energy,

a, b, r, s are the indices for spatial orbitals,

ε_r , ε_a , ε_s , ε_b are the orbital energies.

In recent years due to the availability of computing power one has been able to carry out expansions to orders greater than 2. It has been observed that at high orders the Moller-Plesset series can be convergent or divergent depending on the chemical system [32].

Moller Plesset comes with its own set of drawbacks. The convergence property can be slow, rapid, erratic, regular or oscillatory depending on the chemical system being studied and the basis set used. This has led to recent conclusions where Moller Plesset being a convergent theory is being doubted with suggestions to use other coupled cluster methods to achieve higher accuracy [33].

2.1.1.3 Configuration interaction

Using the orbital approximation the wavefunction for a many electron system can be written as a linear combination of slater determinants. Configuration interaction method helps us to include only certain slater determinants based on certain restrictions [34].

We begin with the wave function for an N electron system given by

$$\xi_i(1, 2, \ldots\ldots, N) = \sum_k^m \psi_k c_{ki} \tag{8}$$

where ψ_k = a linear combination of slater determinants and c_{ki} = variationally determined numerical coefficients.

Here each ψ_k represents an electronic configuration and the mixing of these electronic states gives rise to the interaction thus incorporating the electron correlation term in the wavefunction. This is also the reason behind the naming of the method.

The term ψ_k has certain restrictions that it must satisfy. If ξ_i is to be an approximation for a certain state of a system then ψ_k also needs to represent the particular state. For example, if we are considering the spectroscopic state of lithium given by $^2S_{1/2}$, then all the electronic configurations that give rise to that state like $1s^2 2s$ (forming the ground state), $1s^2 3s$,$1s^2 4s$ (forming the exited states) etc:- can be included. This means ψ_k should be an eigen function of the spin angular momentum operator $\hat{S}^2$ with the spin angular momentum S = ½. In addition to this each ψ_k must lead to L = 0 to give the $^2S_{1/2}$ state. The determinantal basis is composed of the ψ_k terms and the

solution of the m x m determinant gives m roots with the lowest representing the ground state and the rest representing the excited states, all of which have the same L,S and J quantum numbers.

The configuration interaction method provides accurate results because it omits certain determinants based on the above mentioned restrictions. The configuration interaction method can be used only for small systems because as the system gets more complex a large number of determinants need to be calculated which cannot be performed due to computing limitations. In addition, this method is computationally costlier than hartree fock and moeller plesset methods [35].

2.1.1.4 Density functional theory

Density Function Theory (DFT) is a quantum mechanical method that treats many-body systems in particular molecules and condensed phases using an approach which is different from the aforementioned methods. It is helpful is determining the ground state properties of metals insulators and semiconductors. In addition, it can also determine the ground state properties of complex materials like proteins and carbon nanotubes.

The theory was first suggested by Hohenberg and Kohn in 1964. The main idea that DFT uses is that it describes a system of electrons that are interacting with each other through a density and not it's many-body wavefunction [36]. Thus the electron density is used as the fundamental variable. The ground state of the system was then defined by the electron density which minimizes the total energy. Using the electron density one can then find out all other ground state properties like lattice constant, etc)

One of the most common implementations of DFT is the Kohn-Sham method. The Kohn-Sham equation expresses the effective potential experienced by the electrons as a function of electron density [37]. The effective potential includes the coulombic interactions (exchange and correlation interactions) between the electrons and the external potential. Coulombic interactions are very difficult to model. To simplify the approach local-density approximation is used. This approximation locally substitutes the exchange-correlation energy density of an inhomogeneous system by that of an electron gas evaluated at the local density. Subsequently better approximations for the exchange and correlation energy like Generalized Gradient approximation, Krieger-Li-Iafrate approximation have been developed depending on the type of substance property being analyzed.

In DFT the electron density for an N electron system is given by

$$n(\vec{r}) = N\int d^3r_2 \int d^3r_3 .....\int d^3r_N \psi^*(\vec{r},\vec{r}_2,\vec{r}_3,....\vec{r}_N) r_N \psi(\vec{r},\vec{r}_2,\vec{r}_3,....\vec{r}_N) \tag{9}$$

Therefore, given a ground state electron density $n_0(\vec{r})$, one can calculate the ground state wavefunction using the above relation.

$$\psi_0 = \psi_0[n_0] \tag{10}$$

Consequently, the ground state energy can be expressed as a function of $n_0(\vec{r})$,

$$E[n_0] = \langle \psi_0[n_0] | T + V + U | \psi_0[n_0] \rangle \tag{11}$$

Subsequently, the energy with respect to $n(\vec{r})$ is given by

$$E[n] = T[n] + V[n] + U[n] \tag{12}$$

where $V[n] = \int V(\vec{r}) n(\vec{r}) d^3 r$

Thus if one has accurate expressions of T[n] and U[n], the minimization of energy will yield the ground state density $n_0(\vec{r})$.

The minimization of energy functional is done by applying the Lagrangian method of undetermined multiplies [37]. The functional in the equation is written as a density functional of non-interacting particles.

$$E_s[n] = \langle \psi_s[n] | T_s + V_s | \psi_s[n] \rangle \tag{13}$$

where T_s denotes the kinetic energy of the non-interacting electrons with density $n(\vec{r})$ and V_s is an external effective potential in which the particles are moving. If $V_s = V + U + (T - T_s)$, then $n_s(\vec{r}) = n(\vec{r})$.

The orbitals ϕ_i are then determined by solving iteratively solving the Kohn-Sham equations of the non interacting system

$$\left[-\frac{\bar{h}}{2m} \nabla^2 + V_s(\vec{r}) \right] \phi_i(\vec{r}) = \varepsilon_i \phi_i(\vec{r}) \tag{14}$$

The electron density is then given by $n(\vec{r}) = \sum_{i}^{N} |\phi_i(\vec{r})|^2$ (15)

Usually one starts with $n(\vec{r})$, then calculates V_s and solves the Kohn-Sham equations for ϕ_i. From these a new electron density is calculated and the process is repeated till convergence is reached.

One of the main drawbacks of DFT is that it is able to provide only the ground state properties. In addition one needs to accurately and reliably determine the exchange and correlation energies, which amounts to a huge computational cost. Approximations have been developed to solve this problem. However, depending on the property being calculated one needs to apply different approximations.

In order to determine excited electronic states various approaches are being considered in conjunction with DFT. One of approaches is to use Time Dependent Density functional theory (TDDFT). This approach requires the development of better TDDFT potentials in order to determine the excitation properties accurately [38].

2.2 Molecular dynamics

Molecular dynamics is based on classical mechanics unlike the theories we have discussed earlier which are based on quantum mechanics. It is specifically a computer simulation technique. Equilibrium properties of an atomistic or a molecular system are numerically calculated by solving the Newton's equation of motion. Based on Bolztmann's Ergodic hypothesis [39], for large systems one can determine the physical properties of a substance by treating it as a statistical ensemble and taking the average of

the physical properties measured over a sufficient length of time. Extending this to molecular dynamics, the molecular dynamics simulation provides the value of a physical property at different points in time. Hence taking an average of all these values over time will yield an equilibrium expression for the physical property.

Molecular dynamics simulations were first used by to study the phase transition of a hard sphere system [40]. Later potential functions for intermolecular interactions were developed and applied to water [41]. The first simulation for biomolecules was that of the bovine pancreatic trypsin inhibitor [42] and today one finds molecular dynamics simulations being run for complex proteins, DNAs, etc:-. The exponential growth in the computing power is also providing a much needed impetus to conduct molecular dynamics simulations.

Based on Newton's equation of motion,

$$F_i = m_i a_i \tag{16}$$

Where F_i is the force acting on particle i, m_i is the mass of the particle i and a_i is the acceleration of the particle i.

Also, expressing force as a gradient of the potential energy, we have

$$F_i = -\nabla_i V \tag{17}$$

Where V is the potential energy.

In order for the atoms in the simulation to experience forces as they would in reality, a proper choice of potential is very important. The potential is usually a function of the positions of the nuclei and is constructed by considering the relative positions of atoms

with respect to each other. One of the most commonly used potential functions is the Lennard Jones pair potential.

Combining (16) and (17), we have

$$-\frac{dV}{dr_i} = m_i \frac{d^2 r_i}{dt^2} \tag{18}$$

Thus knowing the derivative of potential, one can find the position of a particle at various time instances.

Let us consider a simple application where the acceleration of a particle is constant.

Acceleration, $a = \frac{dv}{dt}$ (19)

After integrating velocity at time t is given by,

$$v = a.t + v_0 \tag{20}$$

Similarly position at time t is given by,

$$r = v.t + x_0 \tag{21}$$

Using (16) and (17), we have

$$a = -\frac{1}{m}\frac{dV}{dr} \tag{22}$$

Thus if we know the initial position of the particle, its initial velocities and the acceleration which is determined by the potential gradient, then one can find out the

positions and velocities of the particle at all other times t. In effect this mechanism can be scaled to a number of particles.

Initial positions are determined using experimental techniques like X-ray crystallography. Initial velocities are randomly determined using Maxwell Boltzmann or Gaussian distribution at a given temperature with the restriction that the overall momentum of the system is zero.

Subsequently, knowing the particles position and momenta one can determine various physical properties of interest. For instance, for a simulation that has M configurations with N particles the average kinetic energy is given by

$$K = \langle K \rangle = \frac{1}{M} \sum_{j=1}^{M} \left\{ \sum_{i=1}^{N} \frac{m_i}{2} v_i v_i \right\}_j$$

Where v_i is the velocity determined at different instances of time.

As mentioned before the potential energy is a function of the positions of the nuclei. Therefore for a system of N atoms, the potential energy is a function of 3N positions. One needs an integration algorithm to integrate the equations of motion. Some of the available algorithms are the verlet algorithm, leap-frog algorithm, velocity verlet and beeman's algorithm [43]. While choosing the algorithm to be implemented one needs to make a trade-off among precision, storage space and complexity of the algorithm.

Molecular dynamics simulations have the capability to model systems containing thousands of atoms but they come with limitations too. Some of the limitations are

neglect of quantum effects, lack of the potential chosen to adequately replicate the forces acting on the atoms, time of size limitations when the system being modeled is very large.

There are a large number of programs available for molecular dynamics simulations. Some of them using classical physics to evolve the system are AMBER, CHARMM, DL_POLY, GROMACS, NAMD, etc. In these programs the effect of nuclei and electrons have been strongly simplified (averaged) by a force field between centers normally representing the atomic centers. Although, as expected, these methods fail tremendously for local effects such as those of interest for chemistry, they provide excellent information about macroscopic or bulk characteristics as the average process seems to be correct. On theother hand, there is also a good number of programs where forces are calculated using electrons through solving in a very simplified manes the Schrödinger equation such as CPMD, VASP, Gaussian03, etc. In these programs the nuclei dynamics is still ruled by Newtons Laws, the forces at the atomic sites are evaluated using Schrödinger equation. Each software has its own advantages and disadvantages. In addition some of them maybe suited for a particular kind of system modeling. However, the underlining factors for all the molecular dynamics simulation programs are the maximum size of the model that can be simulated, simulation time and accuracy of the modeling results. Most of the programs are now implementing parallel processor architectures to achieve high computational speeds. With further increase of computational power one can envisage software run times to get lesser and lesser.

3. METHODOLOGY AND TECHNIQUES

3.1 Enhancement of signals

One of the essential attributes of a sensor is that it should be able to detect minute quantities of the analyte. In fact the sensor should be able to detect a single molecule. However, at those atomic scales there are significant issues to be addressed. One of the issues is that of enhance of signals. Specific to our case where we will be using optical method of detection, the most common and effective way to enhance signals is by using the resonant Raman scattering and surface enhanced Raman scattering. The enhancement provided by surface enhanced Raman scattering is much more than that provided by resonant Raman scattering.

The basis for resonant Raman scattering is that when the incident radiation is in the frequency of a molecule's electronic spectrum then the Raman scattering intensity is increased by an order of magnitude of 2 to 4. The incident radiation has to have a frequency which is nearly equal to the first electronic transition of the molecule.

In the case of surface enhanced Raman scattering when a molecule is adsorbed on a metal like Ag, Cu, Au then the Raman scattering intensity increases by a large factor. Two empirical mechanisms come into play to explain this effect a) surface plasmon resonance b) charge transfer between metal and molecule that cause electronic transitions and thus results in resonance Raman scattering. A theoretical explanation based on ab initio theories has been recently provided [44], indicating that the enhancement is due to the extremely large cross section of the surface than the cross section of the isolated molecule; thus if the frontier molecular orbitals of the molecule

mixed with those of the surface (delocalization) the spectrum lines of the molecule show up in the spectrum of the complex surface-molecule. Surface plasmon resonance (SPR) is a process where the conduction electrons on the metal surface are elevated to extended surface excited states due to which the molecules on the metal surface experience a large electromagnetic field. The vibration modes perpendicular to the surface are strongly enhanced. SPR depends on the wavelength of the incident light and the morphology of the metal. The frequency of the incident light should be close to the plasma frequency of the metal.

Active research is being conducted to develop methods to achieve large enhancement of signals using surface enhanced Raman scattering. It has been observed that when molecules are adsorbed on a silver surface having a self similar fractal topology the enhancement factor increases to a factor greater than 13 [45]. A fractal is a self similar structure whose geometrical and topological features look the same at different levels of magnification. The fractal characteristic of the surfaces causes the incident radiation to be localized to a small area thus resulting is significant enhancement.

Methods exist to achieve large enhancement factors through purely electromagnetic mechanism [46]. If we consider a metal particle then the enhancement factor is proportional to the product of fields $|E(\omega)|^2$ and $|E(\omega')|^2$ where w is the pump frequency w' is the stokes-shift frequency. In most cases the enhancement factor is considered to be proportional to the peak $|E|^4$ thus giving rise to hot spots for enhancement. The electric field is usually seen to be dependent on the structure of the metal. It has been observed that a combination of surface Plasmon excitations in metal dimers and the long

range photonic interactions arising in one dimensional nanoparticle arrays gives rise to a surface enhancement factor of 10^{13} at certain locations in the metal structure.

Efforts are also on to use a combination of scanning probe microscopy methods like AFM, STM, etc and Raman spectroscopy to achieve signal enhancement through the use of different tips such as silver coated tip, gold coated tip, etc:- that provide Plasmon resonance [47].

3.2 Lennard Jones potential

Lennard Jones potential (L-J potential) is used to describe the non bonded interactions between neutral atoms and neutral molecules. As shown from Fig. 7, at long distances the particles experience an attractive Van Der Waals and at short distances they experience a pauli repulsive force due to the overlapping of electron orbitals. John Lennard Jones proposed a simple mathematical model [48] to explain these interactions.

The L-J 6-12 potential is given by

$$V(r) = 4\varepsilon\left[\left(\frac{\sigma}{r}\right)^{12} - \left(\frac{\sigma}{r}\right)^{6}\right]$$

$$V(r) = 4\varepsilon\left[(\frac{\sigma}{r})^{12} - (\frac{\sigma}{r})^{6}\right] \tag{23}$$

where ε is the depth of the potential well and σ is the distance at which the potential is zero.

Alternatively the equation can also be written as

$$V(r) = E_{\min}\left[(\frac{r_{\min}}{r})^{12} - 2(\frac{r_{\min}}{r})^{6} \right] \tag{24}$$

Where $E_{\min} = \varepsilon$ and $r_{\min} = \sqrt[6]{2}\sigma$.

The first exponential term in the equation is used to describe the repulsion and the second exponential term is used to describe the attraction. Though one can explain the repulsion at short distances it is harder to explain attraction at larger distances. The attraction results from induced dipole-dipole moment interaction. Usually an atom is uncharged meaning the electron cloud is symmetrically distributed around its nucleus. But in a case where there undergo collisions or near collisions the situation is different. When two uncharged particles approach one another, their electron clouds undergo deformation. Thus a lack of symmetrical cloud leads to a formation of a dipole and each particle acquires an induced dipole moment. The short time that this moment lasts causes particles with dipoles to be attracted to each other. This called the Van Der Waals force.

It is important to note that the L-J potential is an approximate. The repulsion term is dependent exponentially on the distance but to improve computing speeds we just take it as the square of the attractive term. The L-J parameters can be determined to achieve results similar to experiments or from quantum mechanical theories. It accurately models nobel gases and provides good approximation with neutral atoms and molecules. NAMD uses the L-J potential as formulated in (24).

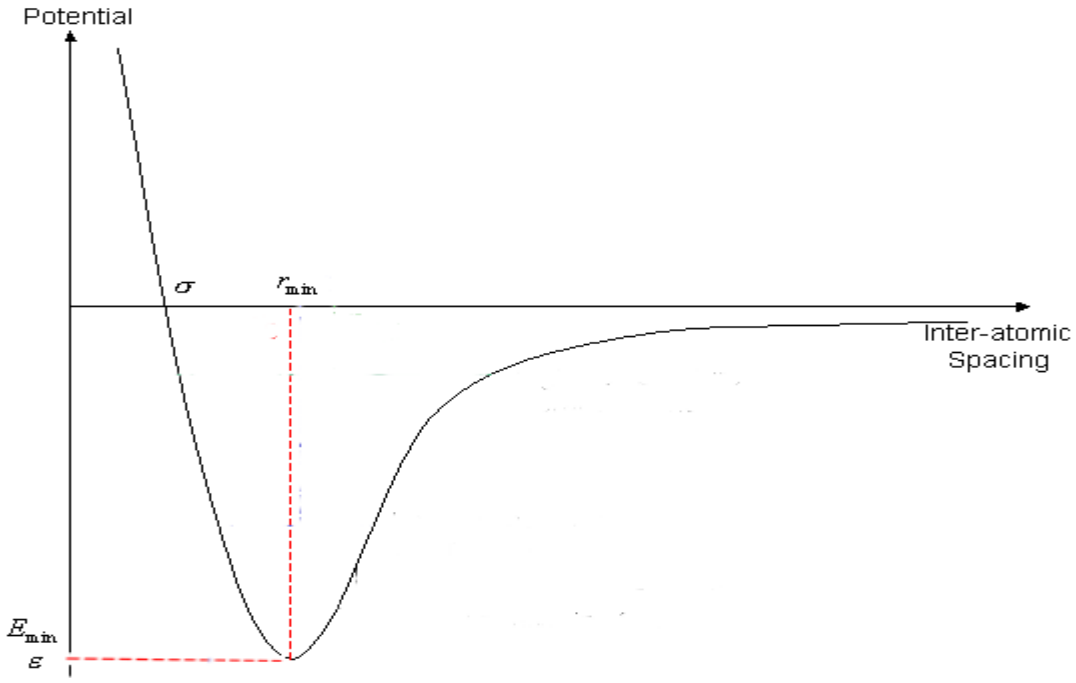

Fig. 7 Lennard Jones Potential.

3.3 Velocity autocorrelation function

The velocity autocorrelation function (VAF) is a time dependent function and provides information regarding the dynamics of the molecular system. For a particle, the velocity autocorrelation function is given by

$$C_i = \frac{1}{N-i}\sum_{n=1}^{N-i} v_{n+i} v_n$$

Where C_i is VAF at a certain time denoted by i, N is the total number of timesteps and v_n is the velocity of the particle at each timestep.

VAF provides a lot of information about the molecular system. It can give an idea about the interatomic forces present. In the presence of very weak forces, the velocity of the atoms remains the same and so the plot of VAF with respect to time will be a horizontal one.

On the other hand if the interatomic forces are strong like in solids and liquids, the VAF will oscillate between positive and negative values but will decay in time showing the evidence of damped harmonic motion. In the case of solids this happens because the atoms are closely packed and they seek positions where the attractive and repulsive forces are balanced. The atoms cannot easily escape from these positions and there the atoms oscillate reversing their velocity at the end of each oscillation. In the case of liquids since the atoms are free to move, the diffusion motion destroys any oscillatory motion. Therefore the VAF shows a damped oscillation with only one minimum.

In the case of gases where the interatomic forces are small but not negligible then the VAF plot shows an exponential decay. This means that the velocity and magnitude are changing gradually under the influence of weak forces.

In addition to the above information, the VAF can be fourier transformed to determine the underlying frequencies. Also one can determine the diffusion coefficient of the substance provided the VAF decays to zero after a long time (meaning velocity has decorrelated with time).

3.4 Fast fourier transform

Fourier theory states that any signal can be expressed as a sum of a series of sinusoids. This signal can be viewed from two different standpoints – frequency domain and time domain. The choice of domain depends on what we intend to do with the signal. For eg:- mathematics is much simpler in the frequency domain if we want to run some calculations on the signal. We can change from one domain to the other using the method of fourier transform.

The continuous fourier transform is defined by

$$f(\nu) = \mathcal{F}_t[f(t)](\nu) = \int_{-\infty}^{\infty} f(t)\, e^{-2\pi i \nu t}\, dt.$$

Discretizing the function $f(t) \to f(t_k)$ by letting $f_k \equiv f(t_k)$, where t_k = kΔ with k = 0,1,2 …N-1 gives the discrete fourier transform as

$$F_n \equiv \sum_{k=0}^{N-1} f_k\, e^{-2\pi i n k/N}.$$

The inverse transform is then

$$f_k = \frac{1}{N} \sum_{n=0}^{N-1} F_n\, e^{2\pi i k n/N}.$$

Fast fourier transform is an efficient way of computing the discrete fourier transform. It uses a divide and conquer approach reducing the number of computations needed for a N point sample from $2N^2$ to $2Nlg_2N$. It was first developed by Cooley and Tukey [49]. The algorithms fall into two classes – decimation in time and decimation in frequency. In most cases one uses the decimation in time class of algorithm. In the case of decimation in time class of FFT, the input data of N is converted into two transforms of N/2 length. The input data is then rearranged in a bit-reverse order and finally recombined to build the output transform. It is usually advised to have the sample size N to be a power of 2 in order to achieve high transformation speeds. A decimation in frequency algorithm follows similar steps but it first transforms and then rearranges the output values.

3.5 Potential energy function (CHARM22)

The form of potential energy function that NAMD uses is taken from CHARMM22. The potential energy function is dependent on the bonded, angle, dihedral, improper interactions and non bonded interactions like Van Der Waals and coulombic interactions. For our particular simulation, the potential energy function

$$V = V_{bond} + V_{angle} + V_{dihedral} + V_{improper} + V_{Urey\text{-}Bradley} + V_{vdw} + V_{coulombic}$$

$$= \Sigma\, k_b\,(b-b_0)^2 + \Sigma\, k_\theta\,(\theta-\theta_0)^2 + \Sigma\, k_\varphi\,[1+\cos(n\varphi-\delta)] + \Sigma\, k_\omega(\omega-\omega_o)^2 + \Sigma\, k_u(u-u_o)^2 + \Sigma\, \varepsilon\,[(r_o/r)^{12} - 2(r_o/r)^6] + q_iq_j/\varepsilon r_{ij}$$

V_{bond} accounts from the energy due to bond stretches, k_b is the bond force constant and $b-b_0$ is the distance from the equilibrium the atom has moved. V_{angle} accounts for the energy due to bond bending, k_θ is the angle force constant and $\theta-\theta_0$ is the angle between 3 bonded atoms. $V_{dihedral}$ is the term for dihedrals, k_φ is the dihedral force constant, n is the multiplicity of the function, φ is the dihedral angle and δ is the phase shift. Impropers i.e. is out of plane bending are considered using $V_{improper}$ term, k_ω is the force constant and $\omega-\omega_o$ is the out of plane angle. The Urey-Bradley component (cross-term accounting for angle bending using 1, 3 nonbonded interactions) is accounted for using the $V_{Urey-Bradley}$ term. k_u is the force constant and $u-u_o$ is the distance between the 1,3 atoms in the harmonic potential. V_{vdw}, $V_{coulombic}$ terms account for the non bonded interactions. We have already explained the Lennard Jones potential which is the basis for V_{vdw} term. $V_{coulombic}$ term is provided to consider the coulombic interactions, q_i and q_j are the charge on the i^{th} and j^{th} particle and r_{ij} is the distance between them, ε is the dielectric permittivity.

3.5 Damped harmonic motion

In physical systems, simple harmonic motion is an idealization. These systems usually have a dissipative force that reduces the system energy and amplitude of vibration. This damping force is usually proportional to the velocity. At low speeds we assume the damping force to be linearly proportional to the velocity. Therefore incorporating the damping force –cdx/dt into Newton's second law

$$\frac{d^2x}{dt^2}+\frac{c}{m}\frac{dx}{dt}+\frac{k}{m}x=0$$

Using a constant q the above equation can be further reduced to

$$\left(\frac{d}{dt}+\frac{c}{2m}+q\right)\left(\frac{d}{dt}+\frac{c}{2m}-q\right)x(t)=0 \qquad (25)$$

Where $q = [\gamma^2\text{-}k/m]^{1/2}$ and $\gamma = c/2m$.

Depending on the values of k, m and c, q can be real or imaginary. Therefore three situations arise

a) overdamping - q is real and greater than 0

The solution to (25) decays to zero and there are no oscillations

b) critical damping - q = 0

For critical damping also, the solution of (25) decays to zero without any oscillations

c) underdamping - q is imaginary

The solution to (25) shows an oscillatory behaviour. However the amplitude and the frequency are reduced when compared to the simple harmonic motion.

3.6 Spectral density

Spectral density is a general concept in signal analysis. For a stationary random process, the spectral density is the fast fourier transform of the sample function. The spectral density of a wave is closely related to the power carried by the wave per unit frequency. So it is also called as the power spectral density. We can also relate the

spectral density to the autocorrelation function since both terms arise from the fourier transforms. According to the Wiener-Khinchin theorem, the spectral density is the fourier transform of the autocorrelation function provided that the signal is a wide sense stationary random process [50].

For a wide sense stationary random process y[n] with an N-point sequence, the spectral density is given by,

$$S(\omega) = \frac{1}{N}\left|Y(\omega)\right|^2$$

$$Y(\omega) = \sum_{n=0}^{N-1} y[n] e^{-2\pi i \omega \frac{n}{N}}$$

where , is the fourier transform of y[n].

The spectral density plot is usually plotted against frequency. The plot shows how the power of the signal is distributed over the frequency range. If we integrate the area under the curve over the entire range then it gives the total power carried by the signal.

3.7 Lattice dynamics

Lattice vibrations in crystal are important to understand if we need to analyze the underlying frequency characteristics. Lattice vibrations can be understood by applying the harmonic approximation. The atoms of a crystal are considered to be moving about their equilibrium positions. We begin by analyzing lattice vibrations of one-dimensional

monatomic crystals. We consider only the interaction between the nearest neighbouring atoms and use the harmonic approximation to determine the relation between the frequency and wave vector. For vibrations with shorter wavelengths, the dispersion relation for the frequency is

$$\omega_k = \left(\frac{4J}{m} \right)^{1/2} \left| \sin \left(\frac{ka}{2} \right) \right|$$

Where J is the force constant between the neighboring atoms, m is the mass of the atom, k is the wave vector and a is the distance between the nearest neighbors. From the above relation we see that as k tends to 0, ω_k also tends to zero. The dispersion curves thus obtained are called the acoustic modes. There is another type of vibration that corresponds to the optical mode. In acoustic mode of vibration, the neighboring atoms vibrate in phase whereas in the case of the optical mode they vibrate out of phase.

4. RESULTS

The electrical, terahertz and optical (ETO) concept uses the electrical, terahertz and optical properties of a molecules to determine its terahertz absorption characteristics. In order to achieve strong terahertz absorption characteristics we consider the implementation of surface enhanced Raman scattering. The combination of the molecules and the substrate would constitute a complex system consisting of thousands of atoms. Therefore we have concluded that molecular dynamics software would be the best choice to model such a system. In particular we are considering NAMD that is suited for modeling large number of molecules and is implemented on parallel processor architecture for high computational speeds. We begin with preliminary calculations of simple molecules and then complex systems with a combination of different molecules will be analyzed.

4.1 Water dimer

We begin with a very simple system consisting of two water molecules as shown in Fig. 8. We model the non-bonded interaction between the water molecules with a Lennard Jones potential. The bonded interactions between oxygen and hydrogen are considered to be modeled on the basis of a harmonic potential. After performing energy minimization and equilibration of the water molecules, the molecular dynamics simulations are run with a time step of 1 fs. The simulations are run at a temperature of 310K.

The output files from the simulations are then used to determine the oxygen-hydrogen (O-H) bond lengths and Oxygen-Oxygen (O-O) interactions and subsequently the frequency spectrum of the O-H bond and the O-O interaction.

Fig. 9(a) shows the variation of the O-H bond length with time. The average O-H bond length over the entire simulation is calculated to be 0.9621 Å which correlates with the spectroscopically determined O-H bond length of 0.96 Å [51]. A fast Fourier transform of O-H bond lengths then gives the frequency spectrum as shown in Fig. 9(b). From the plot O-H bond frequency has a peak at 101.6 THz and the spectroscopically detemined frequency is at 3400 cm^{-1} (102 THz) [52]. Similarly the plot in Fig. 9(c) shows the length variations of the O-O interaction. The average length of the O-O interaction is calculated to be 2.842 Å. A fast fourier transform of these interactions gives the frequency content of these interactions with a peak at 5.615 THz as shown in Fig. 9(d).

Therefore we see that the frequency absorption characteristics of water are in the terahertz region.

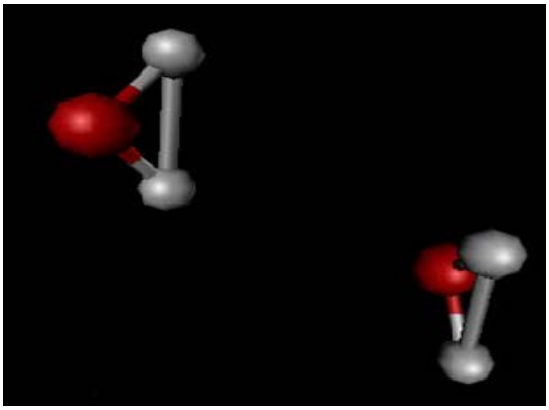

Fig. 8 Visualization of two water molecules using VMD software. Lennard Jones potential and harmonic potential are used for non-bonded and bonded intereactions respectively. Simulation carried out at 310 K.

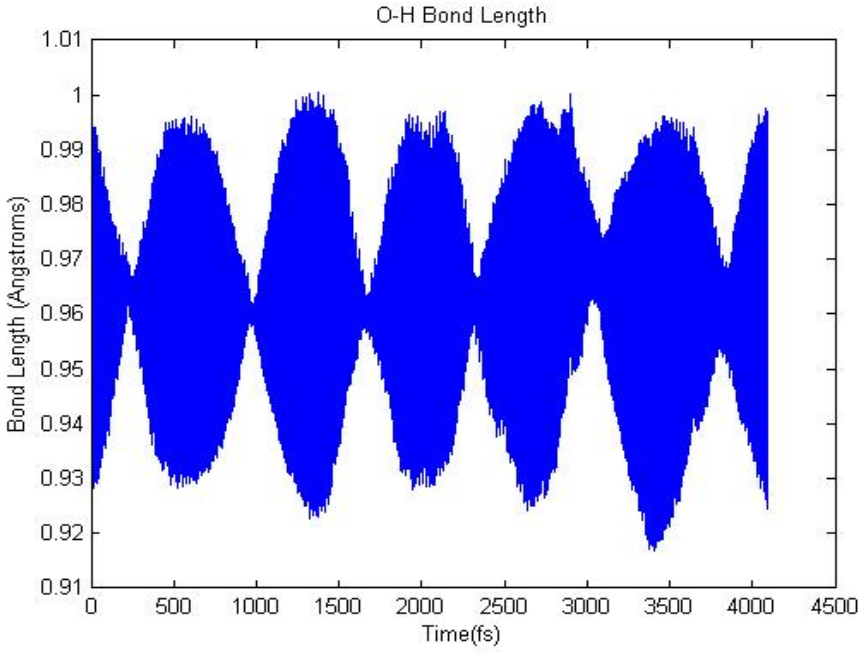

(a)

Fig. 9 Terahertz absorption characteristics of two water molecules. (a) Time domain variation of O-H bond length having an average bond length of 0.9621 Å. (b) Frequency content of the O-H bond with the peak at 101.6 THz.. (c) Time domain variation of O-O interaction length with average interaction length being 2.842 Å. (d) Frequency content of the O-O interaction with the peak at 5.615 THz.

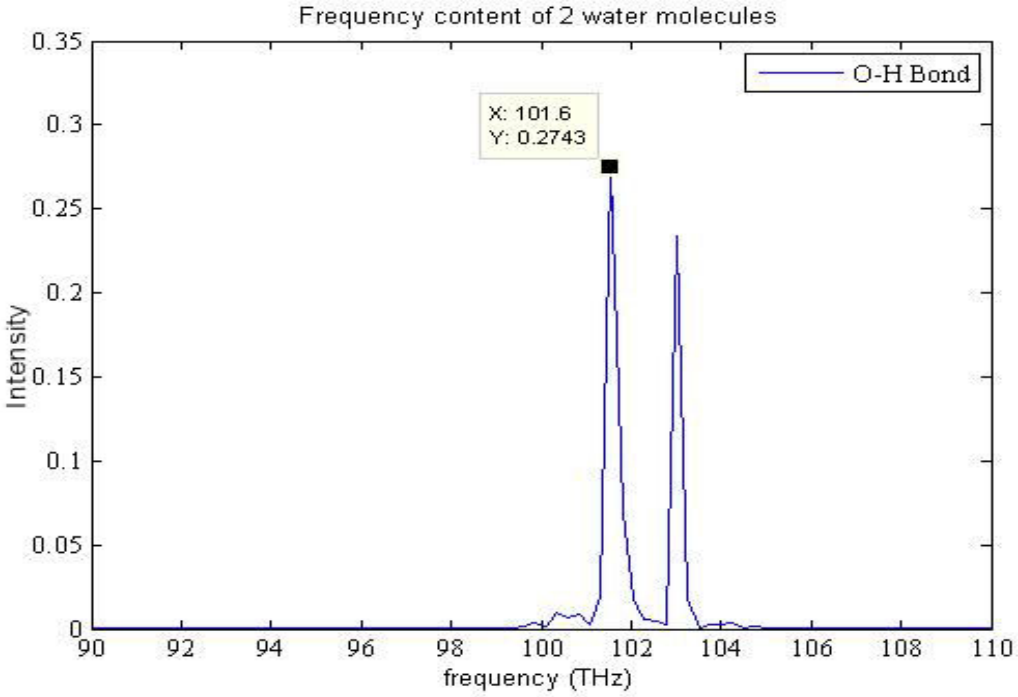

(b)

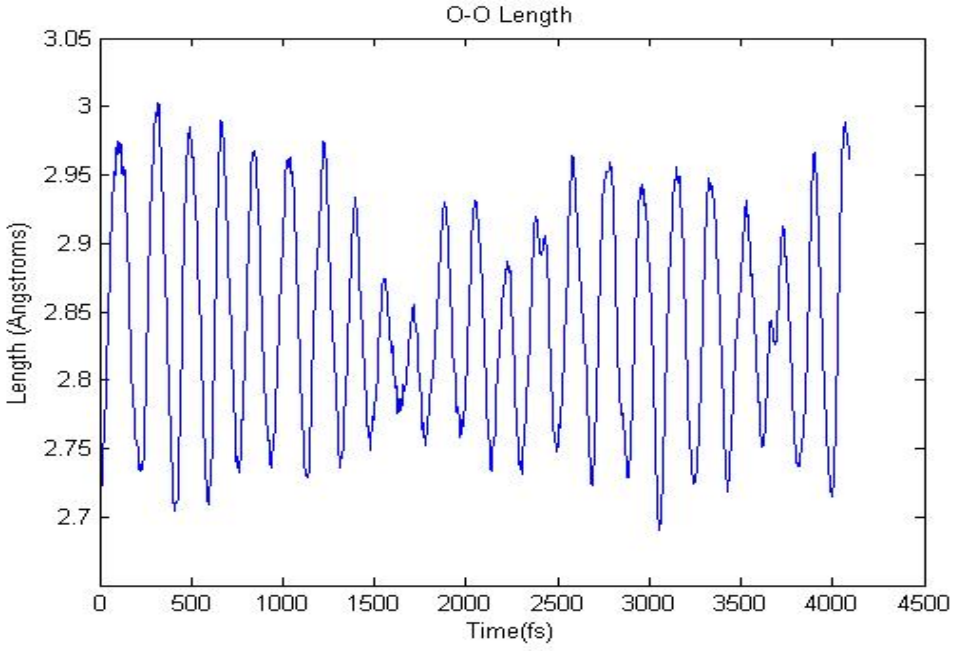

(c)

Fig. 9 continued.

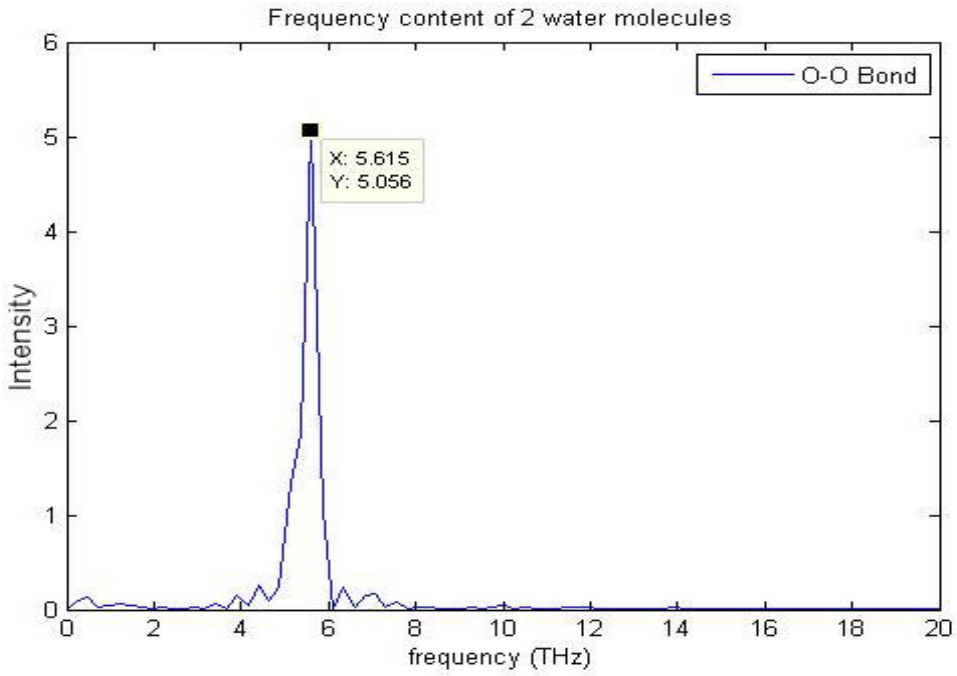

(d)

Fig. 9 continued.

4.2 Dodecane

Dodecane is an alkane with the chemical formula CH3-(CH2)10-CH3. It is also known as dihexyl, bihexyl, adakane 12, or duodecane. It is a thick oily liquid of the paraffin series and is used as a solvent and in the distillation process.

We are considering only a single molecule of dodecane for our simulation as shown in Fig. 10. The bonded interactions between the Carbon-Carbon (C-C) bonds and the Carbon-Hydrogen (C-H) bonds are based on the harmonic potential. We first perform the energy minimization followed by the equilibration. The molecular dynamics

simulations are run with a time step of 1 fs. The simulations are run at a temperature of 310K.

Similar to the analysis of two water molecules, the output files from the simulations are then used to determine the C-C and C-H bond lengths. These bond lengths are then used to determine the frequency spectrum of C-C and C-H bonds.

The analysis of output files gives us the variation of C-H bond length with respect to time as shown in Fig. 11(a). The average C-H bond length is 1.112 Å which is close to the experimental value of 1.09 Å [51]. The FFT of these bond lengths then gives us the frequency spectrum of the C-H bond. As seen from the plot in Fig. 11(b) the peak is observed to be at 90.07 THz which corresponds to the around 3000 cm-1 (90 THz) [53]. Similarly the plot in Fig. 11(c) shows the C-C bond length variations. The average bond length is calculated to be 1.531 Å which again is close to the experimentally determined value of 1.54 Å [51]. A fast fourier transform of these interactions gives the frequency content of this bond with a peak at 30.36 THz as shown in Fig. 11(d).

It is observed that the frequency spectra of the C-C and the C-H bonds belong in the terahertz region. Therefore using these absorption characteristics one can easily achieve signatures pertaining to the dodecane molecule.

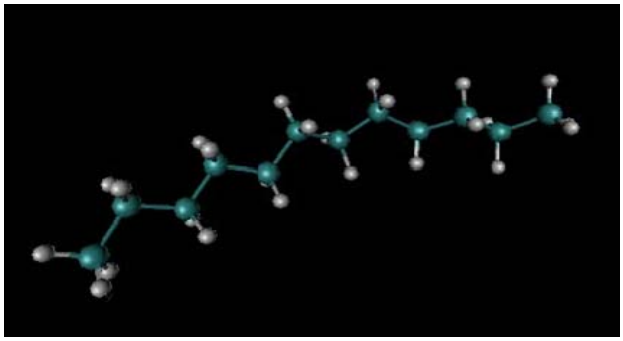

Fig. 10 Visualization of dodecane molecule using VMD software. Harmonic potential is used for bonded intereactions. Simulation carried out at 310 K.

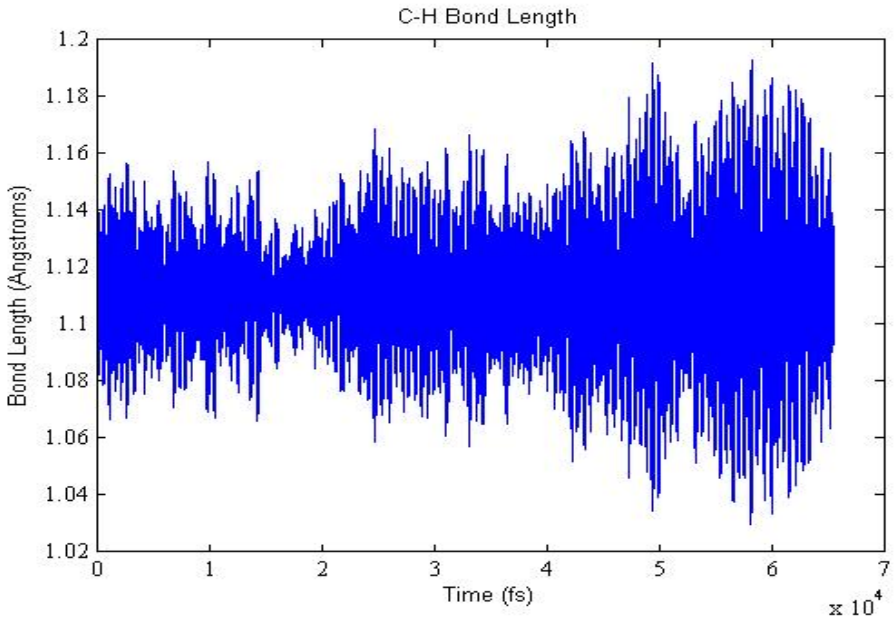

(a)

Fig. 11 Terahertz absorption characteristics of dodecane molecule. (a) Time domain variation of C-H bond length having an average bond length of 1.112 Å. (b) Frequency content of the C-H bond with the peak at 90.07 THz.. (c) Time domain variation of C-C bond length with average interaction length being 1.531 Å. (d) Frequency content of the C-C bond with the peak at 30.26 THz.

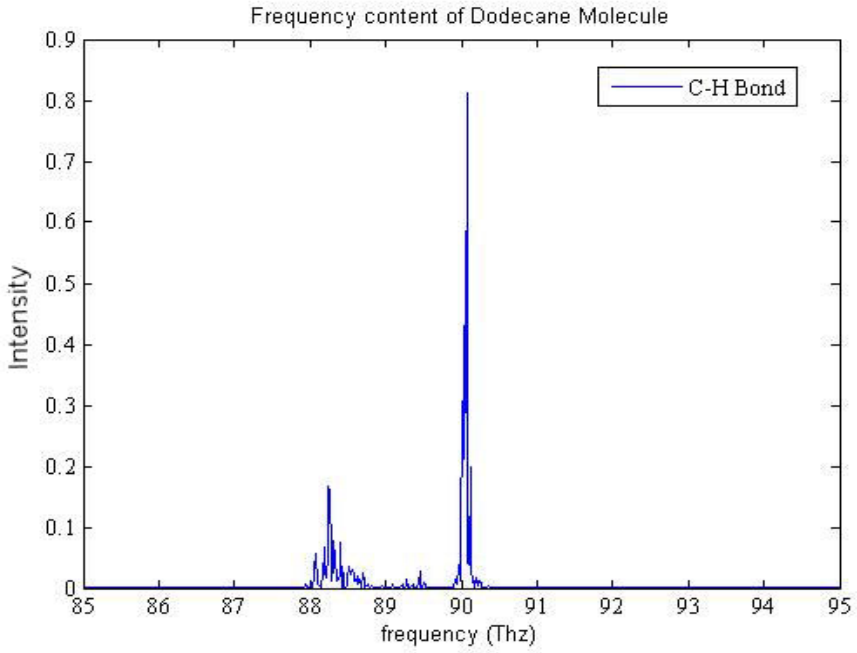

(b)

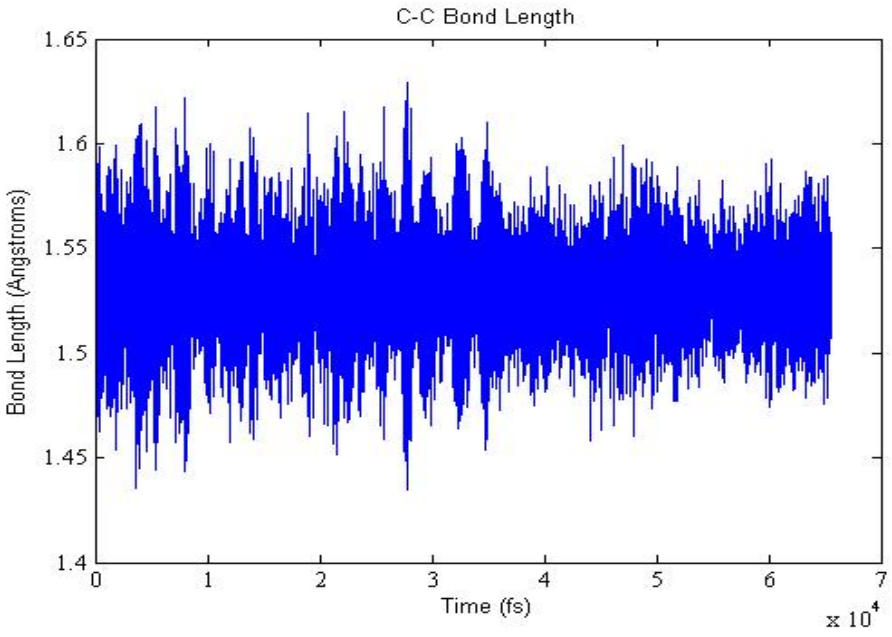

(c)

Fig. 11 continued.

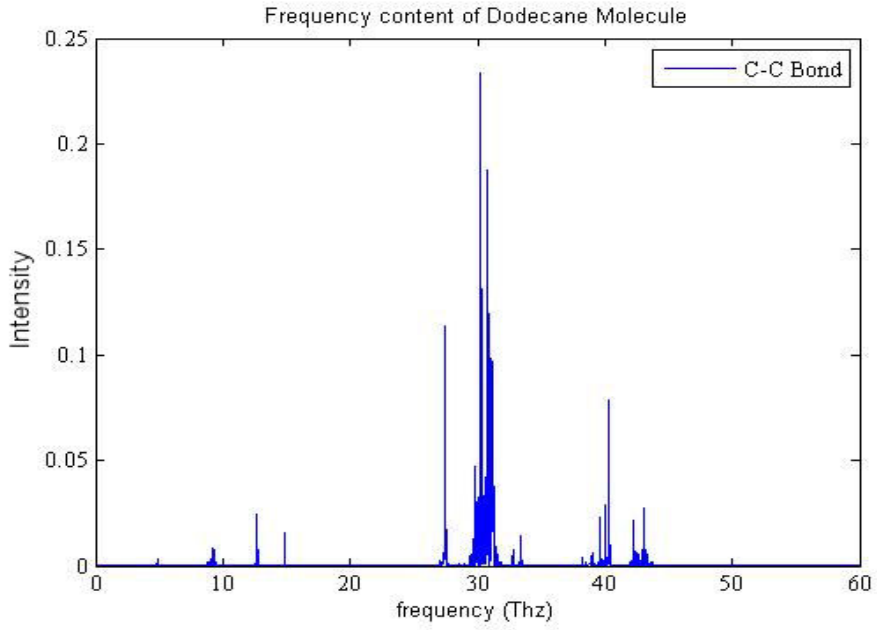

(d)

Fig. 11 continued.

4.3 Nitromethane

Nitromethane is the simplest organic nitro compound with the chemical formula CH_3NO_2, It is a highly polar, colorless, viscous liquid with a disagreeable odor. It is highly flammable and reacts with alkalis, strong acids, oxidizers and metallic oxides. It is widely used in the manufacture of pharmaceuticals, explosives, industrial antimicrobials, fibers and coating. When combined with ammonium nitrate it forms a potent explosive. Nitromethane is considered to be harmful if swallowed, inhaled or absorbed through the skin. It might cause cyanosis (condition where the skin turns blue due to an increase in unoxygenated hemoglobin). In addition it is also anticipated to be a human carcinogen [54].

Nitromethane being an energetic material has witnessed a lot of research being conducted on it. Various experimental [55, 56] and theoretical studies [57-59] have been performed in order to analyze the structure and frequency characteristics of nitromethane.

At this juncture we would like to develop a nanosensor for sensing traces of nitromethane molecules. Nitromethane when it undergoes thermal decomposition gives products consisting of traces of methyl nitrite and residual nitromethane among other susbtances. Physically our nanosensor shall consist of gold electrodes that will be used to interact with the analyte, in our case nitromethane and its decomposition products. In particular we believe that when gold electrodes interact with decomposition products it will produce a measurable change in the frequency characteristics of the gold electrode. In order to realize this nanosensor, we need to determine the frequency characteristics of nitromethane and simulate its thermal decomposition. Subsequently we need to analyze the frequency characteristics of our gold electrodes. Finally a simulation showing the interaction of gold and the decomposition products will be carried out to analyze the feasibility of our nanosensor.

Our approach has been to conduct molecular dynamics study of a certain number of nitromethane molecules using the NPT ensemble. The nitromethane molecules were simulated at ambient conditions of 300 K and 1 bar and the frequency characteristics of nitromethane was obtained and compared to the experimental results [55, 56].

4.3.1 MD simulation of 216 nitromethane molecules

We simulate a box of 216 nitromethane molecules and then conduct the frequency analysis of the CH, NO and CN bonds in order to determine the terahertz frequency characteristics of the nitromethane molecules.

4.3.1.1 Method

We build a cube with side 26.78 Å of these molecules after taking into consideration the density (1.139g/cm^3) and the molecular weight (61.04 gm/mol) of nitromethane.

The intermolecular force field parameters obtained from [58] were modified in order to tailor it to our specific molecular dynamics program (NAMD). We used NAMD molecular dynamics program with periodic boundary conditions to simulate the 216 nitromethane molecules. Langevin dynamics was used for maintaining both temperature (at 300K) and pressure (at 1 bar) in the NPT ensemble over the entire 130172 timesteps. The system was further analysed using a NVE ensemble in order to verify its equilibration by plotting energy and temperature over time. From Fig. 12 we see that the energy and temperature are fluctuating within reasonable limits showing that the system is well equilibrated. The simulation data is then used to determine to the average bond lengths of the CH, NO and CN bonds and subsequently a fast fourier transform algorithm is applied to determine the bond stretching frequencies of these three bonds.

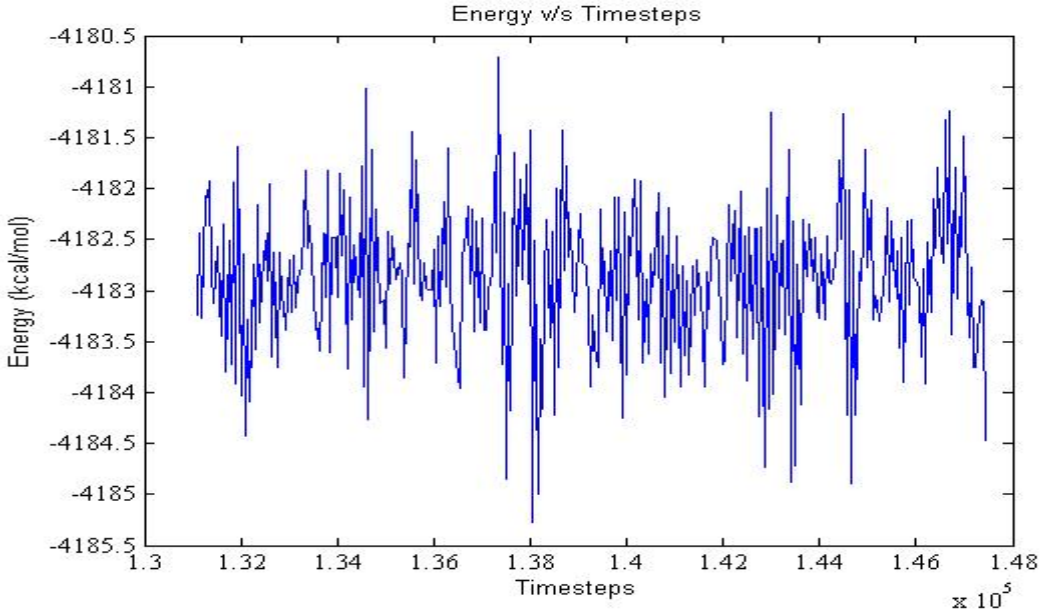

(a)

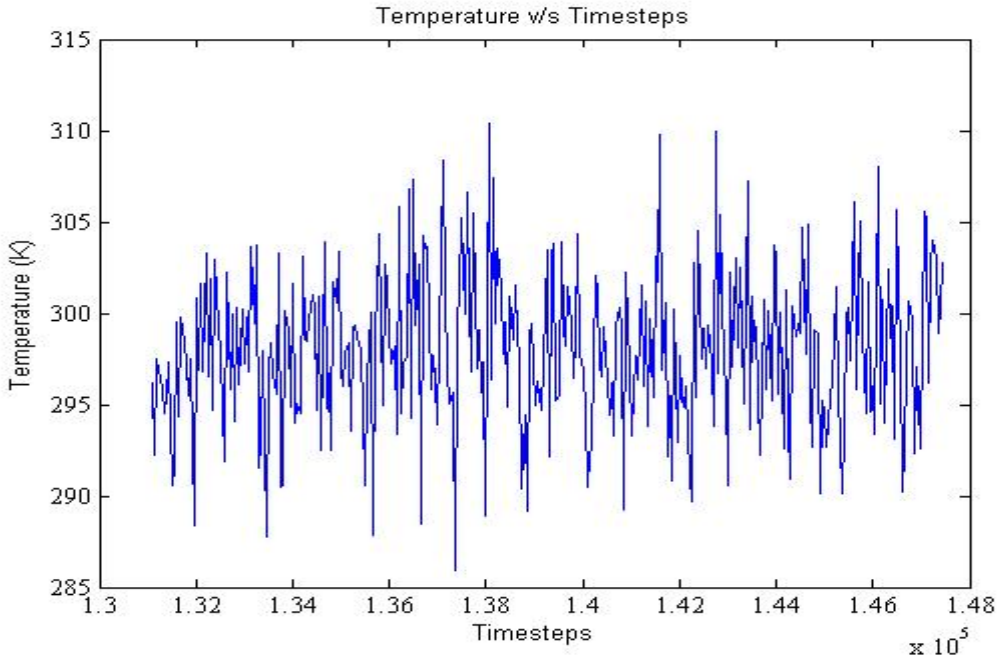

(b)

Fig. 12 Results from the NVE simulation of 216 nitromethane molecules. (a) Plot of energy over time steps (each time step is 1 femtosecond) (b) Plot of temperature over time steps. Both plots show that the system has equilibrated.

4.3.1.2 Results

The average bond lengths of CH, NO and CN bonds were found to be 1.1 Å, 1.49 Å and 1.26 Å respectively at ambient conditions. The bond lengths were found to be close to the experimentally determined equilibrium bond lengths [55, 56].

Fig. 13(a) shows the bond stretching frequencies of the CH, NO and CN bonds. The frequency spectrum generated by the simulation (NAMD) shows the internal modes. The frequency spectrum is qualitatively similar to the one reported in ref. [59]. Fig. 13(b) shows the frequency spectrum pertaining to the CH bond. The symmetric and anti-symmetric stretches at 3011 cm^{-1} and 3156 cm^{-1} are clearly visible. On comparison with the spectrum of the other two bonds it is evident that the CH bond is relatively less affected by the vibrations of the other bonds. Fig. 13(c) and Fig. 13(d) correspond to the frequency spectrums of CN and NO bonds respectively. As seen both spectrums show a peak at 828 cm^{-1} and 1377 cm^{-1}. The anti-symmetric stretching peak for NO bond is seen at 1532 cm^{-1} from Fig. 13(d). One can thus conclude that when considering a bond frequency spectrum it will contain the information regarding other bond frequencies as well.

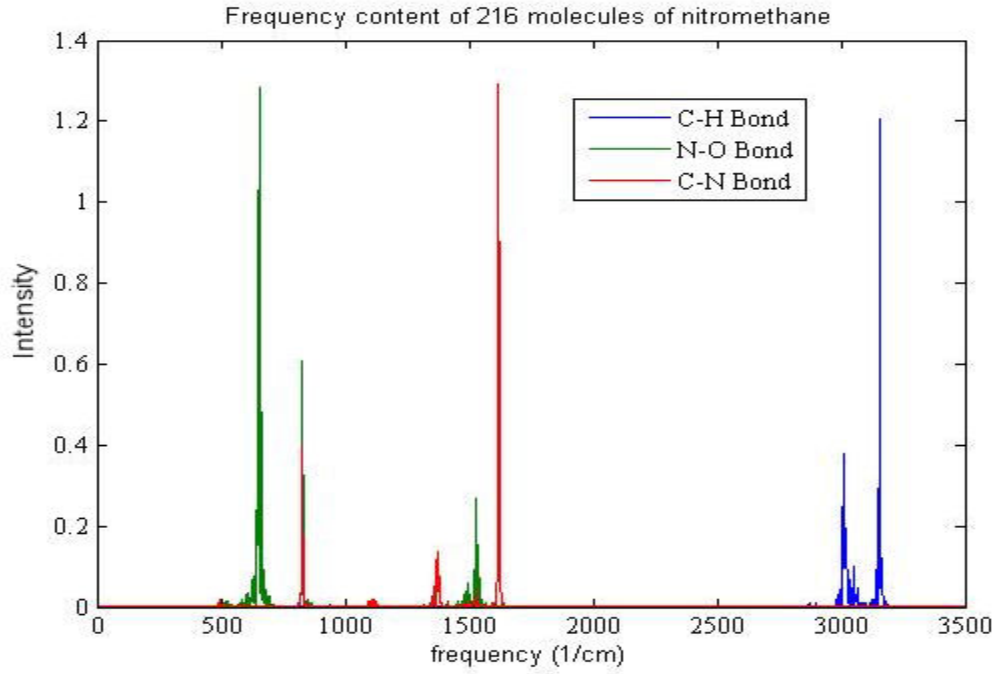

(a)

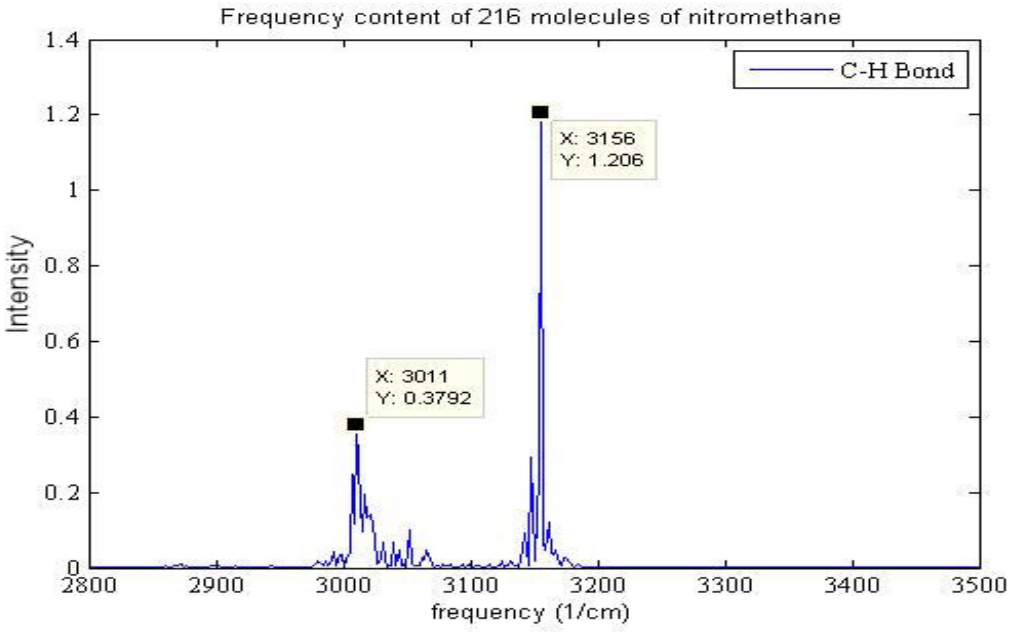

(b)

Fig. 13 Frequency spectrum of 216 nitromethane molecules at ambient conditions (300K and 1 bar). (a) Plot showing the internal modes (NAMD) of all the three bonds (CH, CN and NO). (b) Frequency Spectrum of CH bond with visible symmetric and anti-symmetric stretching peaks at 3011 cm^{-1} and 3156 cm^{-1}. (c) CN bond stretching frequency (d) NO bond stretching frequency with anti-symmetric peak at 1532 cm^{-1}.

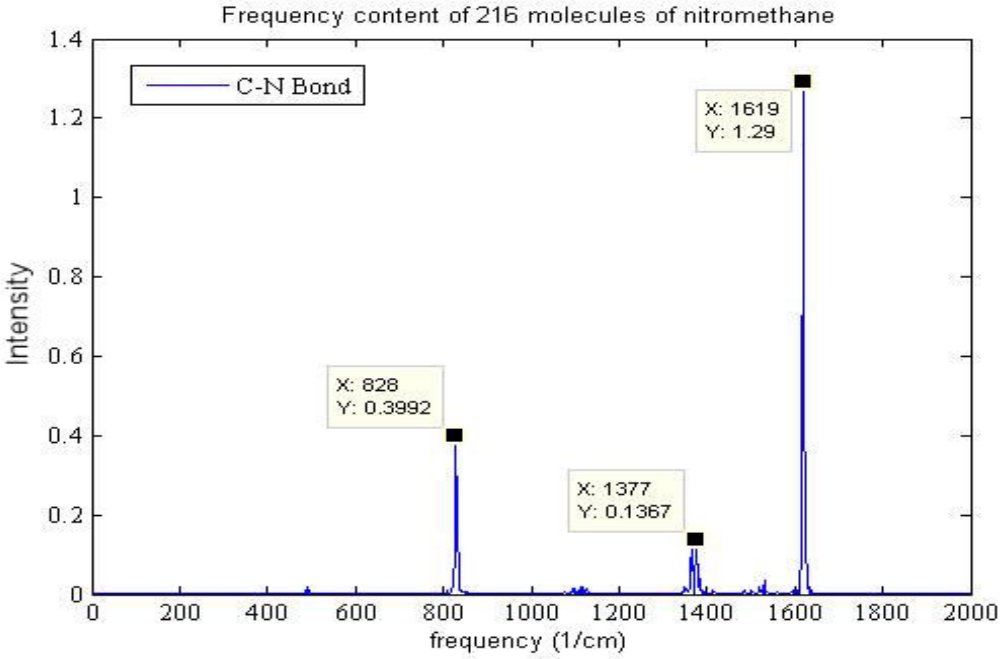

(c)

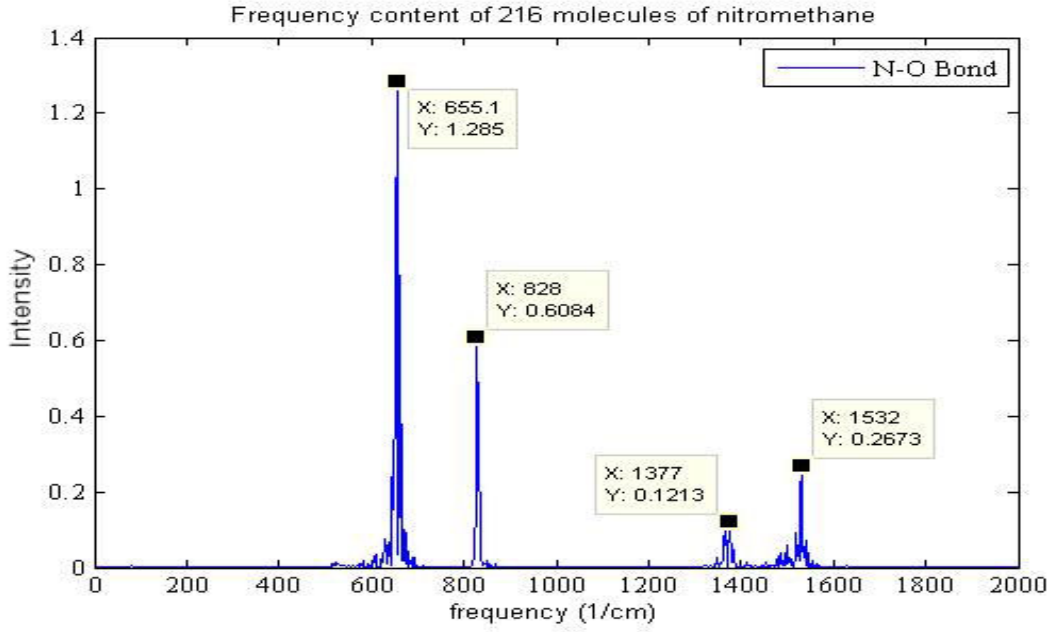

(d)

Fig. 13 continued.

4.3.2 MD simulation of 1000 nitromethane molecules

We now scale the nitromethane system to 1000 nitromethane molecules. As in our simulation for 216 nitromethane molecules, we simulate a box of 1000 nitromethane molecules and then conduct the frequency analysis of the CH, NO and CN bonds.

4.3.2.1 Method

The MD simulation for 1000 nitromethane molecules follows the same steps as that of the 216 nitromethane molecules case. A cube with side 44.65 Å is built after taking into consideration the density and molecular weight of nitromethane which are 1.139g/cm^3 and 61.04 gm/mol respectively. The intermolecular force field parameters that have already been established for the 216 nitromethane molecules run are used here. We begin with an NPT ensemble with periodic boundary conditions. The temperature is maintained at 300 K using Langevin dynamics and the pressure is maintained at 1 bar using Nose-Hoover Langevin piston control. The equations of motion are integrated using the Verlet leapfrog procedure with a timestep of 1 fs. The cutoff distance chosen was 12 Å and the long range electrostatic interactions were calculated using particle mesh ewald sum method. The NPT ensemble was run for 262144 fs. The system was further analysed using a NVE ensemble in order to verify its equilibration by plotting energy and temperature over time. From Fig. 14 we see that the energy and temperature are fluctuating within reasonable limits showing that the system is well equilibrated. The simulation data is then used to determine to the average bond lengths of the CH, NO and

CN bonds and subsequently a fast fourier transform algorithm is applied to determine the bond stretching frequencies of these three bonds.

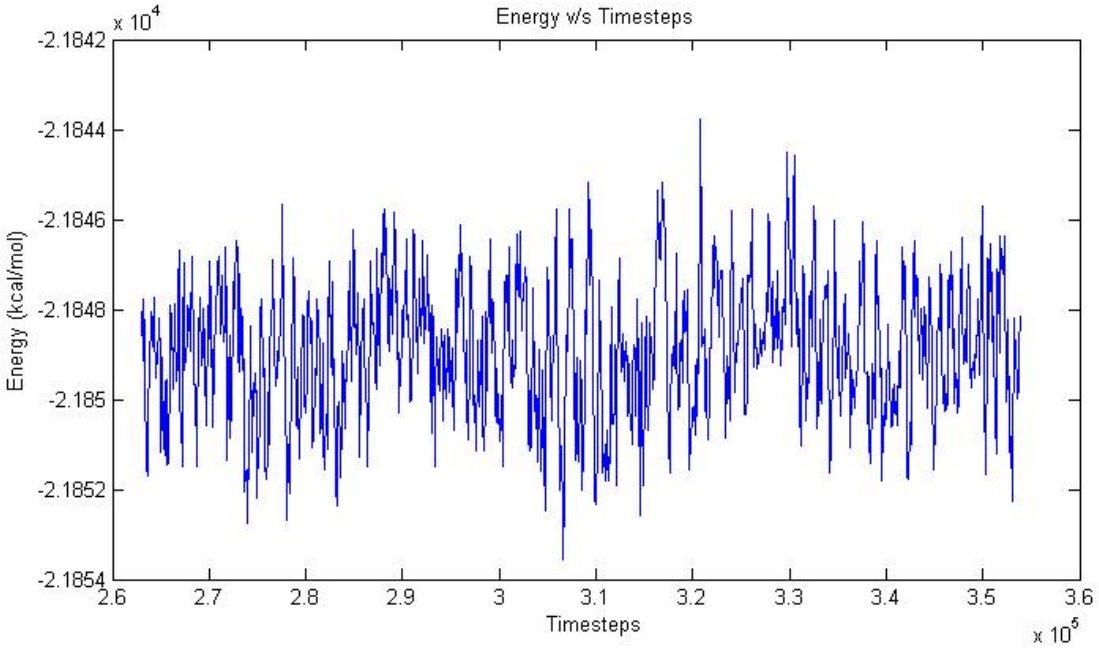

(a)

Fig. 14 Results from the NVE simulation of 1000 nitromethane molecules (a) Plot of energy over time steps (each time step is 1 femtosecond) (b) Plot of temperature over time steps. Plots show that the system has equilibrated.

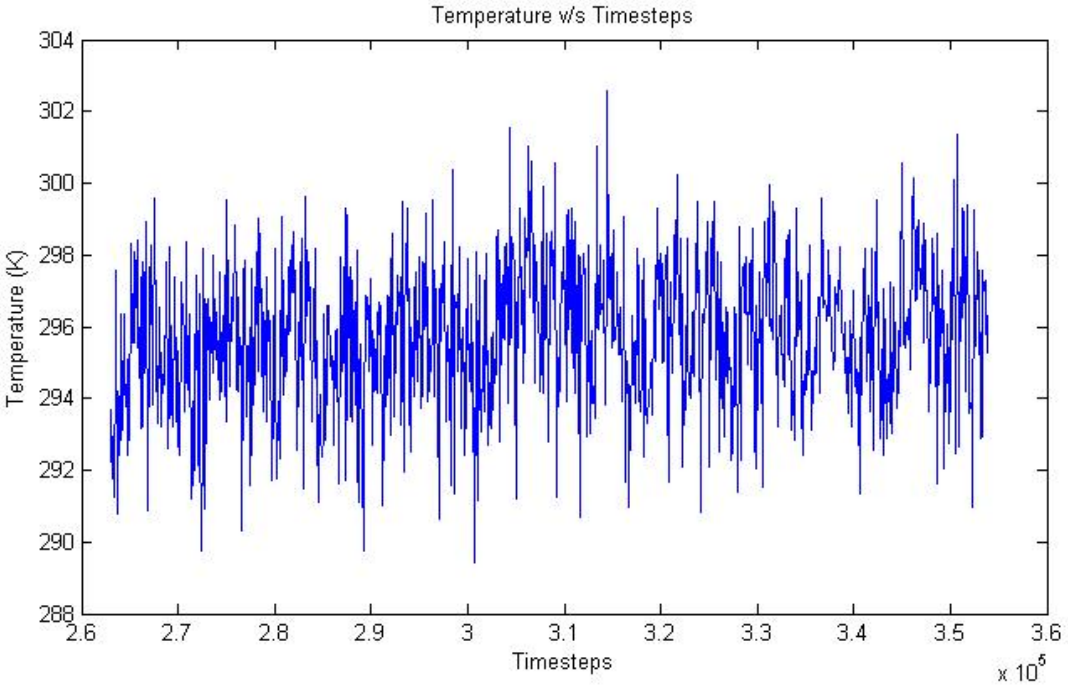

(b)

Fig. 14 continued.

4.3.2.2 Results

The average bond lengths for the CH, NO and CN bonds were found to be 1.08 Å, 1.49 Å and 1.23 Å respectively and agreed with the experimentally determined bond lengths [55, 56].

Fig 15a shows the frequency spectrum of 1000 nitromethane molecules. The plot is similar to the frequency spectrum of 216 nitromethane molecules shown in Fig. 13(a). The internal modes shown in Fig. 15(a) are qualitatively similar to the one reported in ref. [59]. The symmetric and anti-symmetric stretches at 3011 cm^{-1} and 3158 cm^{-1} are evident in Fig. 15(b). As seen in the case of 216 nitromethane molecules, we see from Fig. 15(c) and Fig. 15(d) that both have peaks at 830 $cm^{-1}$and 1375 cm^{-1} respectively

indicating that the frequency of CN and NO bonds affect each other. The CH bond frequency though is relatively unaffected by the vibrations of the other bonds. The anti-symmetric stretching peak of NO bond at 1514 cm^{-1} can be seen from Fig. 15(d). When we compare the frequency spectrums of the individual bonds for the 1000 nitromethane molecules with the corresponding frequency spectrum for the 216 nitromethane molecules, we see that the peaks are identical with a very small variation in the values. However, there is a considerable difference in the intensity of the spectrum which we attribute to the sample data that we use from the simulation. In any case, one can conclude from both 216 and 1000 nitromethane molecules simulations that a frequency spectrum for a bond will carry information regarding the frequency spectrum of other bonds as well.

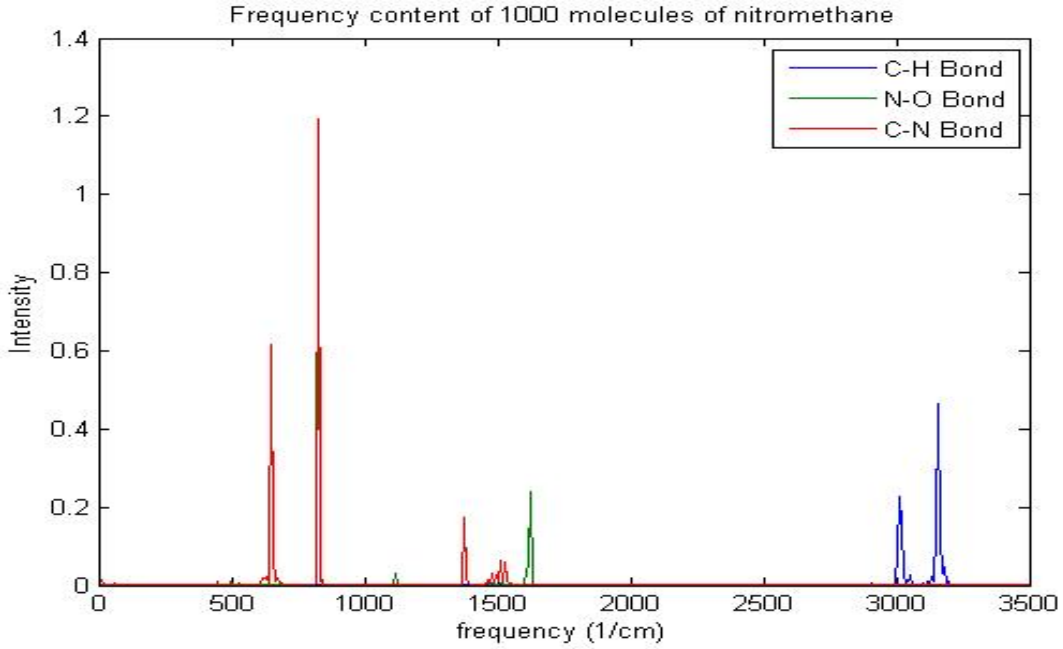

(a)

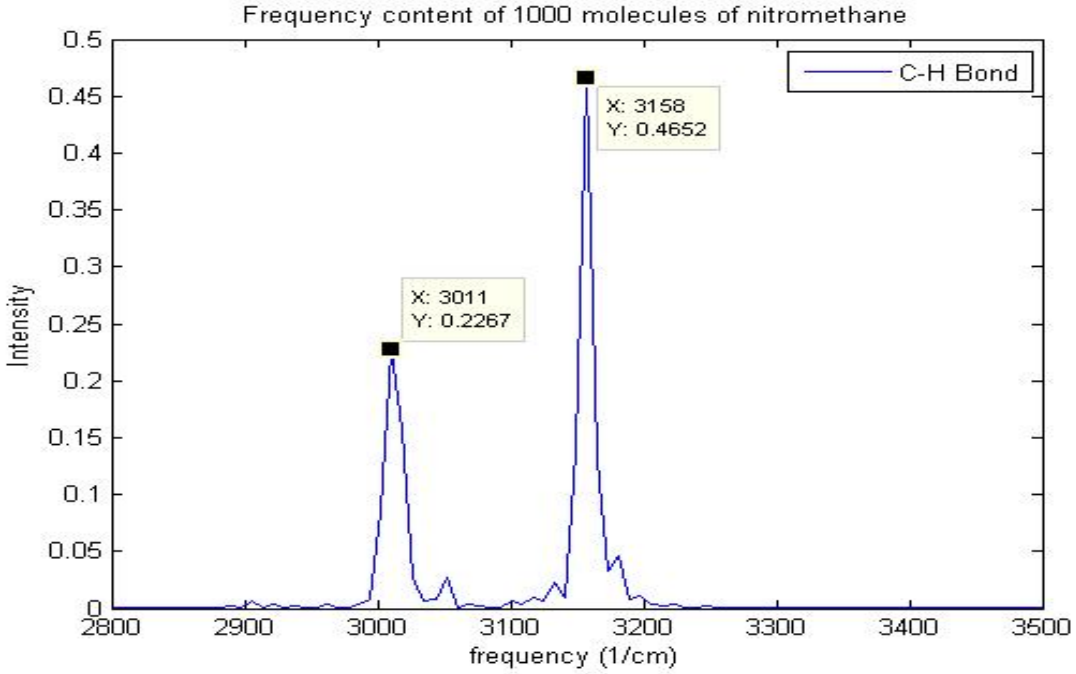

(b)

Fig. 15 Frequency spectrum of 1000 nitromethane molecules at ambient conditions (300K and 1 bar). (a) Plot showing the internal modes of CH, CN and NO bonds. (b) Frequency Spectrum of CH bond with visible symmetric and anti-symmetric stretching peaks at 3011 cm^{-1} and 3158 cm^{-1}. (c) CN bond stretching frequency (d) NO bond stretching frequency with anti-symmetric peak at 1514 cm^{-1}.

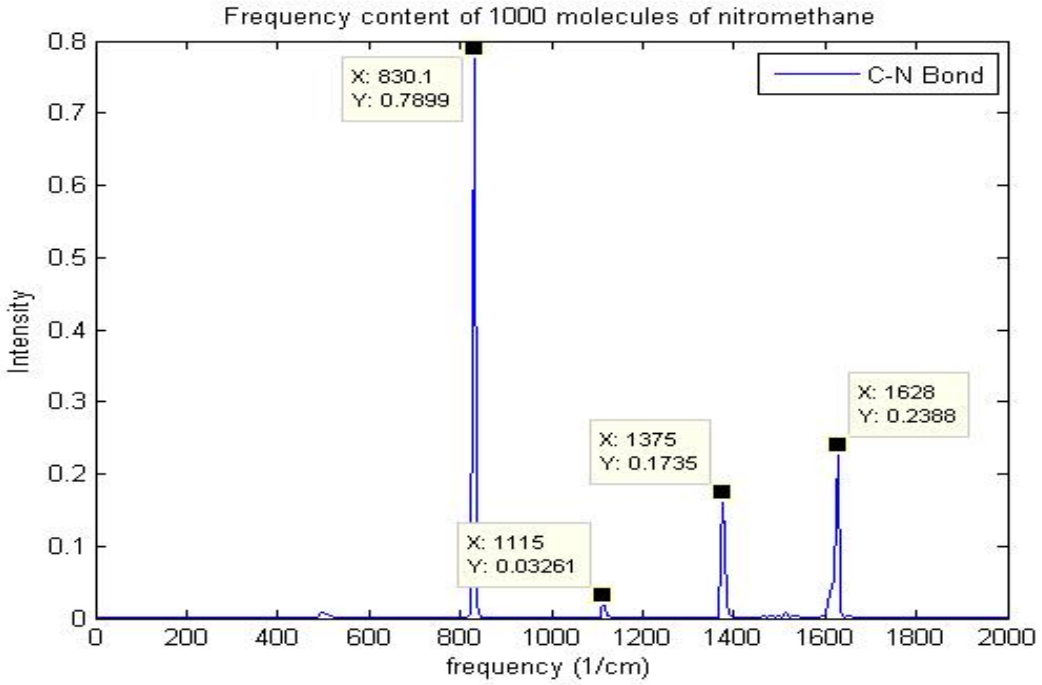

(c)

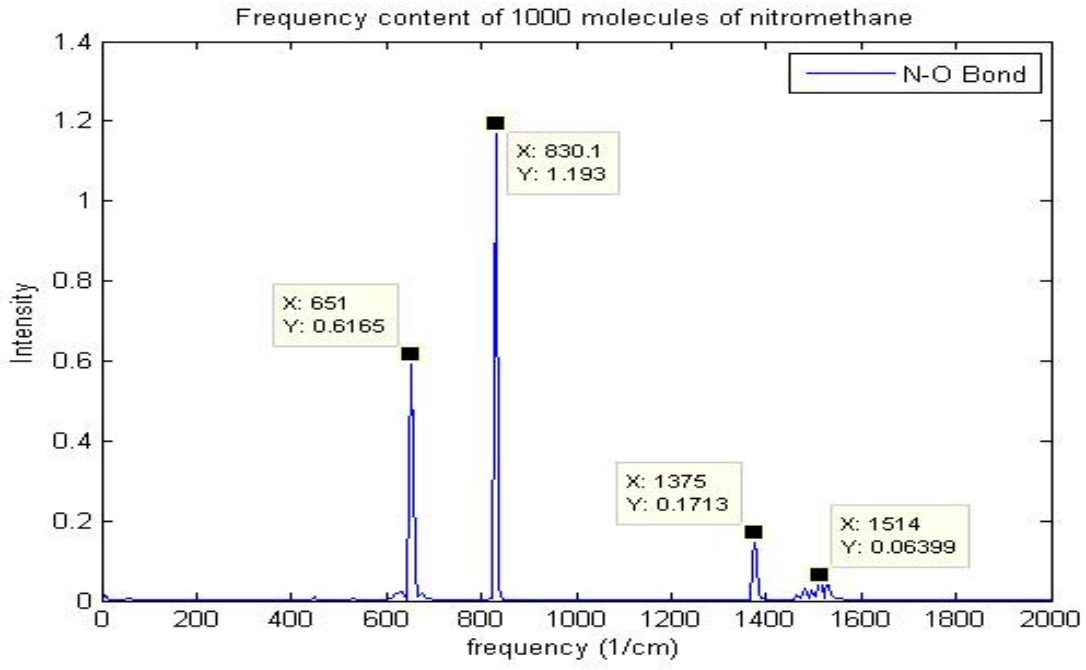

(d)

Fig. 15 continued.

4.3.3 Dissociation of nitromethane molecules

The dissociation of nitromethane molecules occurs through the scission of the CN bond. The reason being that the CN bond is the weakest with the bond energy being around 61.9 kcal/mol [60]. The thermal decomposition of nitromethane begins with the dissociation of CN bond to form CH_3 and NO_2, and it ends with the formation of a CO bond to form methyl nitrite [61]. We conduct the MD simulation of the thermal decomposition of nitromethane molecules in two stages. We first follow the decomposition till nitromethane dissociates to CH_3 and NO_2. Subsequently, we follow it till the CH_3 and NO_2 combine to form methyl nitrite.

The thermal decomposition is performed on a certain number of nitromethane molecules. After the system of nitromethane has decomposed and formed methyl nitrite molecules we conduct a frequency analysis.

4.3.3.1 Determination of Lennard Jones parameters

We begin with the analysis of 216 nitromethane molecules. As explained above, the simulation will be conducted in two stages. Stage 1 involves the decomposition of nitromethane and the stage 2 involves the formation of methyl nitrite. One of the limitations of our MD software is that it does not provide a means to incorporate the morse potential that is necessary for bond breaking (decomposition). In order to overcome this problem we propose to use the Lennard Jones potential to simulate bond breaking.

The determination of the Lennard Jones parameters(E_{min} and r_{min}) for CN bond are based on the criteria that the simulation results should provide frequency results that are in agreement with those achieved using a harmonic bond for CN. The bond dissociation energy or E_{min} was set to be 61.9 kcal/mol and r_{min} is set to be 1.47 Å.

As a trial run, we ran a box of 216 molecules using an NVT ensemble and periodic boundary conditions at 300 K. Subsequently, we ran an NVE ensemble to determine if the system had equilibrated. The coordinates file (.dcd file) from the simulation was then used for analysis. It was found that the bond lengths for CH, CN and NO were found to be 1.11 Å, 1.52 Å and 1.28 Å which are in considerable agreement to the standard equilibrium bond lengths. A frequency analysis was performed using the fft of the bond length data. Fig. 16(a) shows the frequency spectrum of the CH bond. The CH symmetric peak at 3223 cm^{-1} and the CH anti-symmetric peak at 3271 cm^{-1} are in considerable agreement with the experimental symmetric and anti-symmetric peaks of 3044 cm^{-1} and 3080 cm^{-1} respectively [62]. The CN frequency spectrum as seen from Fig. 16(b) shows at 1074 cm^{-1} which is close to the experimental frequency of 917.9 cm^{-1} [62]. The anti-symmetric NO frequency peak is observed at 1563 cm^{-1} as seen from Fig. 16(c) and the experimentally obtained frequency is around 1538.8 cm^{-1} [62]. One is also able to see the other modes of frequency in Fig. 16(b) and Fig. 16(c). The common peaks that are visible in both the figures make us conclude that a frequency spectrum for one bond carries the frequency information of other bonds as well.

In conclusion we can conjecture that the Lennard Jones parameters that we have established for the CN bond provides results that agree reasonably with the experimental

results. The next step is to use the Lennard Jones parameters to simulate the dissociation of nitromethane.

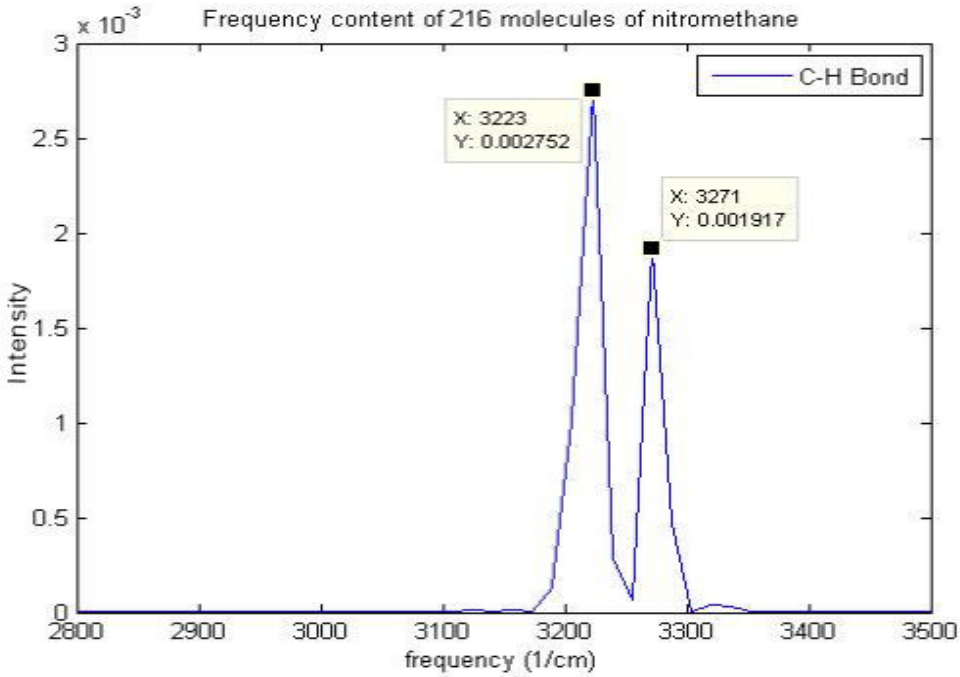

(a)

Fig. 16 Frequency distribution of 216 molecules of nitromethane at 300 K obtained using Lennard Jones parameters for the CN bond. (a) Frequency spectrum of CH bond. The symmetric and anti-symmetric peaks at 3223 cm^{-1} and 3271 cm^{-1} are clearly visible. (b) Frequency spectrum of CN bond showing a peak at 1074 cm^{-1} and also other peaks that are in common with NO bond frequency. (c) Frequency spectrum of NO bond showing an anti-symmetric peak at 1563 cm^{-1}.

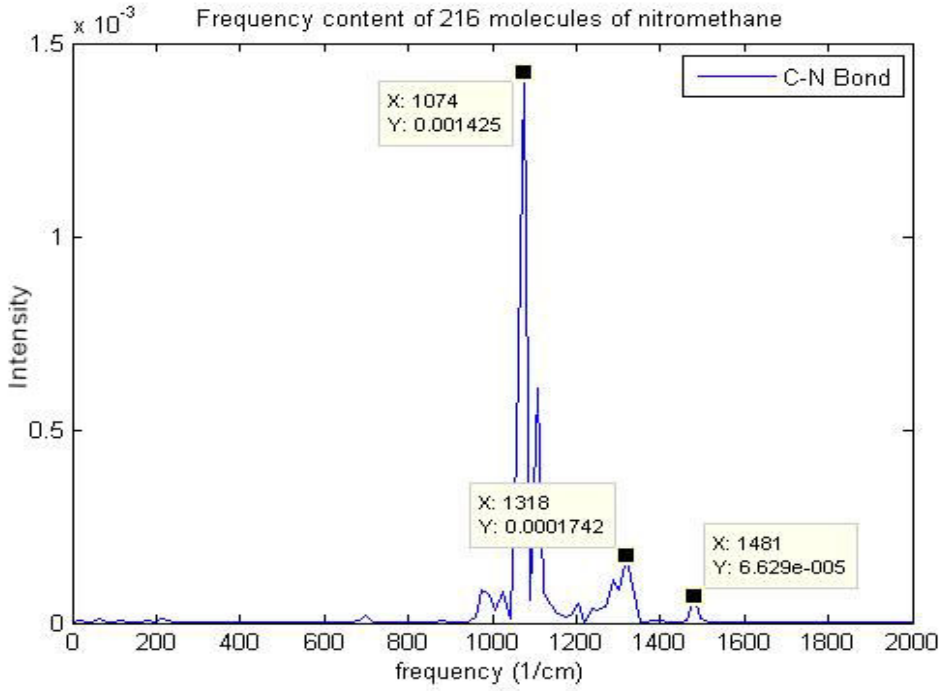

(b)

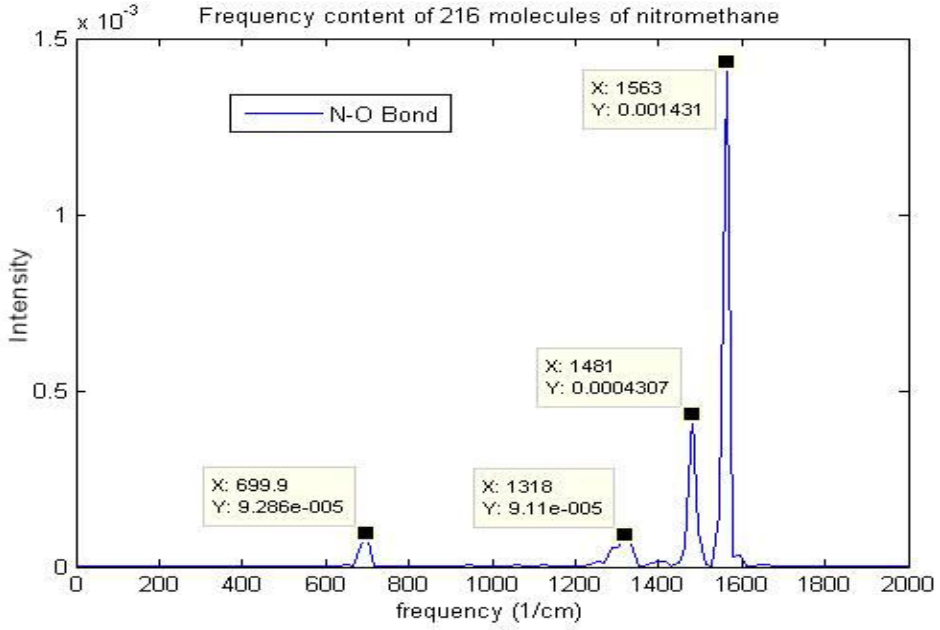

(c)

Fig. 16 continued.

4.3.3.2 MD simulation of 216 nitromethane molecules using LJ potential for C N bond

We have already established the Lennard Jones parameters for the CN bond. We build a system that is a box of 216 nitromethane molecules and conduct the pair distribution analysis to follow the dissociation. We also conduct the vibrational spectrum analysis to understand the underlying frequencies.

4.3.3.2.1 Method

For stage 1, a box of 216 nitromethane molecules is created and the force field parameters [58] are provided through the inclusion of a LJ potential between the CN bond to allow CN bond scission. The size of the box calculated by considering the molecular weight and the density was found to be 26.7874 Å. A number of variations of the LJ potential are tried to achieve the CN bond length to be around the equilibrium CN bond length. An NVT ensemble is used with periodic boundary conditions. The simulation is run from 100K to 1500K with a 50K step. At each temperature the simulation is run for 512 timesteps.

For stage 2, we use the binary coordinates, velocity and extended coordinates files to continue the simulation. However, we provide new force field parameters [63] including a LJ potential between the CO bond. Again an NVT ensemble with periodic boundary conditions is used. We equilibrate the system at 1500 K for 65536 steps.

4.3.3.2.1.1 Results

4.3.3.2.1.1.1 Pair distributions

In order to analyze the decomposition of nitromethane we need to determine the pair distributions of the atoms in the entire system. The dcd file from the stage 1 of the simulation is loaded on the Visual Molecular Dynamics software. The dcd file provides the coordinates of all atoms at every timestep of the simulation. A C program was then used to determine the pair distributions at specific timesteps. The plot of the pair distributions of stage 1 at different temperatures is shown in Fig. 17(a). The area under the each curve should be equal to N(N-1)/2 where N is the number of atoms. The area calculated from the plot and from the formula (with N = 1512) are equal (1142316). As seen from the plot we see a peak around 1.1 Å which includes the pairs of both CH and NO bonds and 1.5 Å that denoted CN pairs. We see that as the temperature increases to about 1500 K, the peak observed at 1.5 Å starts to diminish denoting CN bond breaking. However the peak at 1.1 Å starts to diminish too but starts to spread around that 1.1 Å value meaning that the CH and NO bonds are intact. Fig. 17(b) which is the pair distributions of CN pairs at different temperatures shows the evidence of CN bond breakage much better. The peak that is observed initially at 100 K starts to spread out as the temperature increases. Finally one sees the presense of large CN pair distances at temperatures greater than 1300 K denoting clearly that the CN bond has broken. Therefore at the end of Stage 1 we can conclude that nitromethane has dissociated to form CH_3 and NO_2. However, one needs to keep in mind that at this stage not all the

nitromethane molecules have dissociated, so at the end there exists a mixture of nitromethane, CH_3 and NO_2.

A similar procedure is adopted to obtain a plot of pair distributions for Stage 2. Fig. 17(c) shows a plot of the curves at specific timesteps at 1500 K. The curve at 15464 fs is the initial step for Stage 2 and denotes the dissociation of nitromethane. As the simulation proceeds we see the formation of a peak at around 1.4 Å which is the bond length of CO also evident from Fig. 17(d). Again the peak at 1.1 Å remains the same denoting that the CH, NO bonds are still intact.

The formation of methlyl nitrite has started as early as the 15564 timestep and attains it final peak distribution at 81000 fs. Therefore at the end of Stage 2, a combination of CH_3 and NO_2 has occurred resulting in the formation of methyl nitrite (CH_3ONO). In addition there might be traces of nitromethane, CH_3 and NO_2 left.

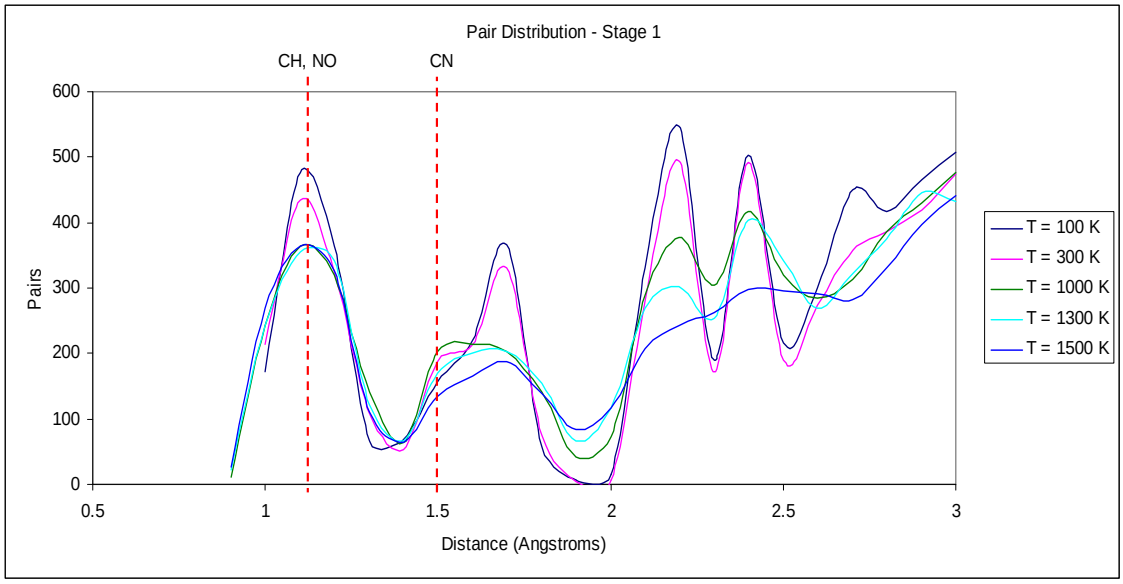

(a)

Fig. 17 Pair distributions to analyze the dissociation of 216 molecules of nitromethane (stage 1) and formation of methyl nitrite (stage 2). Stage 2 begins where Stage 1 ends i.e. from 15464 time step and the temperature is held constant at 1500 K. (a) Plot showing the pair distributions at different temperatures showing the dissociation of nitromethane molecules (Stage 1). The diminishing peak at 1.5 Å denotes CN bond breaking (b) Plot of CN pair distributions at different temperatures. The presence of large CN pair distance values beginning from 1300 K shows that the CN bond has broken. (c) Plot showing the pair distribution at different timesteps showing the formation of methly nitrite evident from the formation of CO bond at 1.4 Å. (d) Plot showing the pair distributions of CO and CN bond. The CO bond formation begins as early as the 15544 timestep and the final pair distribution at the end of stage 2 at 81000 timestep is shown where the CO bond peak is clearly defined.

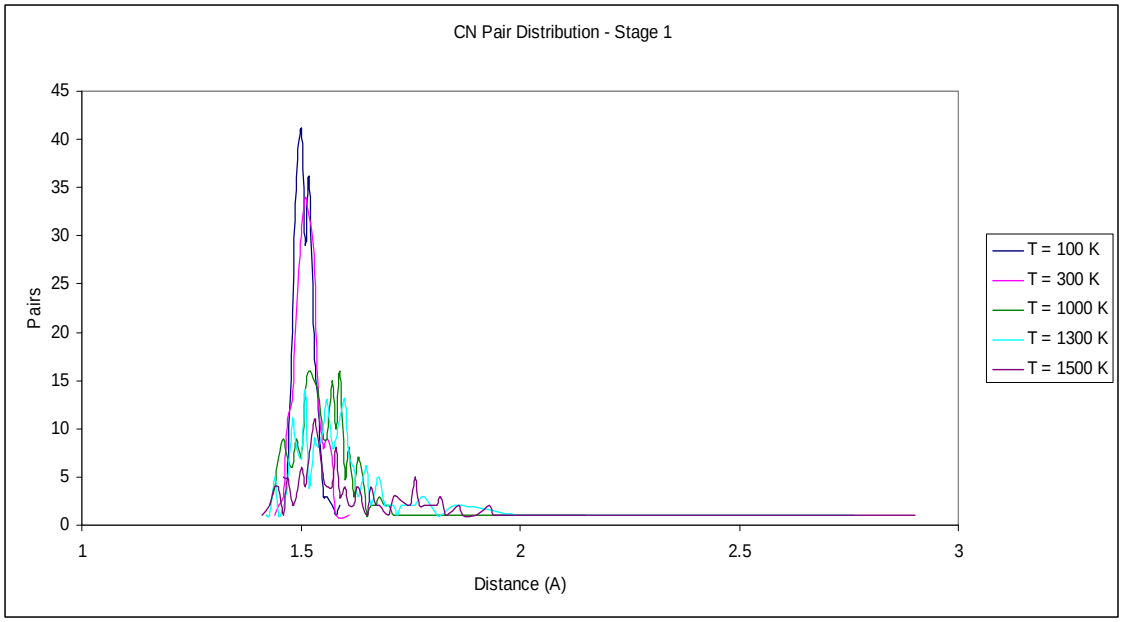

(b)

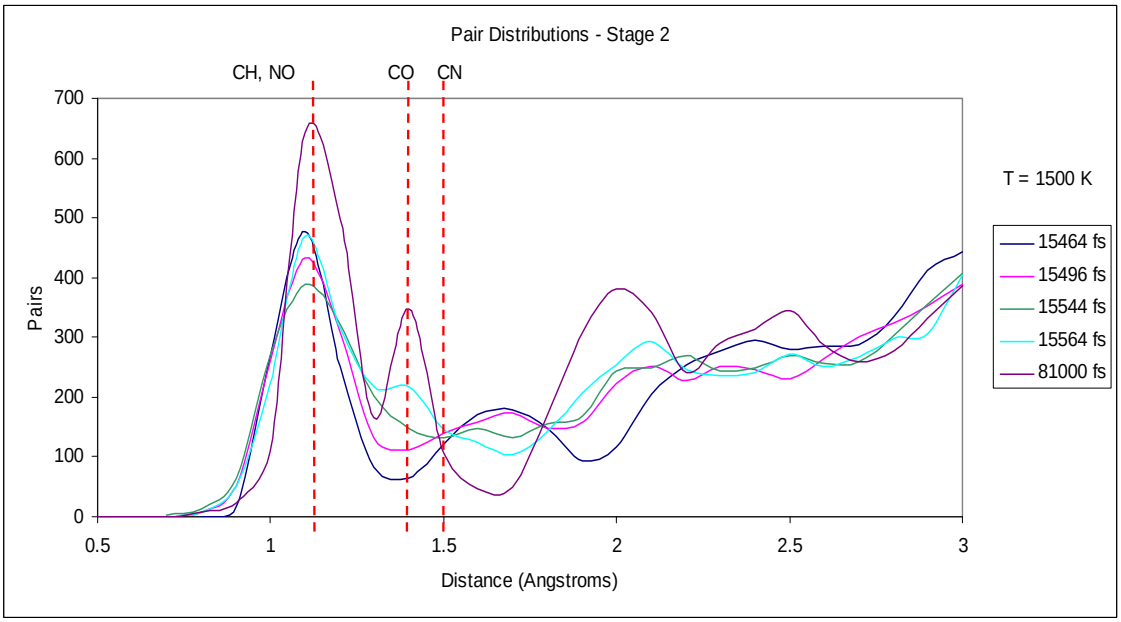

(c)

Fig. 17 continued.

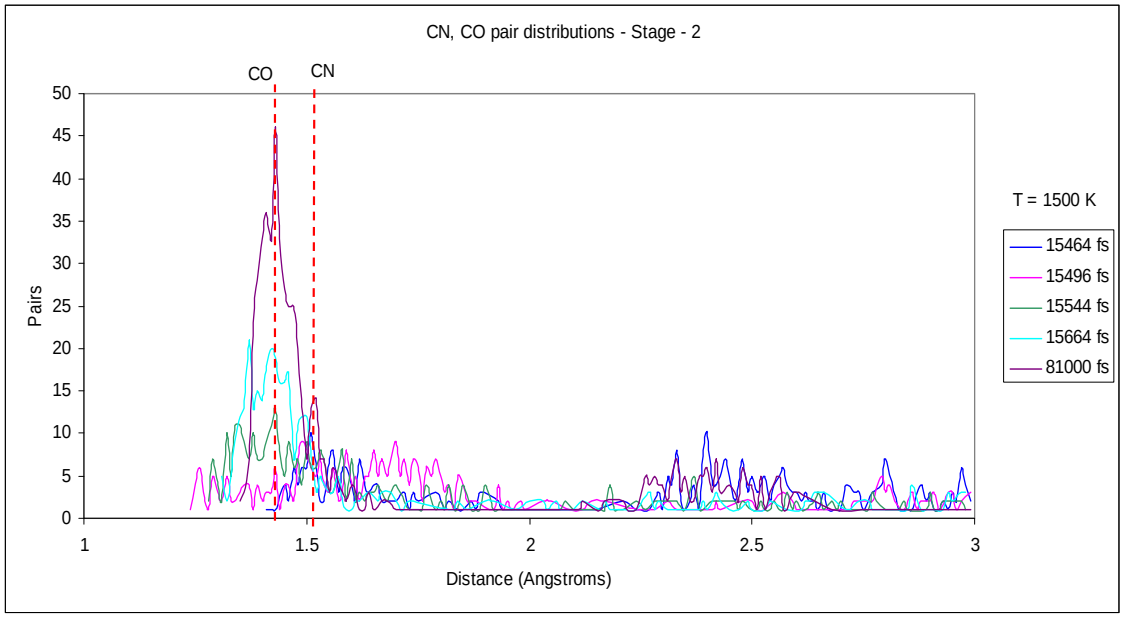

(d)

Fig. 17 continued.

4.3.3.2.1.1.2 Frequency analysis

In order to perform the frequency analysis, we ascertain whether the system has attained equilibrium by performing a simulation using NVE ensemble of the system of 216 nitromethane molecules at 1500 K with periodic boundary conditions. The resultant coordinate file is then used to perform the frequency calculation. Since the simulation is a mixture of methyl nitrite, nitromethane, CH_3 and NO_2 , we consider a single molecule of methyl nitrite for our frequency analysis.

Fig. 18(a)-(d) shows the frequency spectrum of the CH, CO, N=O and N-O bonds respectively for a chosen methyl nitrite molecule. In each case the frequency spectrum seems to be much higher than the experimental determined frequencies – CH anti-

symmetric (3040 cm-1), CH symmetric (2948 cm-1), CO (1036 cm-1), N=O (1653 cm-1), N-O (839 cm-1) [64]. This can be attributed to the fact in our case the temperature is at 1500 K unlike the experimental case which is at ambient conditions.

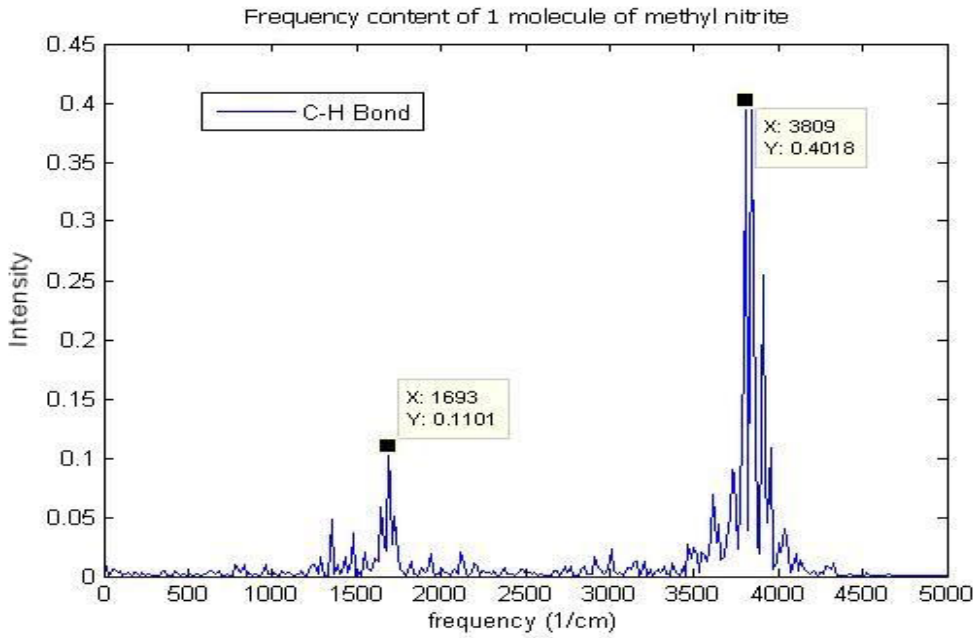

(a)

Fig. 18 Frequency content of one methyl nitrite molecule at 1500 K - 216 case. Experimentally determined frequencies at 300 K - CH anti-symmetric (3040 cm-1), CH symmetric (2948 cm-1), CO (1036 cm-1), N=O (1653 cm-1), N-O (839 cm-1) (a) CH bond frequency spectrum (b) CO bond frequency spectrum (c) N=O bond frequency spectrum (d) N-O bond frequency spectrum.

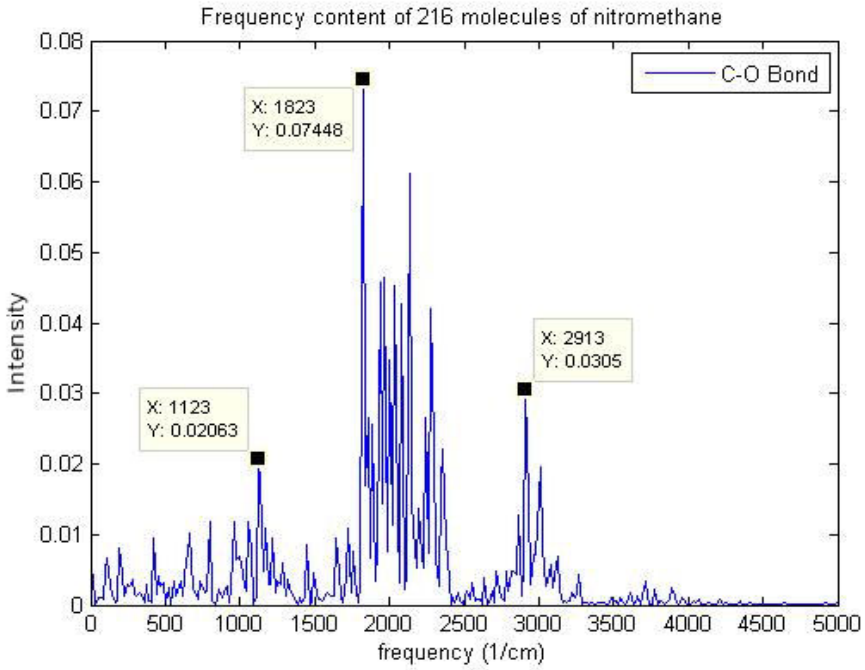

(b)

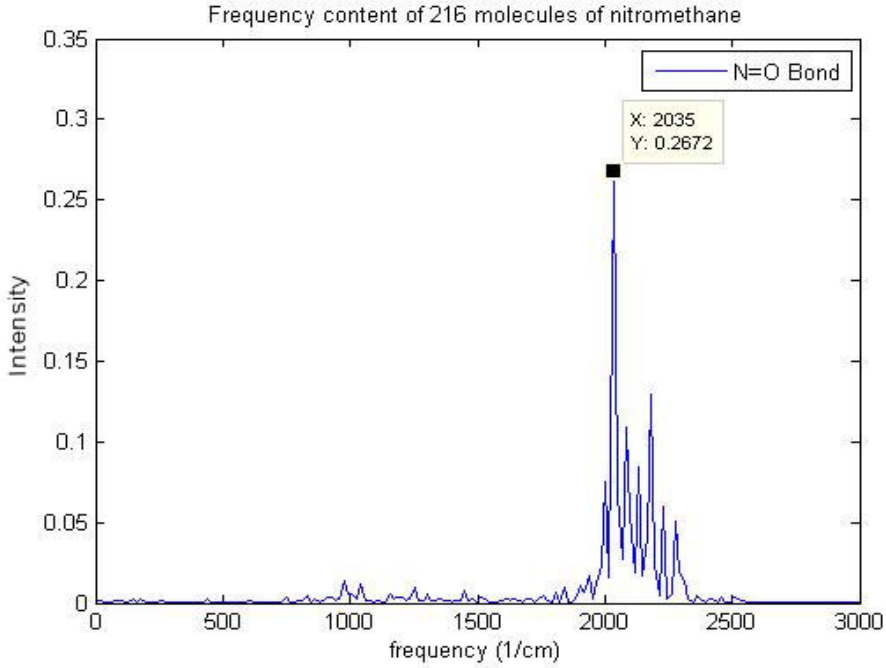

(c)

Fig. 18 continued.

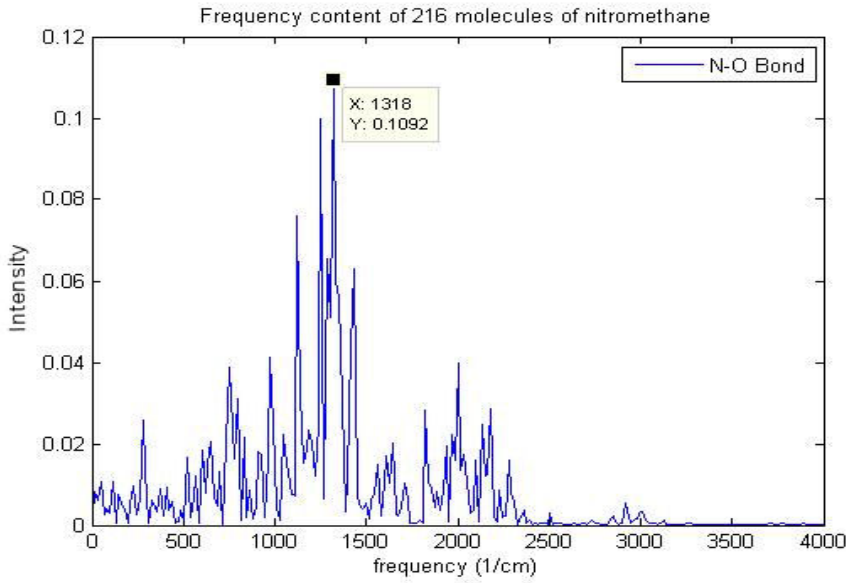

(d)

Fig. 18 continued.

Since we have achieved the frequency characteristics of nitromethane that reasonably agree with experimentally found ones, we scale our system and determine the frequency characteristics of 1000 nitromethane molecules using the same methodology.

4.3.3.3 MD simulation of 1000 nitromethane molecules using LJ potential for C N bond

4.3.3.3.1 Method

We run the simulation for 1000 nitromethane molecules in two stages as we did for the 216 molecules case using the force field parameters provided if ref. [58] and include a LJ potential between the CN bond to allow CN bond scission. The size of the box in this case calculated by considering the molecular weight and the density was found to be

44.6457 Å. A number of variations of the LJ potential are tried to achieve the CN bond length to be around the equilibrium CN bond length. An NVT ensemble is used with periodic boundary conditions. The simulation is run from 100K to 1500K with a 50K step. At each temperature the simulation is run for 2048 timesteps.

For stage 2, we use the binary coordinates, velocity and extended coordinates files to continue the simulation. However, we provide new force field parameters [63] including a LJ potential between the CO bond. Again an NVT ensemble with periodic boundary conditions is used. We equilibrate the system at 1500 K for 131072 timesteps.

4.3.3.3.2 Results

4.3.3.3.2.1 Pair distributions

As in the case of 216 nitromethane molecules we begin with the determination and analysis of pair distributions of the atoms. The dcd file is read using a c program to determine the pair distributions at specific timesteps. The plot of the pair distributions of stage 1 at different temperatures is shown in Fig. 19(a). We see that as the temperature increases to about 1500 K, the peak observed at 1.5 Å starts to diminish denoting CN bond breaking. However the peak at 1.1 Å starts to diminish too but starts to spread around that 1.1 Å value meaning that the CH and NO bonds are intact. Fig. 19(b) is a plot of the pair distributions of the CN pairs at different temperature and it gives a much better idea as to the nature of dissociation through CN bond breakage. The peak that is observed initially at 100 K starts to spread out as the temperature increases. Finally one

sees the presense of large CN pair distances at temperatures greater than 1300 K denoting clearly that the CN bond has broken. Therefore at the end of Stage 1 we can conclude that nitromethane has dissociated to form CH_3 and NO_2. However, one needs to keep in mind that at this stage not all the nitromethane molecules have dissociated, so at the end there exists a mixture of nitromethane, CH_3 and NO_2. Comparing the corresponding plots of Pair distributions (Fig. 19(a) and Fig. 17(a)) and CN pair distributions (Fig. 19(b) and Fig. 17(b)) of Stage 1 of 1000 and 216 nitromethane molecules dissociations, we see that the plots showing a qualitative similarity. Quantitatively though there seems to be a scaling factor involved between the two plots.

Upon the pair distributions analysis of stage 2 of the decomposition we see striking similarities again with that of the 216 molecules case. As prior explained, the curves at 62272 fs in Fig. 19(c) and Fig 19(d) denote the end point of stage 1 where the dissociation of nitromethane has begun. As evident from the plots we see that as the stage 2 simulation proceeds there is a formation of the CO bond visible from the formation of a peak around 1.4 Å. This suggests a formation of methyl nitrite. Finally at the end of stage 2 at 163336 fs there a combination of some CH_3 and NO_2 species has occurred to form methyl nitrite, in addition to residual traces of nitromethane, CH_3 and NO_2. Once again the when the corresponding plots (Fig. 19(c) and Fig. 17(c), Fig. 19(d) and Fig. 17(d)) of Stage 2 of 1000 and 216 nitromethane molecules decomposition are compared we see evidence of qualitative similarity and quantitative scaling.

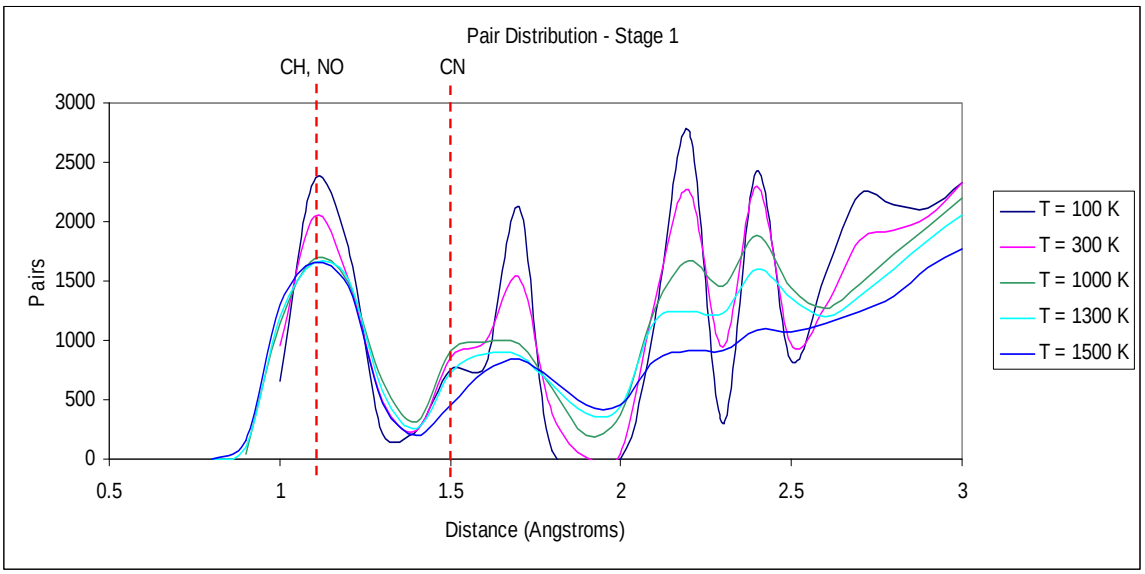

(a)

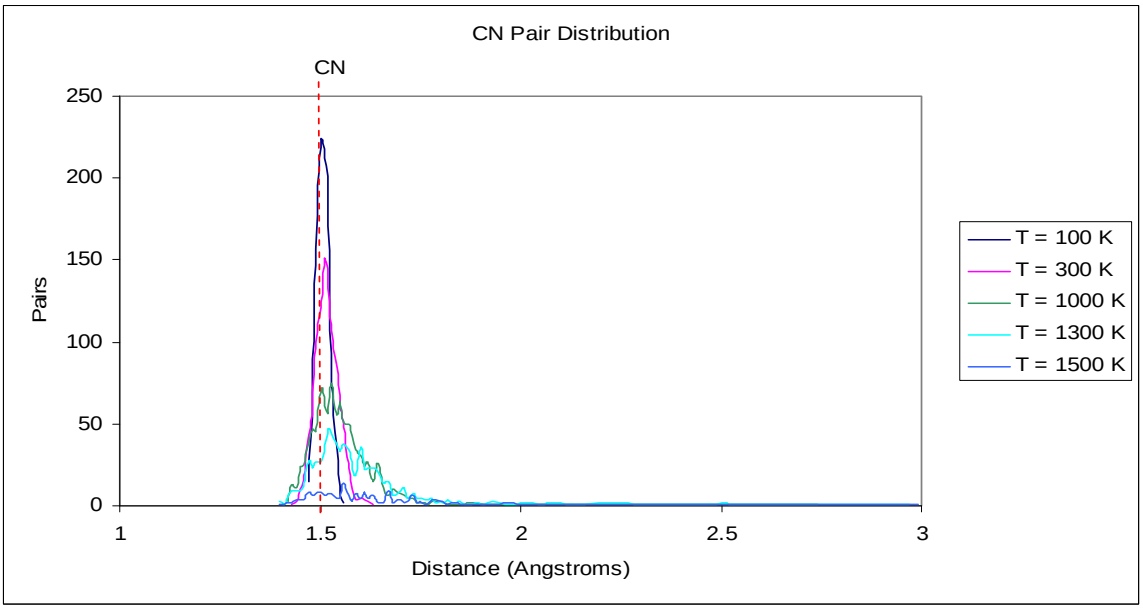

(b)

Fig. 19 Pair distributions of the dissociation of 1000 molecules of nitromethane (stage 1) and formation of methyl nitrite (stage 2). Stage 2 begins where Stage 1 ends i.e. from the 62272 fs time step temperature held constant at 1500 K. (a) Plot showing the pair distributions at different temperatures showing the dissociation of nitromethane molecules (Stage 1). The diminishing peak at 1.5 Å denotes CN bond breaking (b) Plot of CN pair distributions at different temperatures. The presence of large CN pair distance values beginning from 1300 K shows that the CN bond has broken. (c) Plot showing the pair distribution at different timesteps showing the formation of methly nitrite evident from the formation of CO bond at

1.4 Å. (d) Plot showing the pair distributions of CO and CN bond. The CO bond formation is evident from the rising peak at 1.4 Å as the simulation proceeds.

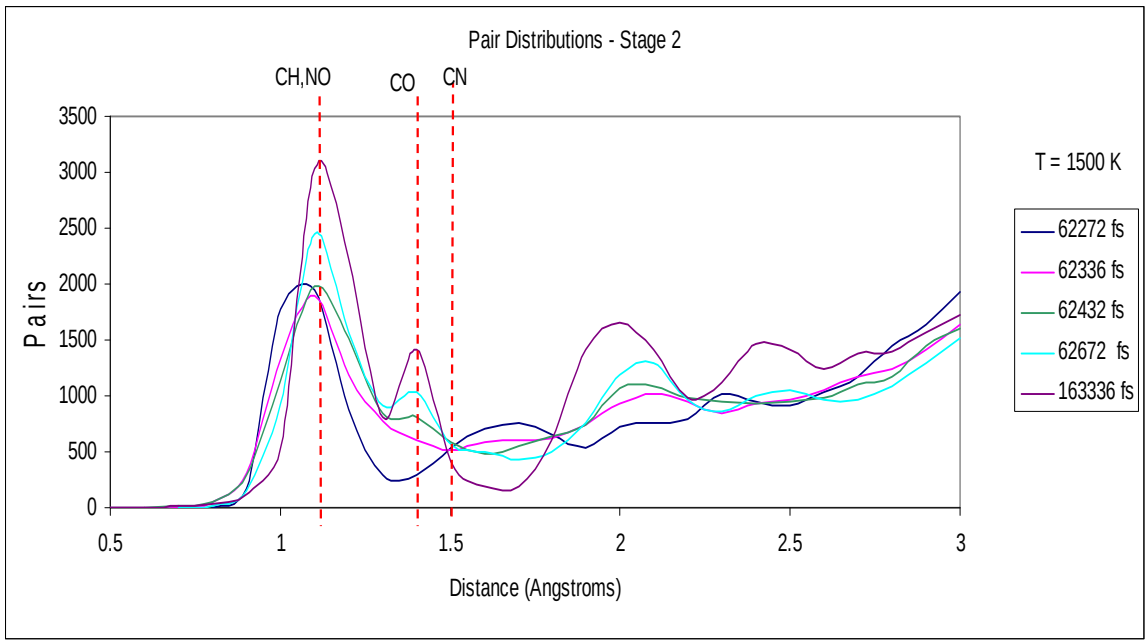

(c)

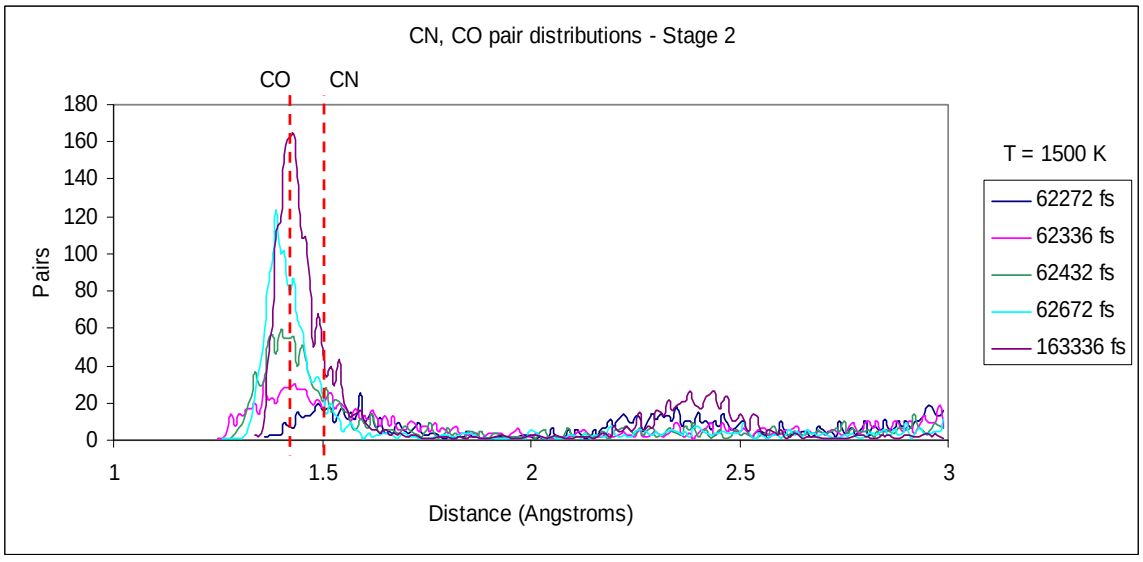

(d)

Fig. 19 continued.

4.3.3.3.2.2 Frequency analysis

We now undertake the frequency analysis of the 1000 nitromethane molecule system. At the end of stage 2 we run a NVE ensemble at 1500 K with periodic boundary conditions in order to determine the stability of the system. The resultant coordinate file is then used to perform the frequency calculation. Our simulation is a mixture of methyl nitrite, nitromethane, CH_3 and NO_2 however we are considered only about methyl nitrite frequency analysis. Hence we chose a single molecule of methyl nitrite for our frequency analysis.

Fig. 20(a)-(d) shows the frequency spectrum of the CH, CO, N=O and N-O bonds respectively for a chosen methyl nitrite molecule. In each case the frequency spectrum seems to be much higher than the experimental determined frequencies – CH anti-symmetric (3040 cm-1), CH symmetric (2948 cm-1), CO (1036 cm-1), N=O (1653 cm-1), N-O (839 cm-1) [64]. This can be attributed to the fact in our case the temperature is at 1500 K unlike the experimental case which is at ambient conditions.

A comparison of the plots with 216 molecule case reveals the inherent similarity between the frequency spectrum characteristics of the CH (Fig. 18(a) and Fig. 20(a)), CO (Fig. 18(b) and Fig. 20(b)) and N=O (Fig. 18(c) and Fig. 20(c)) bond. However there seems to be a considerable difference in the frequency spectrums for the N-O bond as seen from Fig. 18(d) and Fig. 20(d).

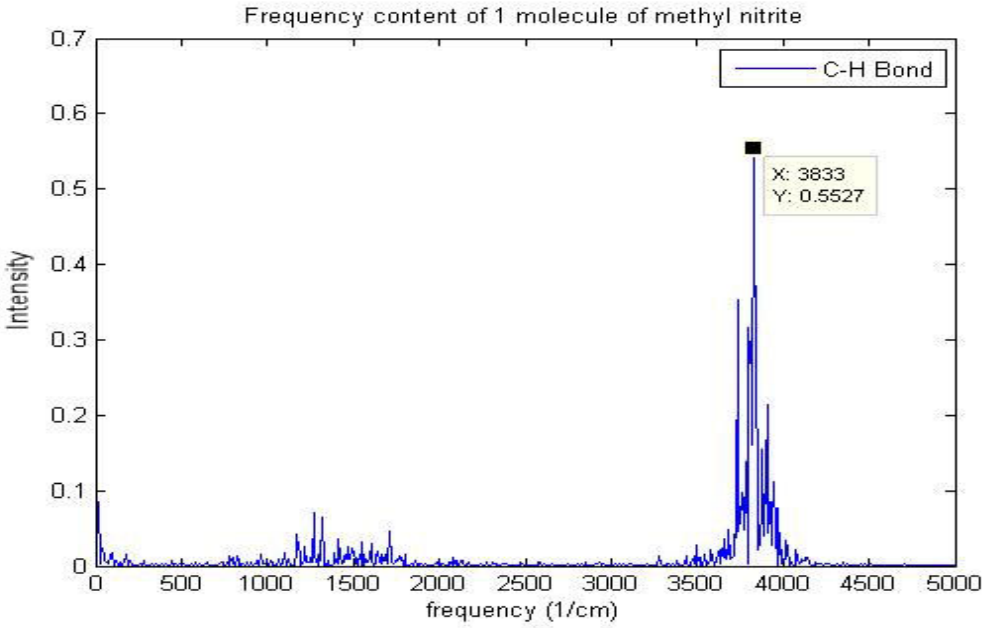

(a)

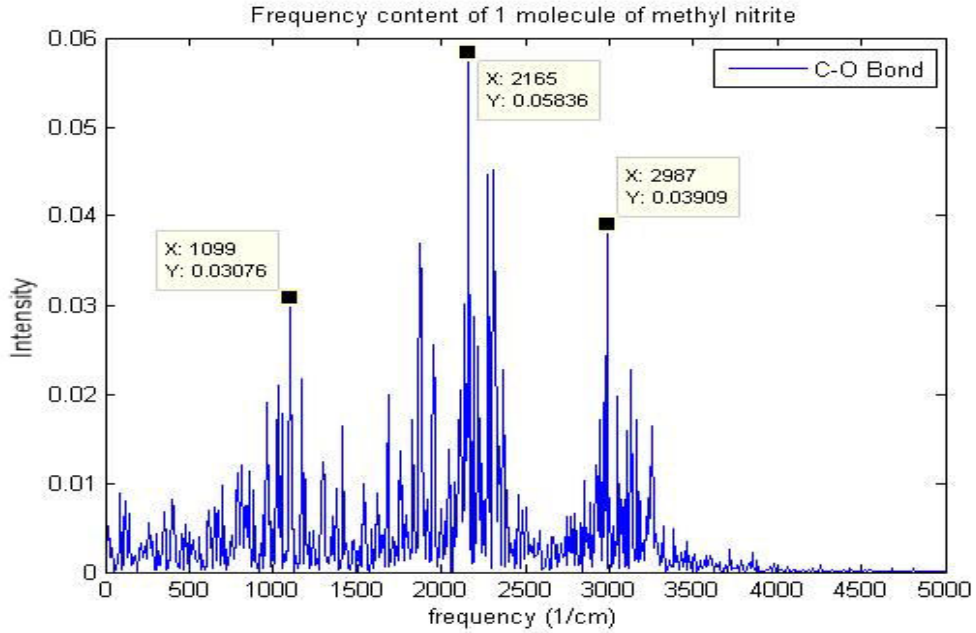

(b)

Fig. 20 Frequency content of one methyl nitrite molecule at 1500 K - 1000 case. Experimentally determined frequencies at 300 K - CH anti-symmetric (3040 cm-1), CH symmetric (2948 cm-1), CO (1036 cm-1), N=O (1653 cm-1), N-O (839 cm-1) (a) CH bond frequency spectrum (b) CO bond frequency spectrum (c) N=O bond frequency spectrum (d) N-O bond frequency spectrum.

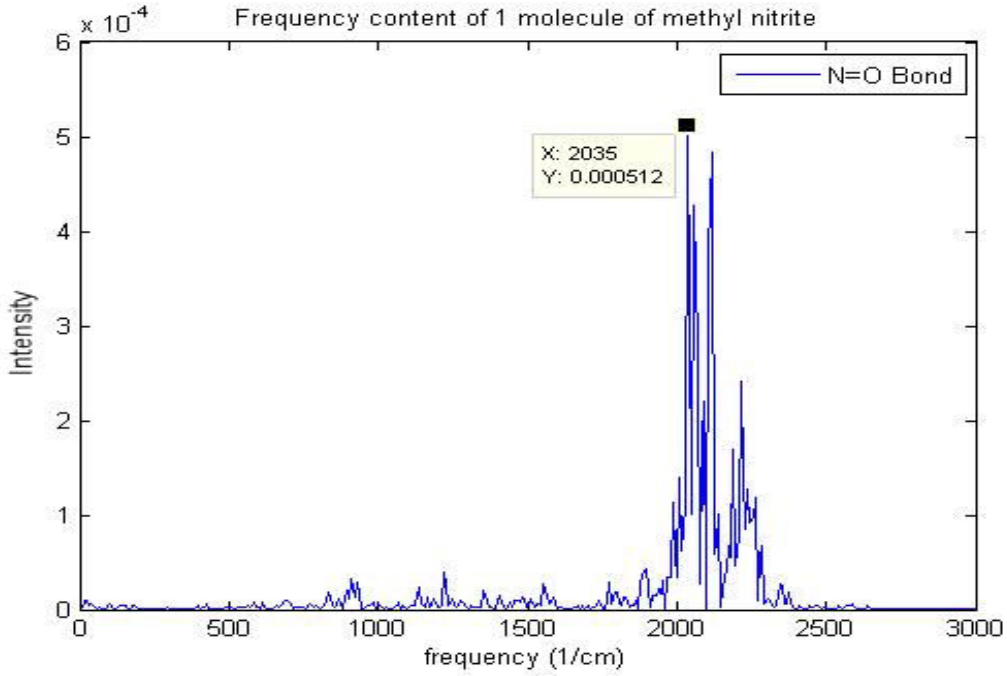

(c)

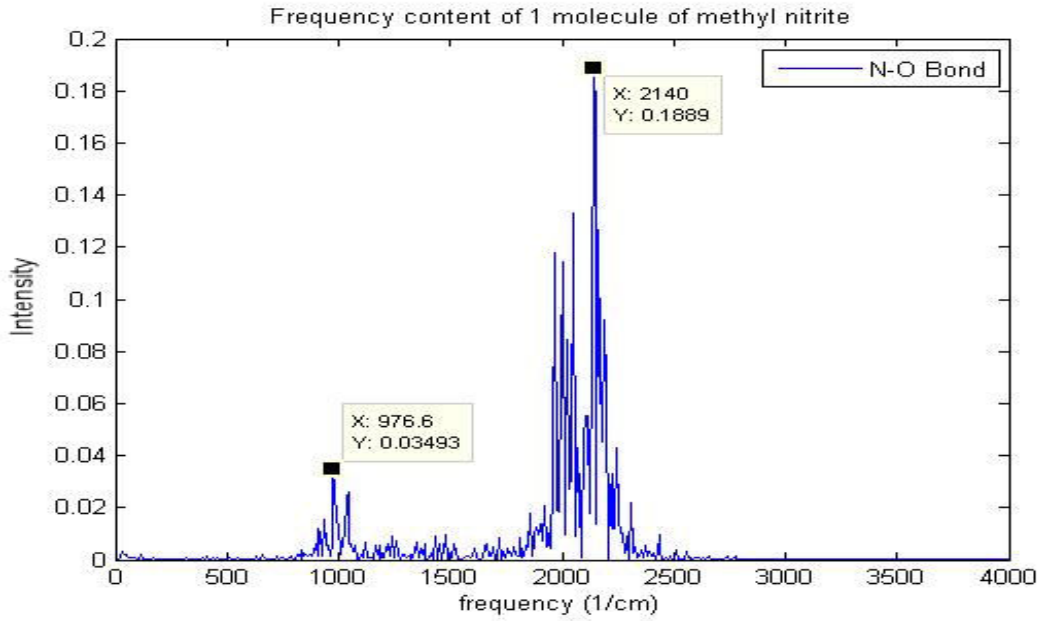

(d)

Fig. 20 continued.

4.4 Nanosensor architecture

The architecture of the nanosensor is as shown in Fig. 21. The sensing part of the nanosensor consists of the gold layer covered with glass with a small gap provided between the two layers. Nitromethane will enter this gap and interact with the gold layer. S1 is a terahertz source and D is a terahertz detector. We believe that nitromethane will cause sufficient changes in the lattice dynamics of the gold layer. Gold has frequencies in the terahertz region and the presence of nitromethane will cause measurable changes in these terahertz frequencies that can be detected thus providing a means to sense nitromethane. We would like to mention here that we are considered with providing the proof of concept only and we have not performed any analysis on the choice of material for our nanosensor.

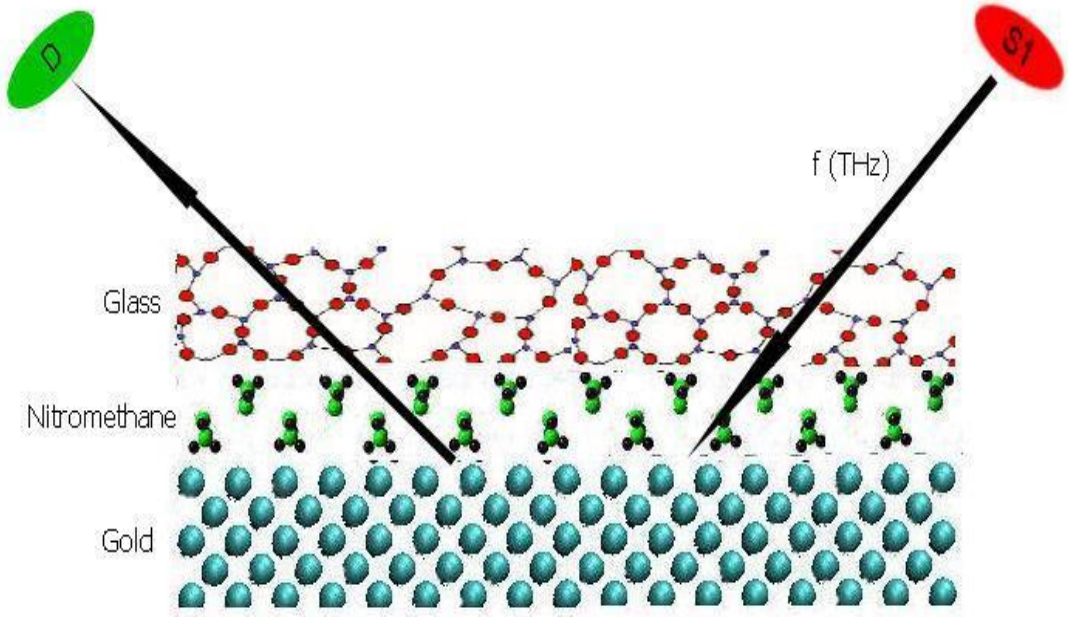

Fig. 21 Nanosensor architecture. Nanosensor consists of gold and glass layer with a small gap where the nitromethane interacts with gold. S1 is a terahertz source and D is a terahertz detector.

4.5 M.D test bed for 216 nitromethane molecules

We first analyze the frequency characteristics of bulk gold, gold without nitromethane (gap filled with water) and finally gold with nitromethane. For the test bed we can consider three types of scenarios – gold glass interaction, gold water glass interaction and gold nitromethane glass interaction.

4.5.1 Gold glass interaction

For this interaction we build a box of gold and build another box of glass at a certain distance on top of the gold.

4.5.1.1 Design of gold box

As mentioned earlier gold electrodes form an integral part of our nanosensor sensing mechanism. Gold being a noble metal has characteristics that make it a good candidate for nanotechnological applications. It is resistant to surface oxidation which would not be the case when we use other metals. It has optical properties depending on the size varying from red to purple that can be used for a wide range of applications. They have a surface chemistry that is well suited for bottom-up assembly of structures especially through the attachment of sulphur-containing molecules. In addition to these factors gold has advantages like ease of fabrication, and good electrical and thermal conductivity. Needless to say that Gold is extremely important to the field of nanotechnology.

Gold has a face centered cubic crystal structure. We build a gold box with (111) orientation. This is to ensure that maximum number of gold atoms are exposed to the

analyte. Fig. 22 shows the unit cell of gold with the important parameters that need to be considered and their relations. The unit cell axis dimension is around 4.078 Å with the nearest neighbour being at a distance of 2.883581 Å. Thus we can build a gold f.c.c crystal with (111) orientation. We build a gold cube that has a side of 26.787439 Å. If you note this was the side length of the cube for the 216 nitromethane molecules. In Fig. 22 the atoms are shared by the surrounding unit cells. So we have 8(1/8) + 6(1/2) = 4 atoms per unit cell. Schematically the unit cell shown in Fig. 22 can now be represented as shown in Fig. 23. For a given cube side length of 26.787439 Å, we see that na unit cells (as shown in Fig. 23) can be fit into the side. For a unit cell axis dimension (a) equal to 4.078 Å, we can fit 7 unit cells. Therefore as show in Fig. 24, we can fit 7 unit cells along each axis. Hence the total number of gold atoms is 4*7*7*7 = 1372 atoms.

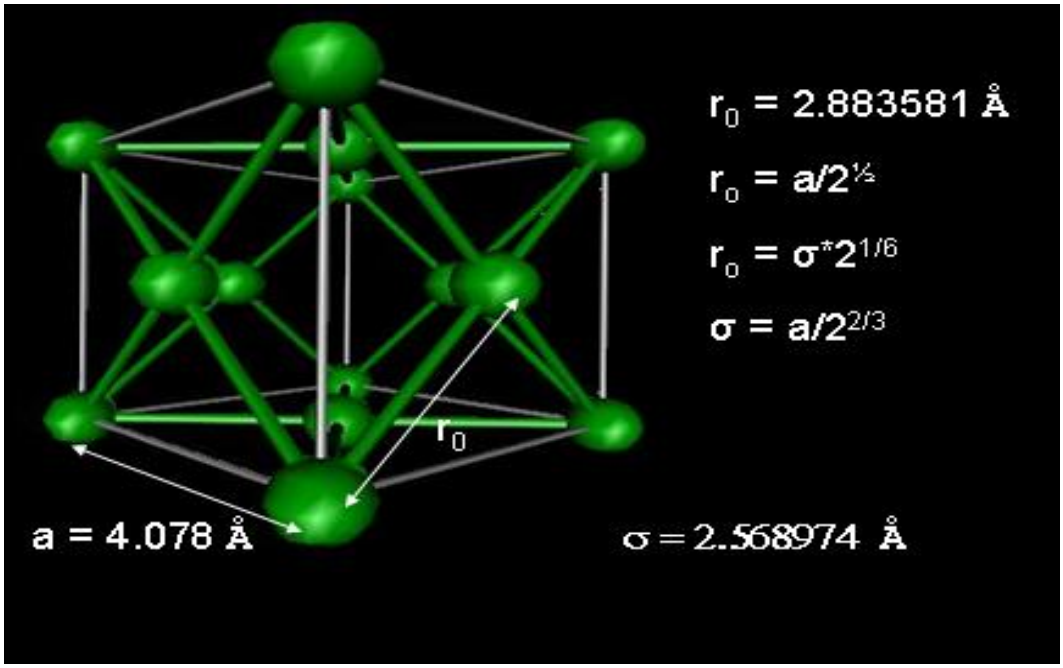

Fig. 22 Unit cell of gold f.c.c crystal. a is the unit cell axis dimension, r_o is the distance at which the Lennard Jones potential is minimum. σ, distance between the atoms at which the Lennard Jones potential is zero. Gold atoms are governed by non bonded interactions and the bonds here are show only for ease of explanation.

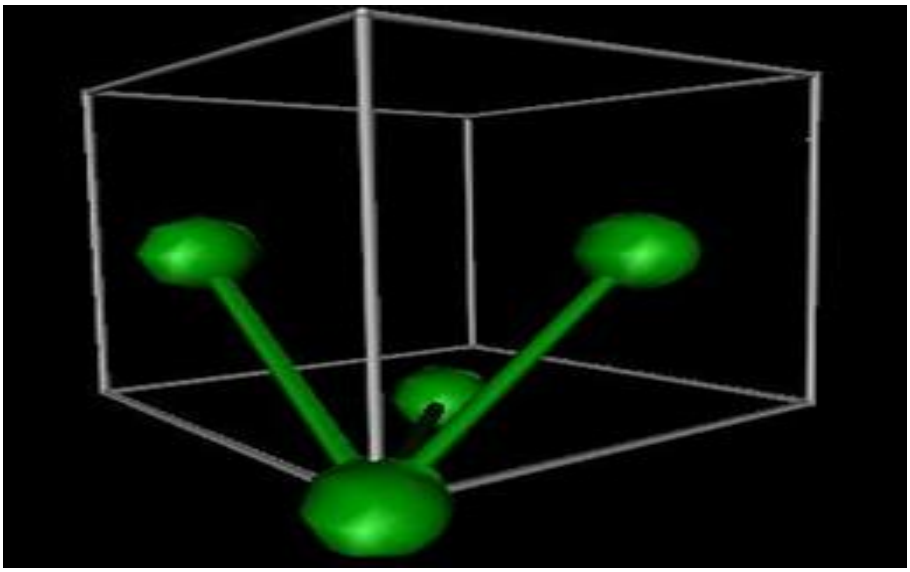

Fig. 23 Another representation of a unit cell of gold f.c.c crystal. It shows the 4 whole atoms that a unit cell can be considered to be consisting of instead of the shared atoms shown in Fig. 22.

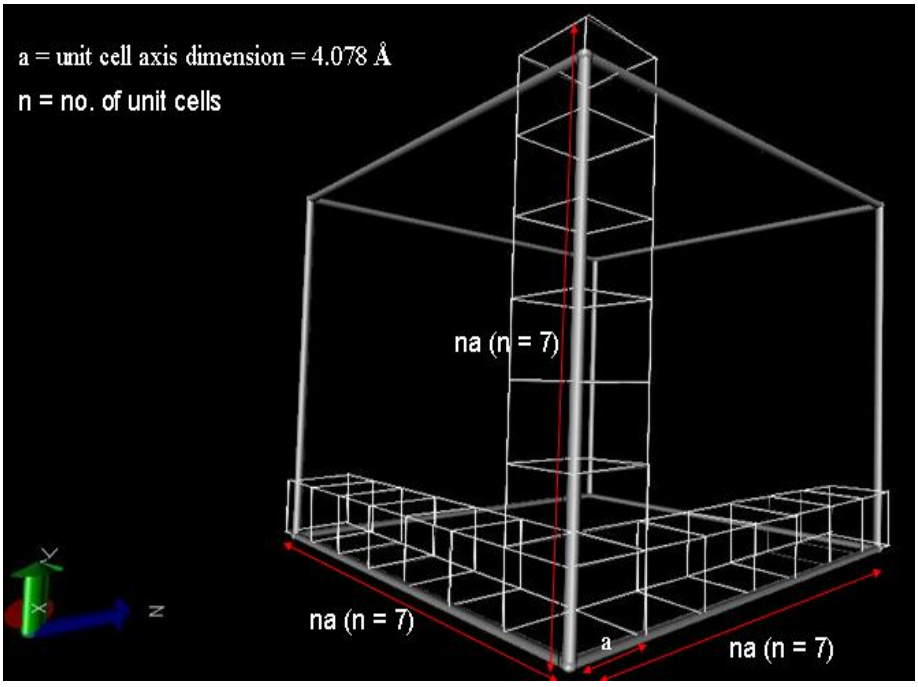

Fig. 24 Gold box dimensions – 216 case. For a cube of side 26.787437 Å and unit cell axis dimension (a) of 4.078 Å, we can fit 7 unit cells along each axis. The total number of gold atoms in the cube is 4*7*7*7 = 1372 atoms.

4.5.1.2 Lennard Jones parameters for gold

Though in Fig. 22 and Fig. 23, we have shown that the gold atoms are bonded, this is just a schematic representation. The gold atoms are non bonded and are governed by the Lennard Jones potential. As seen from Fig. 22, r_o i.e. the distance at which the Lennard Jones potential is minimum is 2.883581 Å. σ, distance between the atoms at which the Lennard Jones potential is zero is 2.568974 Å. The observed dissociation energy of Au-Au is 52 kcal/mol [65]. We need to now scale the dissociation energy carefully since in our case each gold atom is interacting with a number of other gold atoms.

Dissociation energy of Au-Au, E_d = 52 kcal/mol

Depth of Lennard Jones potential well, $\varepsilon = N * (E_d/N_b)$

Where N is the number of gold atoms, N_b is the number of bonds = N (N-1)/2.

For N = 1372 atoms, the number of bonds between nearest neighbours i.e. at a distance of 2.883581 Å is 7098 providing a factor of N/ N_b of 5.2. As N approaches infinity, this factor approaches 6.

Hence $\varepsilon = E_d /6 = 52/6 = 8.666667$ kcal/mol.

Table 3 shows the Lennard Jones parameters for gold is $\varepsilon = 8.666667$ kcal/mol and r_o = 2.883581 Å.

Table 3. Lennard Jones parameters for gold.

Atom	r_o (Å)	ε (kcal/mol)
Au	2.883581	8.666667

4.5.1.3 Design of glass box

Glass consists of 70% amorphous silicon dioxide. So we proceed to design a box that contains amorphous silicon dioxide molecules. The box needs to hold 216 silicon dioxide molecules with the density being 2.6 gm/c.c and the molecular weight being 60.1 gm/mol. The volume of box was calculated to be 8290.942912 $Å^3$. Since the box has to sit on top of the gold box, the dimensions of the silicon dioxide box are 26.787439 Å X 26.787439 Å X 11.554244 Å.

The silicon dioxide box we have designed is to be inert. The silicon dioxide molecules are rigid and do not interact with the gold atoms. To ensure this we set the

beta-factor column of the pdb file to 1 (0 being flexible, 1 being rigid). In addition we set the simulation configuration file to only calculate the interactions pertaining to gold atoms and not the silicon dioxide molecules. Table 4 shows the force field parameters for silicon dioxide. Though the simularion does not consider these parameters, NAMD still requires that we provide the force field parameters. The force field parameters pertain to the CHARMM force field.

Table 4. Force field parameters for silicon dioxide.

Atom	Charge
SI	0.720000
O	-0.360000
O	-0.360000

Bond	k_b (kcal/mol/Å^2)	b_0 (Å)
SI-O	200.000000	1.620800

Angle	k_θ (kcal/mol/rad^2)	θ_0 (rad)
O-SI-O	40.000000	139.000000

Atom	r_o (Å)	ε (kcal/mol)
SI	0.000000	0.000000
O	-0.040000	1.700000

4.5.2 Gold water glass interaction

We have already designed the boxes for gold and glass, we now build a box of water between the boxes of gold and glass.

4.5.2.1 Design of water box

The design of the glass box follows the same design principles as that of the glass box. We begin with the initial information that we need to build a water box containing 512 molecules. Therefore for water density 1 gm/c.c and molecular weight 18.0154 gm/mol, the volume of box comes to be 15316.534114 $Å^3$. The dimensions of the water box are 26.787439 Å X 26.787439 Å X 21.345096 Å. The force field parameters pertain to the TIP4 force field and are shown in Table 5.

Table 5. Force field parameters for water (correspond to the TIP4 force field).

Atom	Charge
O	-0.834000
H	0.417000
H	0.417000

Bond	k_b (kcal/mol/$Å^2$)	b_0 (Å)
O-H	450.000000	0.957200

Angle	k_θ (kcal/mol/rad^2)	θ_0 (rad)
H-O-H	55.000000	104.520000

Atom	r_o (Å)	ε (kcal/mol)
O	3.536400	-0.152100
H	0.449000	-0.046000

4.5.3 Gold nitromethane glass interaction

This is the third type of system we need to simulate. We add a box of nitromethane between the gold and glass boxes.

4.5.3.1 Design of nitromethane box

The design of the nitromethane box follows the same design principles as that of the glass box. We begin with the initial information that we need to build a nitromethane box containing 216 molecules. Therefore for nitromethane density of 1.139 gm/c.c and molecular weight 61.04 gm/mol, the volume of box comes to be 19221.779246 $Å^3$. The dimensions of the water box are 26.787439 Å X 26.787439 Å X 26.787439 Å. The force field parameters for nitromethane have already been established in the previous sections. It is important to reiterate here that the interaction between the carbon and nitrogen atoms of nitromethane are modeled using the Lennard Jones potential. Table 6 provides the force field parameters for nitromethane taken from ref. [58].

Table 6. Force field parameters for nitromethane.

Atom	Charge
C	-0.120000
H	0.040000
H	0.040000
H	0.040000
N	0.300000
O	-0.150000
O	-0.150000

Bond	k_b (kcal/mol/Å^2)	b_0 (Å)
C-H	365.072000	1.090000
N-O_1	564.215000	1.226700
N-O_2	564.215000	1.226700

Angle	k_θ (kcal/mol/rad^2)	θ_0 (rad)
C-N-O_1	70.345000	117.039900
C-N-O_2	70.345000	117.039900
N-C-H	53.696000	107.560700
O_1-N-O_2	157.124000	125.890000
H-C-H	35.813500	111.312300

Dihedral	k_ψ (kcal/mol)	N	δ
H-C-N-O_1	0.27	3	90.000000
H-C-N-O_2	0.27	3	-90.000000

Atom	r_o (Å)	ε (kcal/mol)
C	4.120000	-0.080000
O_1	2.400000	-0.120000
O_2	2.400000	-0.120000
N	3.300000	-0.200000
H	2.640000	-0.022000
C-N*	1.470000	-61.90000

* - This parameter fixes the Lennard Jones parameter for the C N interaction. It is incorporated to allow dissociation to be part of the simulation.

4.5.4 MD simulations

For the three types of scenarios as shown in Fig. 25(a)-(c) we perform an isochoric, isothermal molecular dynamics simulations using the NAMD program (NVT ensemble). Periodic boundary conditions are used and constant temperature of 300 K is achieved via langevin dynamics. The langevin damping coefficient is chosen to be 5 /ps which we believe is sufficient for such a system. The equations of motion are integrated using the Verlet leapfrog procedure with a timestep of 1 fs. The cutoff distance chosen was 12 Å and the long range electrostatic interactions were calculated using particle mesh ewald sum method which is especially effective when periodic boundary conditions are present. In the case of the gold glass interaction, the NVT ensemble was run for 131072 fs. Subsequently a NVE ensemble was run for 65536 fs to ascertain system equilibration and to gather the frequency analysis data. In the case of gold water glass interaction, the NVT ensemble was run for 262144 fs followed by a NVE ensemble for 65536 fs. Similarly for the gold nitromethane glass interaction, the NVT ensemble was run for 524288 fs followed for a 65536 fs NVE ensemble run. The force field parameters have already been established and the CHARM22 potential energy function is used model the three interactions. It is important to note that in all these simulations the silicon dioxide molecules are held fixed and their forces are not considered in our calculations and analysis.

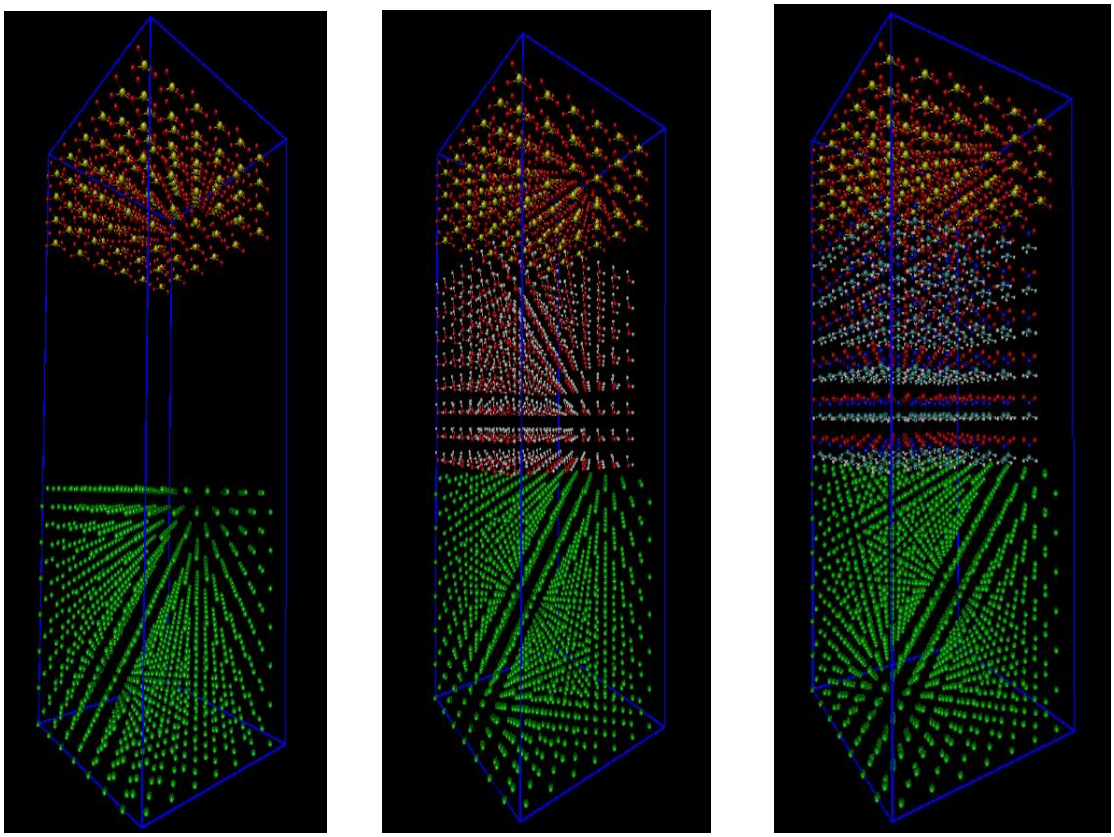

Fig. 25 The three scenarios for the nanosensor – 216 case (a) gold glass interaction (b) gold water glass interaction (c) gold nitromethane glass interaction.

4.5.5 Results

Since in our nanosensor, the gold box represents the gold electrode that will interact with the analyte (water or nitromethane), we limit the analysis of the three scenarios to the gold atoms. Specifically, only the 98 surface gold atoms are taken into consideration since these atoms interact directly with the analyte. We begin with determining the dynamic properties (velocity autocorrelation function) and subsequently we perform the frequency analysis.

4.5.5.1 Dynamical properties

To determine the dynamical properties we calculated the molecular center of mass linear velocity autocorrelation function (VAF). The velocity dcd file was used in conjunction with a fortran program to find the velocities of the 98 gold atoms at different time steps. The final VAF is calculated as the average of all VAF's calculated in the course of the simulation. Fig. 26 shows the VAF's for the three scenarios – gold glass, gold water glass and gold nitromethane glass. As seen from plot, the VAF for all three scenarios decreases rapidly to zero and then enters a negative region corresponding to the "cage effect" and finally settles down to oscillate between positive and negative values suggesting the presence of strong interatomic forces and providing evidence that the gold is in a solid phase as expected. These values however decay with time resembling a damped harmonic motion. The three VAF curves on the first glance seem similar but on a closer look one can see small differences between the values. It seems that the presence of water or nitromethane does not have a significant effect on the gold atoms. This can be explained using the underdamped scenario of damped harmonic motion. The interaction of gold with other atoms produces an increased damping force when compared to the case when gold is not interacting with other atoms. We compare the interactions of gold with water and gold with nitromethane using the Lennard Jones parameters which form the basis for non bonded interactions. As seen from the parameters, nitromethane would produce a damping force which is more than the one produce by water on the vibrations of the surface gold atoms. Therefore from the plot we can see that for the gold nitromethane glass interaction, the frequency is lesser when

compared to the curve of gold water glass interaction. However the gold gold interaction modeled through the Lennard Jones interaction is stronger than the interaction of gold with other atoms. Therefore the presence of water or nitromethane molecules produces only a minute change in the dynamics of the gold atoms.

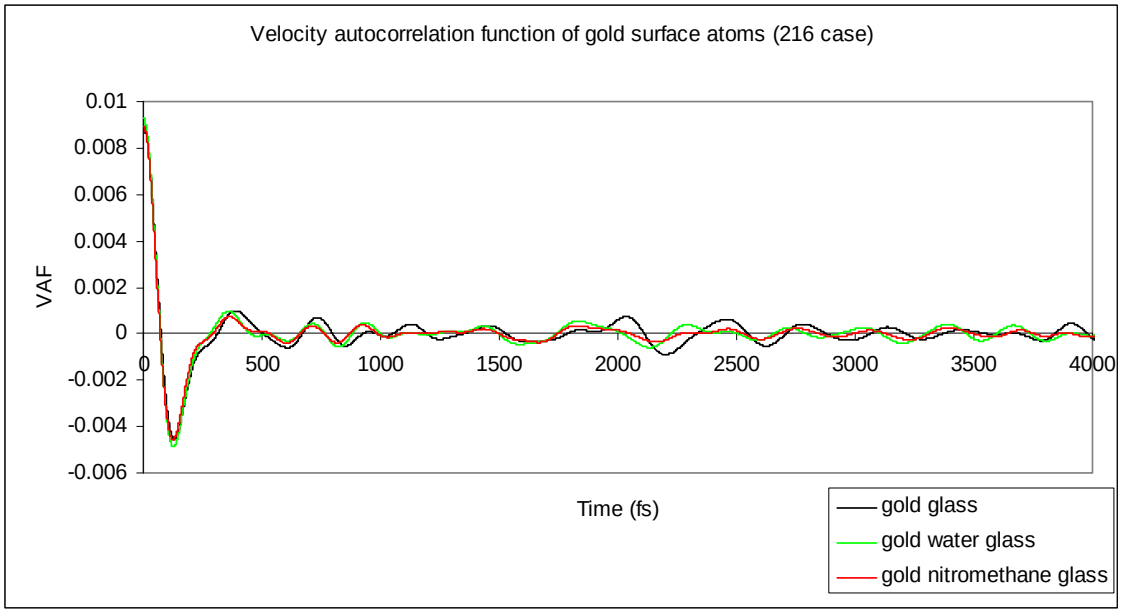

Fig. 26 Velocity autocorrelation function of 98 surface gold atoms. Oscillatory nature of VAF decaying with time resembles a damped harmonic motion and suggests the presence of strong interatomic forces.

4.5.5.2 Vibrational properties

The vibrational spectrum of the three scenarios are extracted from the analysis of the MD simulations. We perform the fast fourier transform of the velocity autocorrelation function in order to determine the underlying frequency characteristics. Fig 26a shows the frequency spectrum of the 98 surface gold atoms for the gold glass interaction. As we have explained the silicon dioxide molecules are fixed and the interactions due to

these molecules are not considered. Therefore the vibrational spectrum for gold glass interaction can be considered to be as the vibrational spectrum for bulk gold. The spectrum seems to be qualitatively similar to the spectrum for bulk gold in ref. [66] [67] [68]. The two peaks at approximately 2 THz and 3 THz correspond to the two main vibrational modes of bulk Au. Fig. 27(b) shows the frequency spectrum for the gold water glass interaction. As explained in the previous section, the presence of water gives rise to a damping constant in the vibrational characteristics of gold. As a result of this we see that the frequency peak at 3 THz moves to a lower frequency. In addition, we see that the damping constant causes a broadening of the spectrum of gold water glass interaction. We can also explain this phenomenon using the dispersion relation. The underdamped condition causes a reduction in the effective force constant between neighboring gold atoms and as a result the frequency also reduces. Fig. 25(c) shows the frequency spectrum for gold nitromethane glass interaction. Intuitively one can conclude that nitromethane effects the lattice vibrations of gold to a much greater extent than water. The presence of nitromethane causes highly damped harmonic vibrations in gold and as a result the spectral density plot does not show any well-defined peaks which were evident in the gold glass and gold water glass interactions. The damping constant resulting from the presence of nitromethane is much higher than that of the one resulting from the presense of water. As a consequence of this, the frequency spectrum of gold nitromethane glass broadens to a much greater extent than for the other two interactions. These differences could form the basis for sensing the analyte, in our case the nitromethane.

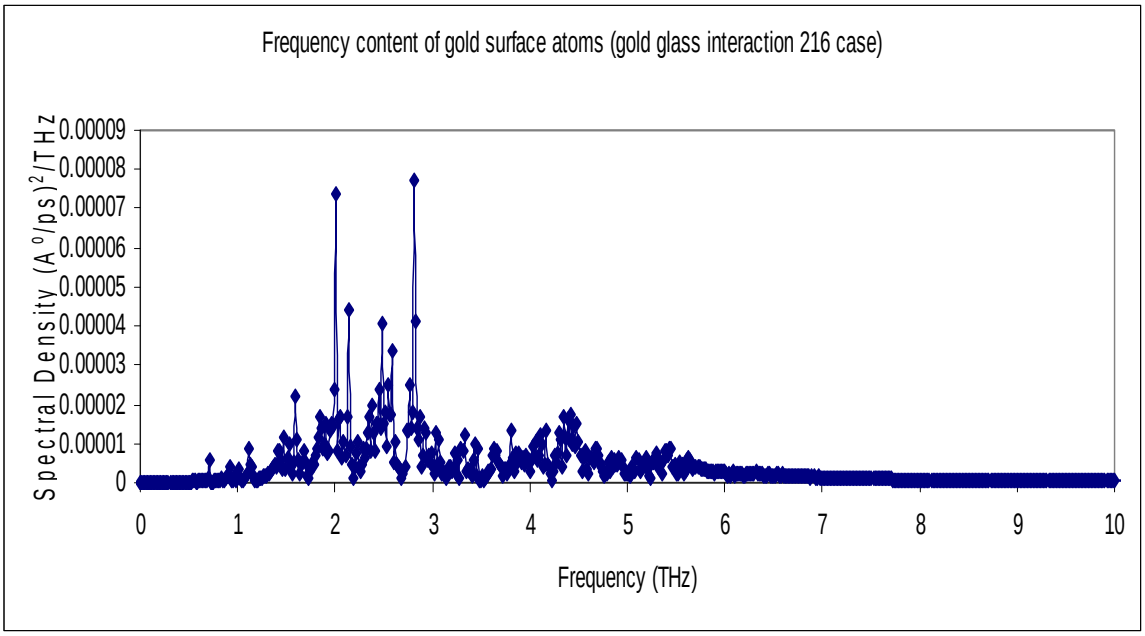

(a)

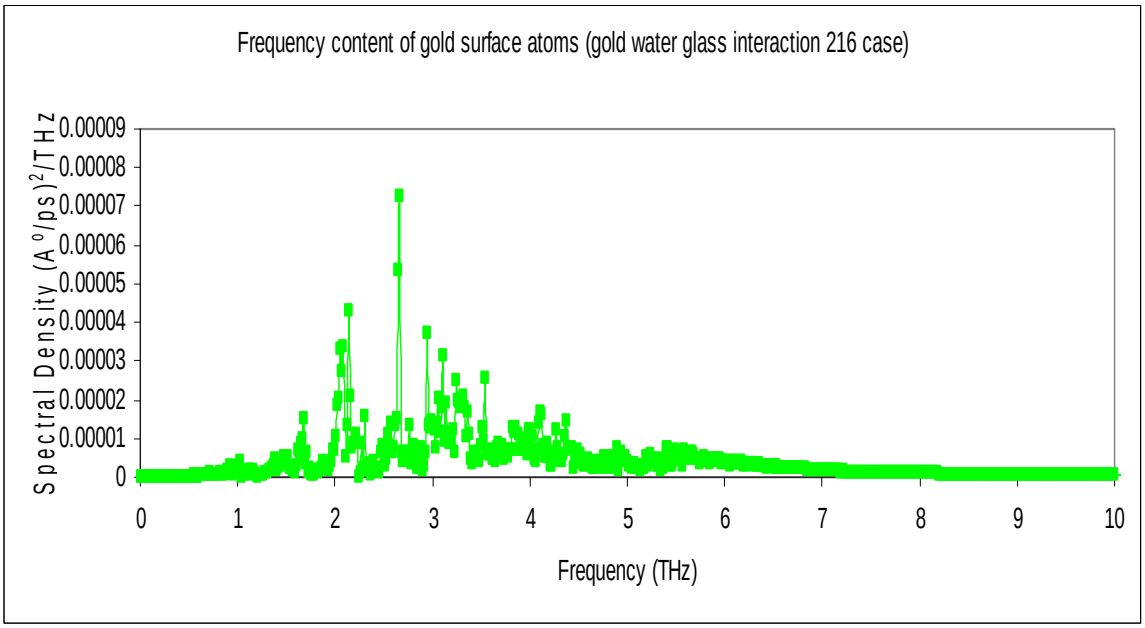

(b)

Fig. 27 Vibrational spectrum of the three interactions – 216 case. The spectrum is obtained from taking the FFT of the velocity autocorrelation function of the 98 surface gold atoms for each of the three interactions. (a) gold glass interaction vibrational spectrum. (b) gold water glass interaction vibrational spectrum (c) gold nitromethane glass vibrational spectrum. (d) vibrational spectrum of all three interactions.

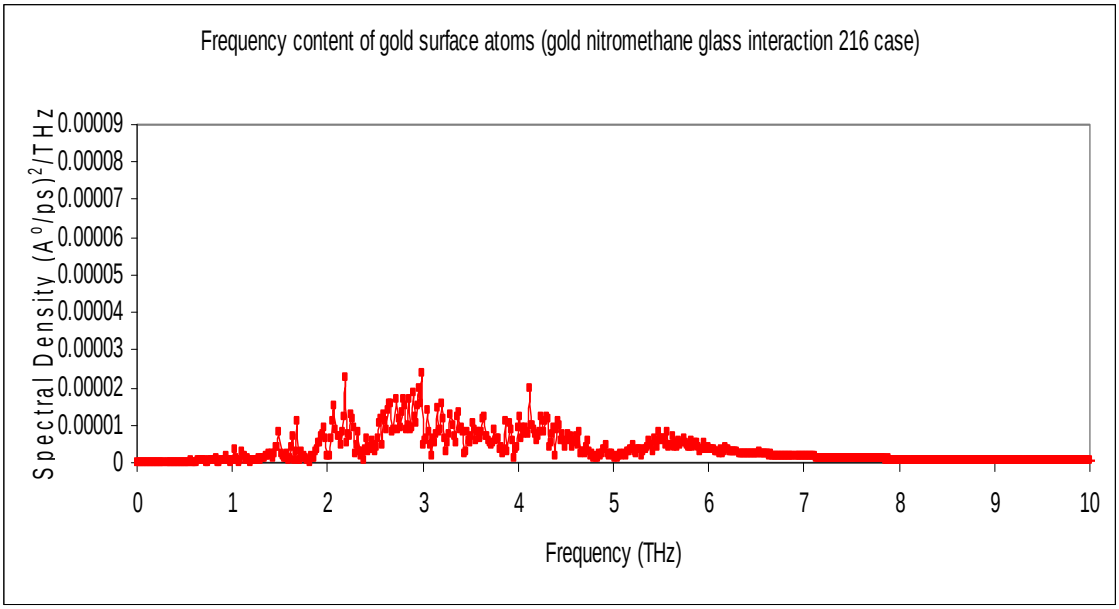

(c)

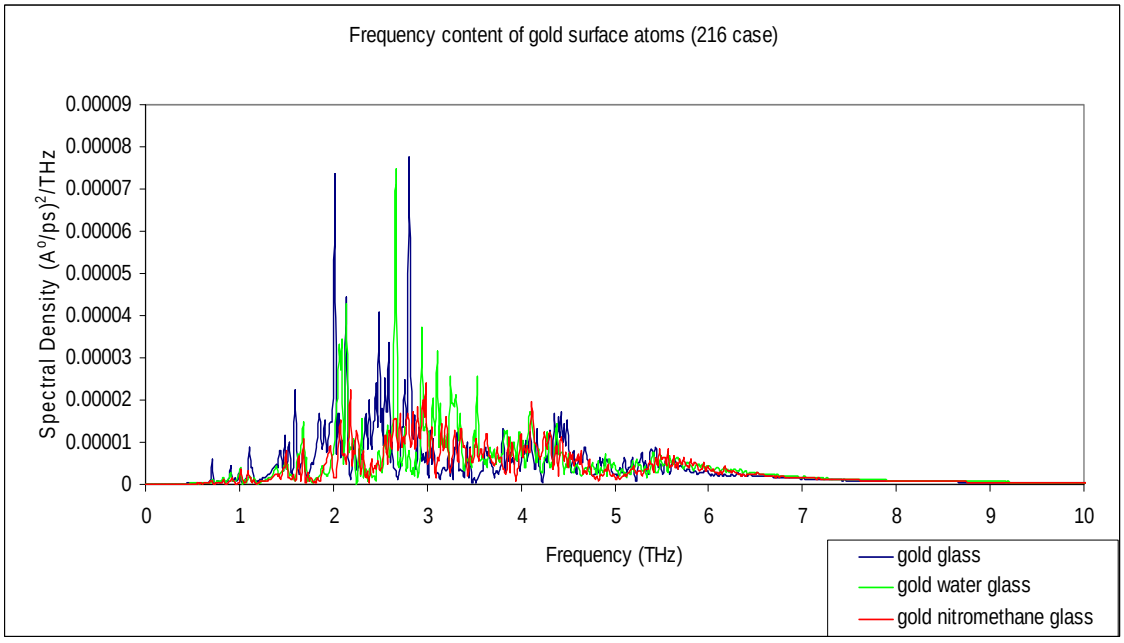

(d)

Fig. 27 continued.

4.6 M.D test bed for 1000 nitromethane molecules

We have already designed, simulated and analyzed the test bed for 216 nitromethane molecules, we now scale the system so as to analyze a 1000 molecules of nitromethane. As in the 216 case we envisage that the test bed for 1000 molecules would be subjected to three different scenarios - gold glass interaction, gold water glass interaction and gold nitromethane glass interaction.

4.6.1 Gold glass interaction

To model this interaction we build a box of gold first and then a box of glass at a certain distance from the box of gold.

4.6.1.1 Design of gold box

We build a gold box with (111) orientation to ensure that maximum number of gold atoms are exposed to the analyte. We have already established the unit cell axis dimension is around 4.078 Å with the nearest neighbor being at a distance of 2.883581 Å. Thus we can build a gold f.c.c crystal with (111) orientation. We build a gold cube that has a side of 44.645732 Å. If you note this was the side length of the cube for the 1000 nitromethane molecules. Using the unit cell shown in Fig. 23, for a given cube side length of 44.645732 Å, we see that na unit cells (as shown in Fig. 28) can be fit into the side. For a unit cell axis dimension (a) equal to 4.078 Å, we can fit 11 unit cells. Therefore as show in Fig. 28, we can fit 11 unit cells along each axis. Hence the total number of gold atoms is 4*11*11*11 = 5324 atoms.

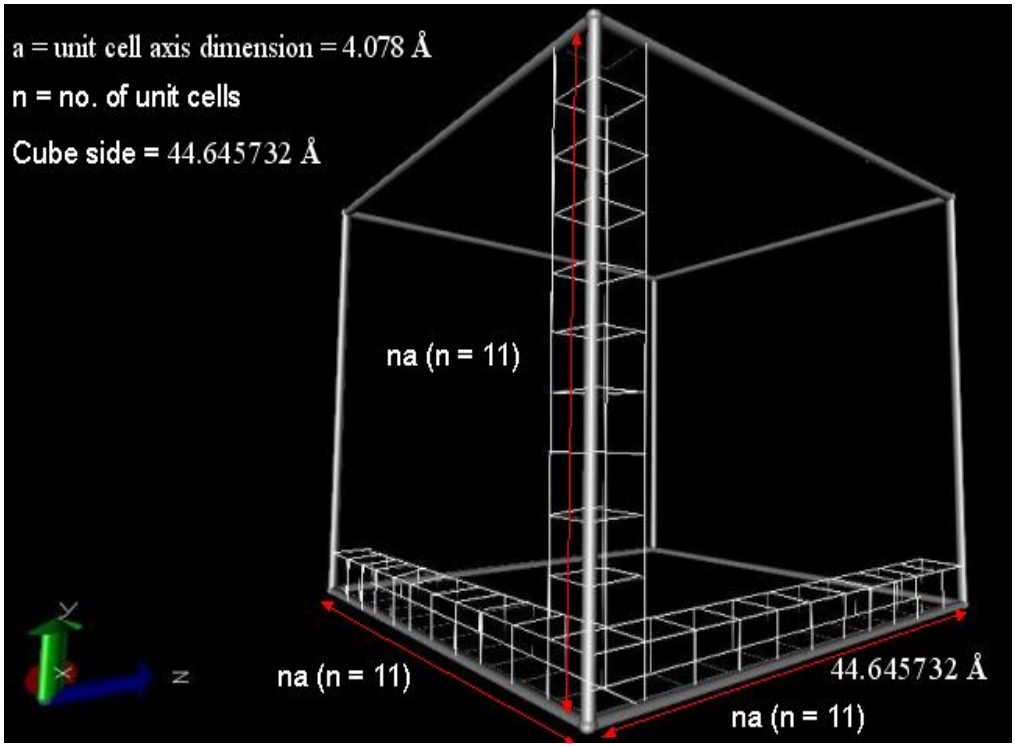

Fig. 28 Gold box dimensions - 1000 case. For a cube of side 44.645732 Å and unit cell axis dimension (a) of 4.078 Å, we can fit 11unit cells along each axis. The total number of gold atoms in the cube is 4*11*11*11 = 5324 atoms.

4.6.1.2 Design of glass box

We proceed to design a box that contains amorphous silicon dioxide molecules. The box needs to hold 1000 silicon dioxide molecules with the density being 2.6 gm/c.c and the molecular weight being 60.1 gm/mol. The volume of box was calculated to be 38383.994873 $Å^3$. Therefore the dimensions of the silicon dioxide box are 44.645732 Å X 44.645732 Å X 19.257073 Å. The silicon dioxide box we have designed is to be inert. The silicon dioxide molecules are rigid and do not interact with the gold atoms.

4.6.2 Gold water glass interaction

For this interaction we build a box of water in between the boxes of gold and glass.

4.6.2.1 Design of water box

The design of the glass box follows the same design principles as that of the glass box. We begin with the initial information that we need to build a water box containing 2744 molecules. Therefore for water density 1 gm/c.c and molecular weight 18.0154 gm/mol, the volume of box comes to be 82087.05006 $Å^3$. The dimensions of the water box are 44.645732 Å X 44.645732 Å X 41.182694 Å.

4.6.3 Gold nitromethane glass interaction

Lastly to facilitate the sensing of nitromethane, we add a box of nitromethane between the gold and glass boxes.

4.6.3.1 Design of nitromethane box

The design of the nitromethane box follows the same design principles as that of the glass box. We begin with the initial information that we need to build a nitromethane box containing 1000 molecules. Therefore for nitromethane density of 1.139 gm/c.c and molecular weight 61.04 gm/mol, the volume of box comes to be 88989.720722 $Å^3$. The dimensions of the water box are 44.645732 Å X 44.645732 Å X 44.645732 Å. It is important to reiterate here that the interaction between the carbon and nitrogen atoms of nitromethane are modeled using the Lennard Jones potential.

4.6.4 MD simulations

For the three types of scenarios as shown in Fig. 29(a)-(c) we perform an isochoric, isothermal molecular dynamics simulations using the NAMD program (NVT ensemble). Periodic boundary conditions are used and constant temperature of 300 K is achieved via langevin dynamics. The langevin damping coefficient is chosen to be 5 /ps which we believe is sufficient for such a system. The equations of motion are integrated using the Verlet leapfrog procedure with a timestep of 1 fs. The cutoff distance chosen was 12 Å and the long range electrostatic interactions were calculated using particle mesh ewald sum method which is especially effective when periodic boundary conditions are present. In the case of the gold glass interaction, the NVT ensemble was run for 262144 fs. Subsequently a NVE ensemble was run for 65536 fs to ascertain system equilibration and to gather the frequency analysis data. In the case of gold water glass interaction, the NVT ensemble was run for 524288 fs followed by a NVE ensemble for 65536 fs. Similarly for the gold nitromethane glass interaction, the NVT ensemble was run for 1048576 fs followed for a 65536 fs NVE ensemble run. The force field parameters for the three scenarios have already been established and are listed in Tables 3-6. It is important to note that in all these simulations the silicon dioxide molecules are held fixed and their forces are not considered in our calculations and analysis.

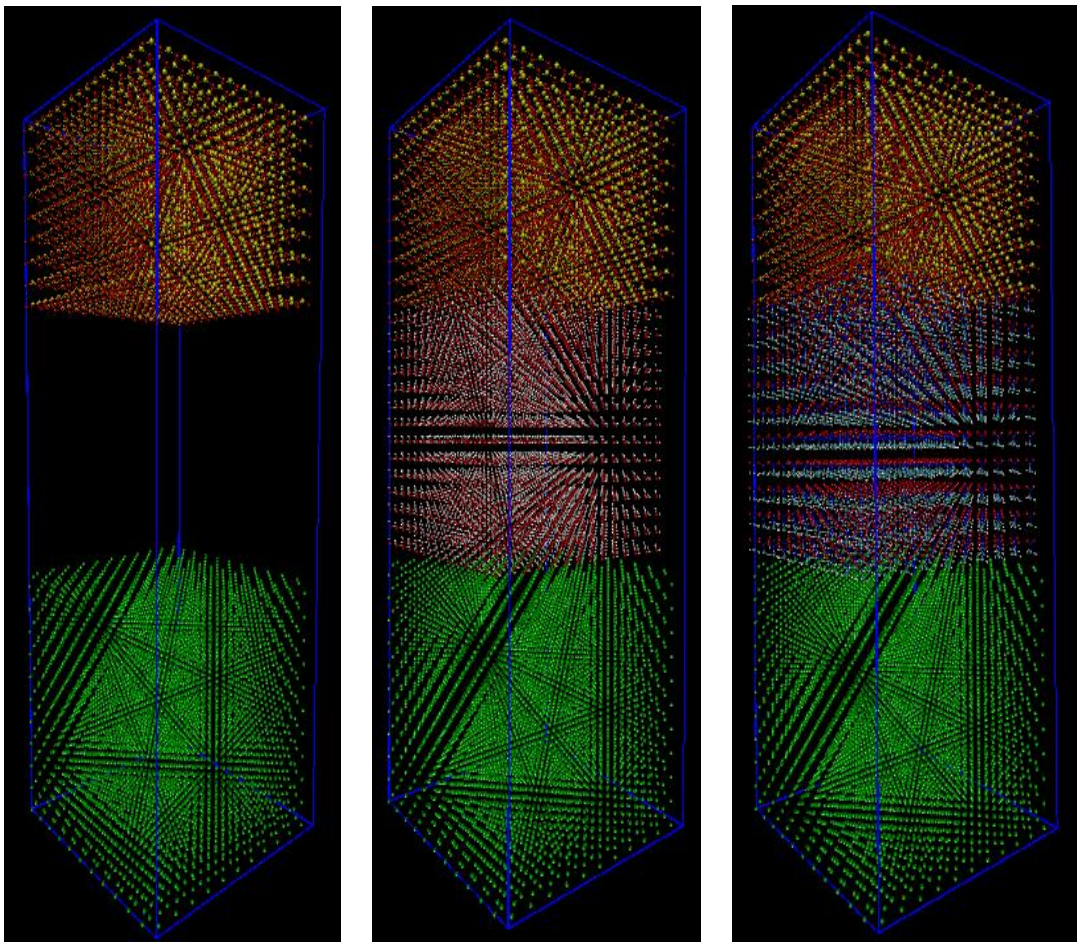

(a) (b) (c)

Fig. 29 The three scenarios for the nanosensor – 1000 case (a) gold glass interaction (b) gold water glass interaction (c) gold nitromethane glass interaction.

4.6.5 Results

As in the 216 case, we limit the analysis of the three scenarios to the gold atoms. Specifically, only the 242 surface gold atoms are taken into consideration since these atoms interact directly with the analyte. We begin with determining the dynamic properties (velocity autocorrelation function) and subsequently we perform the frequency analysis.

4.6.5.1 Dynamical properties

To determine the dynamical properties we calculated the molecular center of mass linear velocity autocorrelation function (VAF). Fig. 30 shows the VAF's for the three scenarios – gold glass, gold water glass and gold nitromethane glass. As seen from the plot, the VAF for all three scenarios decreases rapidly to zero and then enters a negative region and finally settles down to oscillate between positive and negative values. When compared to Fig. 26, we see that the velocity for all three interactions decorrelates much faster with time. We expect such a behavior since the system size is larger and has a larger number of atoms thus resulting in stronger interatomic forces. The dynamical properties resemble a damped harmonic motion satisfying the underdamped condition. The presence of nitromethane or water at this system size also does not cause any significant changes in the vibrational characteristics of the gold atoms. As mentioned in the 216 case scenario, the presence of water or nitromethane results in a damping force on the gold vibrations. The damping force produced by nitromethane molecules is believed to be much higher than the damping force due to the water molecules. Therefore the presence of nitromethane molecules affects the lattice dynamics of gold to a greater extent than water.

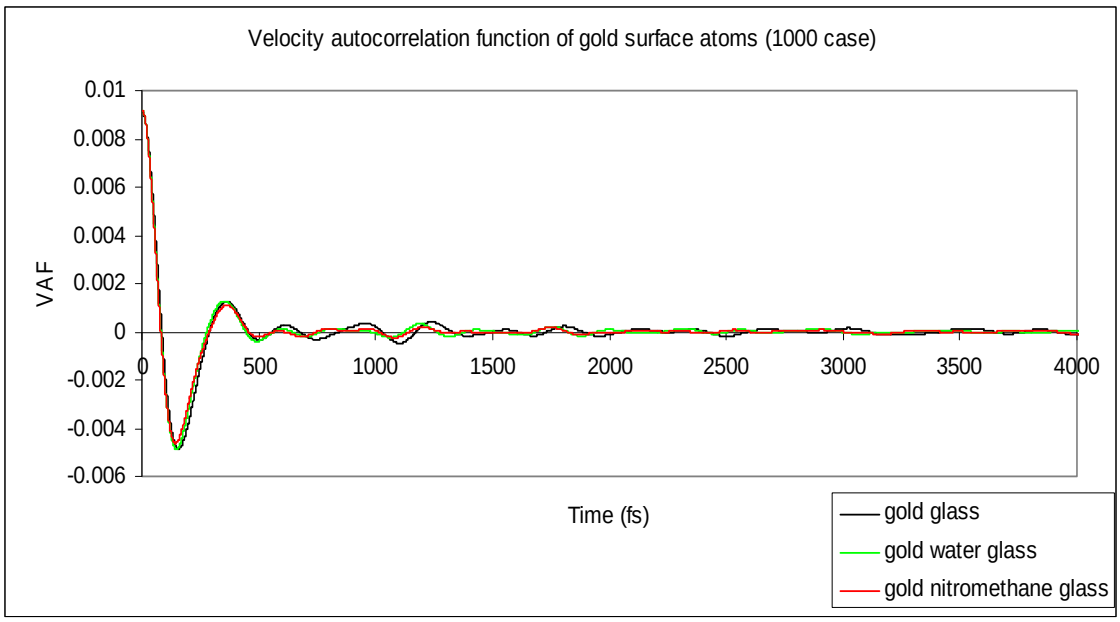

Fig. 30 Velocity autocorrelation function of 242 surface gold atoms. Oscillatory nature of VAF decaying with time resembles a damped harmonic motion and suggests the presence of strong interatomic forces.

4.6.5.2 Vibrational properties

We take the fast fourier transform of the velocity autocorrelation function in order to determine the underlying frequency characteristics. Fig 30a shows the frequency spectrum of the 242 surface gold atoms for the gold glass interaction. As we have explained the silicon dioxide molecules are fixed and the interactions due to these molecules are not considered. Therefore the vibrational spectrum for gold glass interaction can be considered to be as the vibrational spectrum for bulk gold. The spectrum seems to be qualitatively similar to the spectrum for bulk gold in ref. [66-68]. The two characteristic peaks of gold at 2 THz and 3.5 THz can be seen in Fig. 31(a). Fig. 31(b) shows the frequency spectrum of gold water glass interaction. We see that the damping force due to the presence of water causes the peak at 3.5 THz to shift to a lower

value. The damping constant also broadens the spectrum. Using the dispersion relation, the damping force reduces the effective force constant between gold atoms thus reducing the frequency. Fig. 31(c) shows the vibrational spectrum of gold nitromethane glass interaction. As explained earlier the presence of nitromethane results in a greater damping constant than the one resulting from the presence of water. Due to this we see that the frequency peak shifts to a much lower frequency. Again this can be also explained using the dispersion relation as we did for the gold water glass interaction. The increase in damping constant also causes the gold nitromethane glass interaction frequency spectrum to broaden. We now perform a qualitative comparison of the plots in Fig. 26(d) and Fig. 31(d). We see that for the 216 case scenario the qualitative aspect of the characteristic spectrum of gold (gold glass interaction) is still maintained in the presence of water and nitromethane. However, when we consider the 1000 case scenario, we see that the characteristic spectrum of gold (gold glass interaction) goes a lot of change in the presence of water and nitromethane. This can be attributed to the fact that the velocity of gold atoms decorrelates with time much faster due to strong interatomic forces. In other words, the gold loses it frequency characteristics in the presence of water and nitromethane. We can thus conclude that the effect of water and nitromethane in the 1000 case scenario is much greater than the effect in the 216 case scenario.

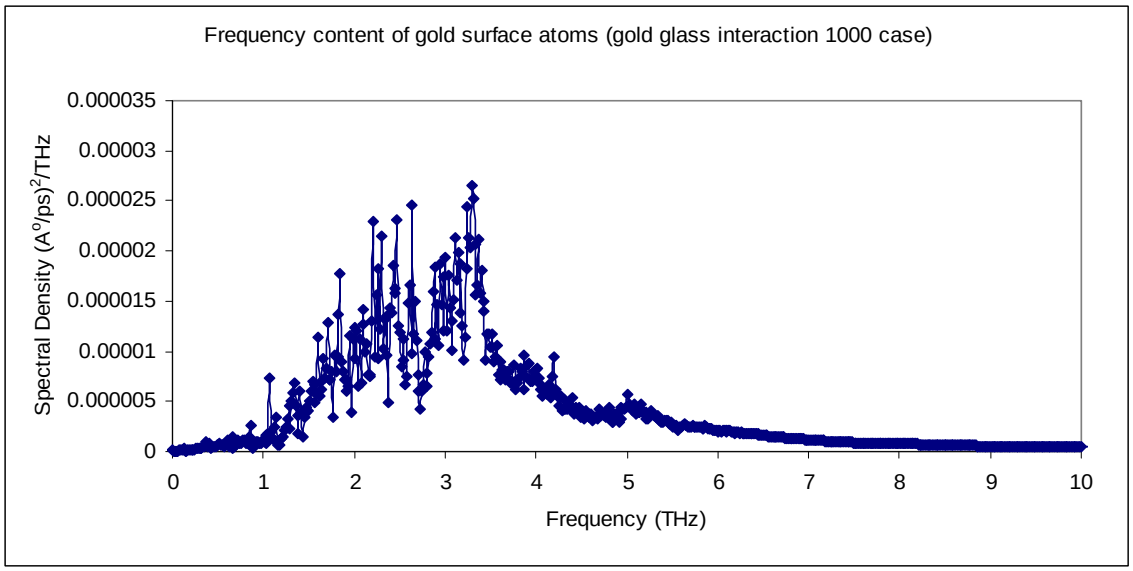

(a)

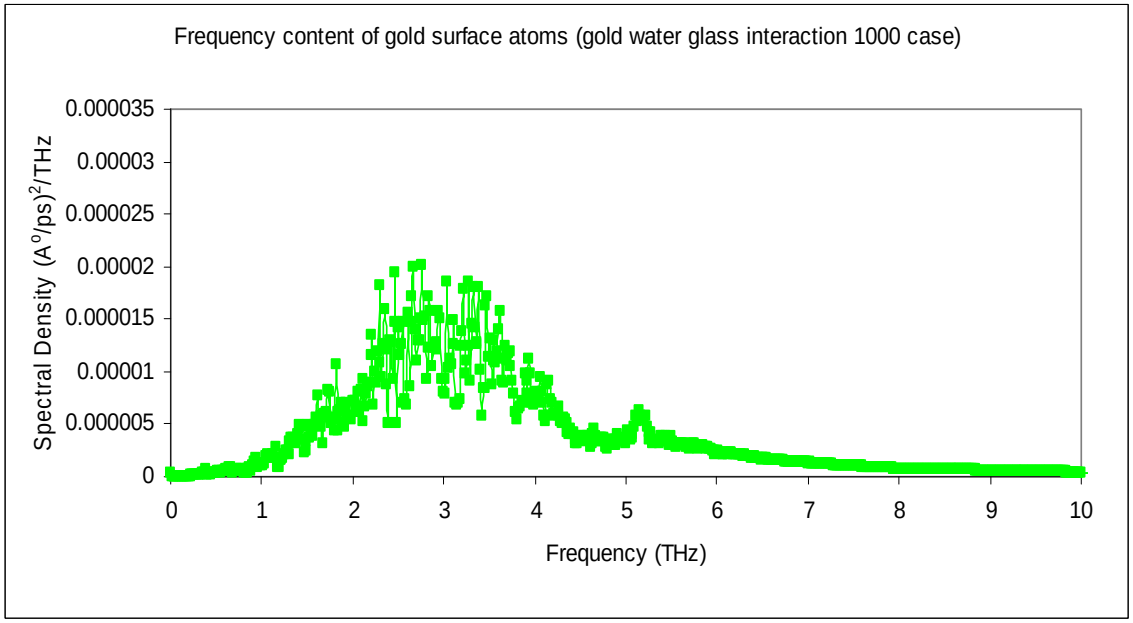

(b)

Fig. 31 Vibrational spectrum of the three interactions – 1000 case. The spectrum is obtained from taking the FFT of the velocity autocorrelation function of the 242 surface gold atoms for each of the three interactions. (a) gold glass interaction vibrational spectrum. (b) gold water glass interaction vibrational spectrum (c) gold nitromethane glass vibrational spectrum. (d) vibrational spectrum of all three interactions.

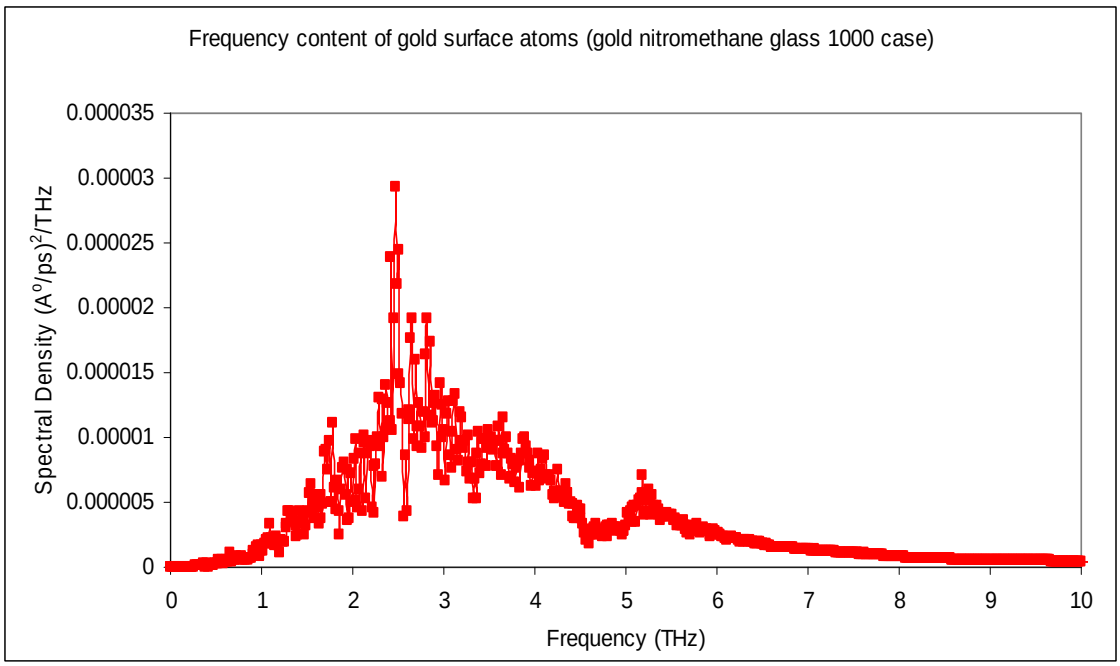

(c)

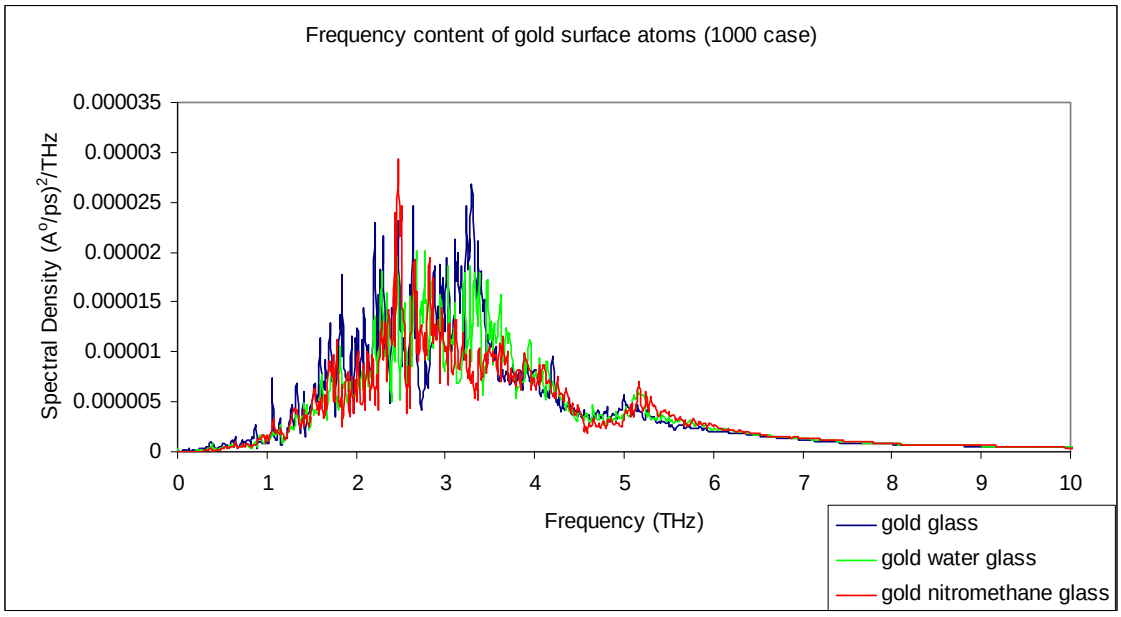

(d)

Fig. 31 continued.

5. CONCLUSION

We have performed the design, simulation and analysis of a nanosensor that operates on terahertz frequencies and can sense an energetic substance like nitromethane. We performed extensive MD simulations on nitromethane using a classical potential and determined its frequency characteristics. We performed the simulations on two system sizes; one containing 216 nitromethane molecules and the other containing 1000 nitromethane molecules. We found that the frequencies obtained were in agreement with the experimentally determined frequencies. In order to allow dissociation of nitromethane when it comes in contact with the nanosensor we simulated dissociation characteristics of the two system sizes. The results from the analysis showed that the nitromethane dissociates through the CN bond scission as expected.

We designed two nanosensors that can interact with the two system sizes (216 and 1000) of nitromethane. We envisaged that the nanosensors would be involved in three types of interactions – gold glass, gold water glass and gold nitromethane glass. We performed simulations to model these interactions and performed the dynamic property and vibrational property analysis. Gold was the main sensing medium in our nanosensor and we considered the effect of water and nitromethane on the properties of gold. The nanosensors showed terahertz operation characteristics. It was seen that the presence of water and nitromethane causes certain measurable changes in the frequency characteristics of gold. The changes are observed mainly in the terahertz region of the electromagnetic spectrum. We believe the presence of water and nitromethane results in a damping force on the vibrations of gold thus causing a change in the frequency

spectrum of gold. The effect of water and nitromethane is more in the case of the larger system (1000 case) which results in stronger interatomic forces. We believe these changes in frequency are measurable and thus provide a means of sensing nitromethane. We have thus provided a proof of concept of a molecular nanosensor that operates in terahertz frequencies and can sense energetic materials like nitromethane.

Finally, we would like to mention that the results obtained from MD simulations are as accurate as the force field parameters used. We would like to calculate accurate force field parameters through the use of ab initio methods. The experimental setup would involve the building of the nanosensor consisting of a layer of gold atoms and a layer of glass separated by a very small gap. The nanosensor would be subjected to terahertz radiation through a terahertz source and a terahertz detector would be used to analyze the transmitted signals. We believe that the presence of nitromethane in the gap will cause sufficient changes in the transmitted signals which can be easily detected by the terahertz detector thus providing a means to detect the presence of nitromethane.

REFERENCES

[1] I. L. Medintz, G. P. Anderson, M. E. Lassman, E. R. Goldman, L. A. Bettencourt, and J. M. Mauro, "General Strategy for Biosensor Design and Construction Employing Multifunctional Surface-Tethered Components, " *Analytical Chemistry*, vol. 76, pp. 5620-5629, Sep. 2004.

[2] A. Nel, T. Xia, L. Madler, and N. Li, "Toxic Potential of Materials at the Nanolevel," *Science*, vol. 311, pp. 622-627, Feb. 2006.

[3] D. Prosnitz, "WMD Sensors--Search and Seizure," *Science*, vol. 310, pp. 978, Nov. 2005.

[4] K. Brown, "Biosecurity: Up in the Air," *Science*, vol. 305, pp. 1228-1229, Aug. 2004.

[5] "Biological agents" available at http://www.bt.cdc.gov/agent/agentlist-category.asp, Accessed Feb. 2007.

[6] "Chemical agents" available at http://www.bt.cdc.gov/agent/agentlistchem-category.asp, Accessed Feb. 2007.

[7] T. A. Taton, C. A. Mirkin, and R. L. Letsinger, "Scanometric DNA Detection with Nanoparticle Probes," *Science*, vol. 285, pp. 1757-1760, Sep. 2000.

[8] S. J. Park, T. A. Taton, and C. A. Mirkin, "Array Based Electrical Detection of DNA with Nanoparticle Probes," *Science*, vol. 295, pp. 1503-1506, Feb. 2002.

[9] M. G. Ancona, A. W. Snow, E. E. Foos, W. Kruppa, and R. Bass, "Scaling Properties of Gold Nanocluster Chemiresistor Sensors," *IEEE Sensor*, vol. 6, pp. 1403-1414, Dec. 2006.

[10] J. M. Seminario, Y. Ma, and V. Tarigopula, "The NanoCell: A Chemically Assembled Molecular Electronic Circuit," *IEEE Sensor*, vol. 6, pp. 1614-1626, Dec. 2006.

[11] E. S. Snow, F. K. Perkins, E. J. Houser, S. C. Badescu, and T. L. Reinecke, "Chemical Detection with a Single-Walled Nanotube Capacitor," *Science*, vol. 307, pp. 1942-1945, Mar. 2005.

[12] J. C. Meyer, M. Paillet, and S. Roth, "Single Molecule Torsional Pendulum," *Science*, vol. 309, pp. 1539-1541, Sep. 2005.

[13] G. Shekhawat, S. H. Tark, and V. P. Dravid, "MOSFET Embedded Microcantilevers for Measuring Deflection in Biomolecular Sensors," *Science*, vol. 311, pp. 1592-1595, Mar. 2006.

[14] B. A.Korgel, "Nanosprings Take Shape," *Science*, vol. 309, pp. 1683-1684, Sep. 2005.

[15] J. V. Ruitenbeek, "Silver Nanoswitch," *Nature*, vol. 433, pp. 47-50, 2005.

[16] W. Fritzsche and T. A. Taton, "Metal Nanoparticles and Labels for Heterogeneous, Chip-Based DNA Detection," *Nanotechnology*, pp. 63-73, Oct. 2003.

[17] P. J. Treado, "Reagentless Molecular Chemical Imaging," in 19th Annual NDIA Security Symposium & Exhibition, 2005.

[18] D. L. Woolard, T. Koscica, D. L. Rhodes, H. L. Cui, R. A. Pastore, J. O. Jensen, J. L. Jensen, W. R. Loerop, R. H. Jacobsen, D. Mittleman, and M. C. Nuss, "Millimeter Wave Induced Vibrational Modes in DNA as a Possible Alternative to Animal Tests to Probe for Carcinogenic Mutations," *J. Appl. Toxicol.*, vol. 17, pp. 243–246, Apr. 1997.

[19] E. R. Mueller, "Terahertz Radiation: Applications and Sources," *The Industrial Physicist*, vol. 9, pp. 27, Aug. 2003.

[20] J. M. Seminario, P. A. Derosa, L. E. Cordova, and B. H. Bozard, "A Molecular Device Operating at Terahertz Frequencies: Theoretical Simulations," *Nanotechnology*, vol. 3, pp. 215-218, Mar. 2004.

[21] J. M. Seminario, L. Yan, and Y. Ma, "Transmission of Vibronic Signals in Molecular Circuits," *Physical Chemistry*, vol. 109, pp. 9712-9715, Oct. 2005.

[22] D. L. Woolard, E. R. Brown, M. Pepper, and M. Kemp, "Terahertz Frequency Sensing and Imaging: A Time of Reckoning Future Applications?," *Proceedings of the IEEE*, vol. 93, pp. 1722-1743, Oct. 2005.

[23] M. K. Choi, K. Taylor, A. Betterman, and D. Vanderweide, "Spectroscopy with Electronic Terahertz Techniques for Chemical and Biological Sensing," in *Terahertz Sensing Technology*, vol. 2, L. Woolar, Shur, Ed.: Singapore: World Scientific, 2003, pp. 35-48.

[24] E. R. Brown, T. B. Khromova, T. Globus, D. L. Woolard, J. O. Jensen, and A. Majewskiv, "Narrow THz Attenuation Signatures in *Bacillus subtilis* Spores," *Phys Rev. Lett,* 2005.

[25] G. P. Gallerano, "Overview of Terahertz Radiation Sources," *Proceedings of the 2004 Free Electron Laser Conference*, 216-221, 2004.

[26] S. Ebbinghaus, K. Schrock, J. C. Schauer, E. Bründermann, M. Heyden, G. Schwaab, M. Boke, J. Winter, M. Tani, and M. Havenith, "Terahertz Time-Domain Spectroscopy as a New Tool for the Characterization of Dust Forming Plasmas," *Plasma Sources Sci. Technol*, vol. 15, pp. 72-77, Feb. 2006.

[27] T. W. Crowe, T. Globus, D. L. Woolard, and J. L. Hesler, "Terahertz Sources and Detectors and Their Detection to Biological Sensing," *Phil. Trans. R. Soc. Lond.*, vol. A, pp. 365-377, Feb. 2004.

[28] A. Tredicucci, R. Kohler, L. Mahler, H. E. Beere, E. H. Linfield, and D. A. Ritchie, "Terahertz Quantum Cascade Lasers—First Demonstration and Novel Concepts," *Semicond. Sci. Technol*, vol. 20, pp. S222-S227, Jun. 2005.

[29] B. Ferguson and X. Zhang, "Materials for Terahertz Science and Technology," *Nature Materials*, pp. 26-33, 2002.

[30] M. Koch, "Terahertz sources: The Search Continues for Efficient Terahertz Sources," in *Laser Focus*, 2005.

[31] C. Moller and M. S. Plesset, "Note on an Approximation Treatment for Many-Electron Systems," *Phys. Rev.*, vol. 46, pp. 618-622, Oct. 1934.

[32] B. L. Frank H. Stillinger, "Moller-Plesset Convergence Issues in Computational Quantum Chemistry," *Chemical Physics*, vol. 112, pp. 9711-9715, Mar. 2000.

[33] M. L. Leininger, W. D. Allen, H. F. Schaefer, and C. D. Sherrill, "Is Moller–Plesset Perturbation Theory a Convergent *ab initio* Method?," *Chemical Physics*, vol. 112, Jun. 2000.

[34] F. L. Pilar, *Elemental Quantum Chemistry*, 2nd ed. New York: McGraw-Hill, 2001.

[35] A. P. Scott and L. Radom, "Harmonic Vibrational Frequencies: An Evaluation of Hartree-Fock, Moller-Plesset, Quadratic Configuration Interaction, Density Functional Theory, and Semiempirical Scale Factors," *Physical Chemistry*, vol. 100, pp. 16502-16513, Jul. 1996.

[36] P. Hohenberg and W. Kohn, "Inhomogeneous Electron Gas," *Phys. Rev.*, vol. 136, Nov. 1964.

[37] W. Kohn and L. J. Sham, "Self-Consistent Equations Including Exchange and Correlation Effects," *Phys. Rev.*, vol. 140, Nov. 1965.

[38] G. Onida, L. Reining, and A. Rubio, "Electronic Excitations: Density-Functional Versus Many-Body Green's-function Approaches," *Rev. Mod. Phys.*, vol. 74, pp. 601-659, Jun. 2002.

[39] D. Szasz, "Boltzmann's Ergodic Hypothesis, a Conjecture for Centuries?," presented at International Symposium in Honor of Boltzmann's 150th Birthday, Vienna, Feb. 1994.

[40] B. J. Alder and T. E. Wainwright, "Phase Transition of a Hard Sphere System," *Chemical Physics*, vol. 27, Nov. 1957

[41] F. H. Stillinger and A. Rahman, "Improved Simulation of Liquid Water by Molecular Dynamics," *J. Chem. Phys.*, vol. 60, pp. 1545-1557, Feb. 1974.

[42] J. A. McCammon, B. R. Gelin, and M. Karplus, "Dynamics of Folded Proteins," *Nature* vol. 267, pp. 585-590, 1977.

[43] "Molecular dynamics tutorial pages." available at ch.EMBnet.org, Accessed Feb 2007.

[44] J. M. Seminario and L. Saenz, "Intensity Enhancement of the Vibrational Spectrum of Oxygen When Attached to a Platinum Nanocluster," *J. Chem. Phys.*, vol. 125, Nov. 2006.

[45] S. Pan, Z. Wang, T. D. Krauss, H. Du, and L. J. Rothberg, "The Structural Basis for Giant Enhancement Enabling Single-Molecule Raman Scattering.," *PNAS*, vol. 100, pp. 8638-8643, Jul. 2003.

[46] S. Zou and G. C. Schatz, "Silver Nanoparticle Array Structures that Produce Giant Enhancements in Electromagnetic Fields," *Chemical Physics Letters*, vol. 403, pp. 62-67, 2005.

[47] A. Sokolov, "Developing Optical Techniques for Analysis of Materials at the Nanoscale," in Polymer Photonics Workshop, Akron, April. 2004.

[48] J. E. L. Jones, "Cohesion," *Proceedings of Physical Society*, vol. 43, pp. 461-482, Sep. 1931.

[49] J. W. Cooley and J. W. Tukey, "An Algorithm for the Machine Calculation of Complex Fourier Series," *Math. Comput.*, vol. 19, pp. 297-301, Apr. 1965.

[50] G. R. Cooper and C. D. McGillem, *Probabilistic Methods of Signal and System Analysis*, 2nd ed. New York: CBS college publishing, 1986.

[51] Huheey, "*The Strengths of Chemical Bonds,*" London: Butterworths Scientific, 1958.

[52] M. F. Kropman and H. J. Bakker, "Dynamics of Water Molecules in Aqueous Solvation Shells," *Science*, vol. 291, pp. 2118-2120, Mar. 2001.

[53] R. Faiman and K. Laresson, "Assignment of the C-H Stretching Vibrational Frequencies in the Raman Spectra of Lipids," *Journal of Raman Spectroscopy*, vol. 4, pp. 387-394, Oct. 1975.

[54] "Eleventh report on carcinogens," available at http://ntp.niehs.nih.gov/ntp/roc/toc11.html Accessed Feb, 2007.

[55] A. P. Cox and S. Waring, "Microwave Spectrum and Structure of Nitromethane," *J. Chem. Soc.*, vol. 68, pp. 1060-1071, Dec. 1972.

[56] S. Courtecuisse and F. Cansell, "Comparative Raman Spectroscopy of Nitromethane-h3 , Nitromethane-d3, and Nitromethane up to 20 GPa," *Journal of Chemical Physics*, vol. 108, pp. 7350-7355, May. 1998.

[57] J. M. Seminario, M. C. Concha, and P. Politzer, "Molecular Dynamics Simulation of Liquid Nitromethane Shocked to 143 kbar," *International Journal of Quantum Chemistry*, vol. 29, pp. 621-625, Mar. 1995.

[58] P. M. Agrawal, B. M. Rice, and D. M. Thompson, "Molecular Dynamics Study of the Melting of Nitromethane," *Journal of Chemical Physics* vol. 119, pp. 9617-9627, Nov. 2003.

[59] D. C. Sorescu, B. M. Rice, and D. L. Thompson, "Molecular Dynamics Simulations of Liquid Nitromethane," *J. Phys. Chem.* , vol. 105, pp. 9336-9346, Sep. 2001.

[60] W. Hu, T. He, D. Chen, and F. Liu, "Theoretical Study of the CH3NO2 Unimolecular Decomposition Potential Energy Surface," *J. Phys. Chem.*, vol. A, pp. 7294-7303, Jul. 2002.

[61] S. Han, A. V. Duin, and A. Strachan, "Thermal decomposition of condensed nitromethane from molecular dynamics using the ReaxFF Reactive force field," in APS March Meeting, 2005.

[62] D. C. Sorescu, B. M. Rice, and D. L. Thompson, "Theoretical Studies of Solid Nitromethane," *J. Phys. Chem.*, vol. 2000, pp. 8406-8419, Aug. 2000.

[63] B. M. Rice and D. L. Thomson, "Classical Dynamics Studies of Unimolecular Decomposition of Nitromethane," *J. Chem. Phys.*, vol. 93, pp. 7986-8000, Dec. 1990.

[64] H. D. Stidham, G. A. Guirgis, B. J. V. Veken, T. G. Sheehan, and J. R. Durig, "Raman Spectra and Ab initio Calculations for Methyl Nitrite and Methyl-d_3 Nitrite," *Journal of Raman Spectroscopy*, vol. 21, pp. 615-628, Apr. 1990.

[65] J. A. Dean, *Lange's Handbook of Chemistry,* 15 ed, New York: McGraw-Hill, 1973.

[66] W. J. Lee, S. P. Ju, S. J. Sun, and M. H. Weng, "Dynamical Behaviour of 7-1 Gold Nanowire Under Different Axial Tensile Strains," *Nanotechnology*, vol. 17, pp. 3253-3258, Jun. 2006.

[67] G. Bilalbegovic, "Structure and Stability of Finite Gold Nanowires," *Phys. Rev. B*, vol. 58, Dec. 1998.

[68] J. W. Lynn, H. G. Smith, and R. M. Nicklow, "Lattice Dynamics of Gold," *Phys. Rev. B.*, vol. 8, pp. 3493-3499, Oct. 1973.

VITA

Name:	Sukesh Shenoy
Address:	Department of Mechanical Engineering MS 3123 c/o Dr. Banerjee or Dr. Seminario Texas A&M University College Station, TX 77843-3123
Email Address:	sukeshshenoy@gmail.com
Education:	B.E, Industrial Production Engineering, Manipal Institute of Technology, 1999 M.S, Mechanical Engineering, Texas A&M University, 2007